Charge transfer dynamics and conduction kinetics within photo-electronic junction devices based on some inorganic semiconductor nanocomposites: Theoretical Insights and Experimental Studies

A Thesis Submitted to

Jadavpur University, Kolkata

In partial fulfillment of the requirements for the degree of

Doctor of Philosophy (Ph.D.) in Science

By

Animesh Biswas

Department of Physics

Jadavpur University

Kolkata-700032, India

September 2024

যাদবপুর বিশ্ববিদ্যালয়
কলকাতা - ৭০০ ০৩২, ভারত

JADAVPUR UNIVERSITY
KOLKATA-700 032, INDIA

FACULTY OF SCIENCE : DEPARTMENT OF PHYSICS

CERTIFICATE FROM THE SUPERVISOR(S)

This is to certify that the thesis entitled "**Charge transfer dynamics and conduction kinetics within photo-electronic junction devices based on some inorganic semiconductor nanocomposites: Theoretical Insights and Experimental Studies**" submitted by Sri **Animesh Biswas** who got his name registered on 6th November, 2019 **(Index No. 146/19/Phys./26)** for the award of Ph. D. (Science) degree of Jadavpur University, is absolutely based upon his own work under the supervision of **Prof. Partha Pratim Ray** and **Dr. Animesh Layek** and that neither this thesis nor any part of it has been submitted for either any degree/diploma or any other academic award anywhere before.

Partha Pratim Ray
(Prof. Partha Pratim Ray) 24/09/24

Dr. Partha Pratim Ray
Professor
Department of Physics
Jadavpur University

Animesh Layek
(Dr. Animesh Layek)

Dr. Animesh Layek
Assistant Professor
Department of Physics
Jadavpur University
Kolkata - 700032

ABSTRACT

Index No.: 146/19/Phys./26

Thesis Title: "Charge transfer dynamics and conduction kinetics within photo-electronic junction devices based on some inorganic semiconductor nanocomposites: Theoretical Insights and Experimental Studies".

The dissertation is mainly focused upon the original synthesis technique and characterization processes of semiconductor nanomaterials. The ternary I-III-VI_2 Semiconductor $CuInSe_2$ has been synthesized and characterized and their potential applicability in thin film Schottky barrier diodes have been examined and demonstrated accordingly. In later part, Cadmium Oxide (CdO) has been synthesized by hydrothermal route and the morphological impact of the derived CdO on charge conduction and relaxation within Schottky diode is investigated by using bias-dependent impedance spectroscopy (IS). This thesis work has focused not only on the synthesis and characterizations of the above semiconductors but also focused on the optoelectronic device fabrication followed by the investigation of the charge transport properties via impedance spectroscopy (IS) and analysis of current-voltage (I-V) data.

In the prolonged course of these experimental studies, the charge transport mechanism through Al/$CuInSe_2$ is extensively analyzed by employing space charge limited current (SCLC) theory. It has been observed that after illumination of light the mobility is increased ~5 fold. Over all, the experimental analysis involved me to get insights into the charge transport mechanism, and the physics of Schottky interfaces.

The successful energy quenching and resonance energy transfer process from P3HT to $CuInSe_2$ via Fluorescence Resonance Energy Transfer (FRET) analysis by compositing P3HT:$CuInSe_2$ is established. The photo-induced charge transport phenomenon has been successfully examined through estimation of band structures along with proper band diagram. The estimate value of the Förster distance (R_0) of critical energy transfer and thorough studies of absorption and emission spectra highly ensured the possibility of resonance energy transfer from P3HT to $CuInSe_2$ in context to fabricate efficient photovoltaics.

Meticulous computational investigations revealed that, the hetero-junctions of the configuration TiO_2/$CuInSe_2$ and HF-TiO_2/$CuInSe_2$ junctions show p-n diode like behavior in compare to the first kind of device, the second one is more efficient towards the light response.

Partha Pratim Ray
(Prof. Partha Pratim Ray)

Animesh Layek
(Dr. Animesh Layek)

Animesh Biswas
Animesh Biswas

24/09/24
Dr. Partha Pratim Ray
Professor
Department of Physics
Jadavpur University

Dr. Animesh Layek
Assistant Professor
Department of Physics
Jadavpur University
Kolkata - 700032

*To my **FAMILY**, whose unwavering love, support and encouragement have been the cornerstone of my journey…*

ACKNOWLEDGEMENT

The completion of this thesis represents not only the fulfillment of an academic journey but also the culmination of years of persistence, growth, challenges, and transformation. It has been a path filled by many highs and lows, and along the way, I have been fortunate to receive unwavering support, guidance, and encouragement from numerous individuals and institutions. I am profoundly grateful to each and every person who has contributed to the success of this endeavor in their unique way.

First and foremost, I wish to express my deepest appreciation to my supervisors, Prof. Partha Pratim Ray and Dr. Animesh Layek. Their expertise, patience, and unwavering commitment to my growth as a researcher have been the bedrock of this thesis. From the very beginning, they gave me the flexibility to explore ideas freely, providing just the right direction and constructive criticism. Their meticulous attention to detail, insightful questions, and high academic standards continually pushed me to refine my work. They have been more than advisors—they have been like a mentor, a motivator, and an inspiration. The countless hours they spent discussing concepts, revising drafts, and offering encouragement will forever be remembered with the deepest gratitude.

I would like to extend my thanks to my former lab mates who have contributed immensely to this thesis. The bond of friendship cultivated in the laboratory and the fruitful scientific interactions have collectively enhanced my Ph.D. experience. A mere thanks would not be enough to express my deepest gratitude to Dr. Arka Dey and Dr. Sayantan Sil for their insightful suggestions, constant support, and for always being available when I needed advice or a sounding board. I would like to convey my sincere thanks to Dr. Joydeep Datta, Dr. Mrinmay Das, Dr. Rajkumar Jana and Dr. Joydeep Dhar for the collaborative discussions, encouragement, guidance and steady support they provided to help me to stay focused and driven throughout this journey. I would like to thank Dr. Dhananjoy Das and Mr. Moinak Das, two of my younger lab mates, for being there to help me in any form whenever I needed. My gratitude further extends to my other lab mates - Dr. Pubali Das, Ms. Baishakhi Pal, Dr. Jitendra Kumar, Mr. Ramjan Sk. and Mr. Supravat Ghosh for the friendship and happy times

we've spent that have shaped our collective experience. I have spent many wonderful moments with all of you and it will remain in my heart forever.

I am grateful to the members of my research advisory committee, Prof. Sanjay Kumar, former and present Heads of the department of physics Prof. Sukhen Das, Prof. Kalyan Kumar Chattopadhyay and Prof. Nabin Baran Manik, whose thoughtful and challenging feedback helped me to look at my work through a broader lens and ensured that this thesis achieved the rigor it required. My sincerest thanks also go to the Department of Physics, Jadavpur University, the office staff, and the research and Ph.D. sections. Their administrative support has been invaluable. For his unparallel support in academic and administrative concerns, Mr. Azizur Rahaman (Ph. D. Cell) deserves a special recognition. The resources, academic opportunities, and support offered by this institution have been invaluable in enabling me to pursue this research.

In my PhD tenure, I got the opportunity to work in collaboration with Prof. Shouvik Chattopadhyay (Jadavpur University, Kolkata) and Dr. Biswajit Dey (Visva Bharati). I want to express my deep gratitude to them for giving me the opportunity. It has been a learning experience for me.

My heartfelt thanks go to my colleagues and peers in Sreegopal Banerjee college. The sense of community we have cultivated over the years has been a cornerstone of my academic experience. Whether it was through formal collaborations, informal discussions, or simply sharing in the day-to-day struggles, they have all been a significant part of this journey. I am particularly grateful to Dr. Animesh Das, Dr. Rima Pal and Dr. Biplab Goswami for their unwavering support, encouragement and advice. I would like to offer my heartfelt thanks to Dr. Angshuman Biswas, who has not only been a colleague but also like an elder brother to me throughout this journey. His wisdom, guidance, and constant support have been instrumental in both my personal and professional development. I am deeply grateful for the countless moments of mentorship, encouragement, and friendship that have enriched my life and this work. His belief in me, combined with his generous spirit, has been a constant source of inspiration. For all of this, I will always be thankful.

On a personal level, I am incredibly fortunate to have had the unwavering support of my family. Words cannot fully express the depth of my gratitude. Their belief in me, even when I doubted myself, gave me the strength to persevere. They have always encouraged me

to dream big and have supported those dreams with love, sacrifice, and unending patience. Their pride in my accomplishments has been a constant source of motivation and joy. Special respect and gratefulness is owed to my elder brother, Mr. Arobindu Biswas, for his encouragement and for always being a source of strength, and comfort. I want to deeply appreciate my wife, Mrs. Priyanka Biswas, for being my biggest source of strength along this journey with her constant love, support, and encouragement. Her understanding, perseverance, and confidence in me allowed me to achieve this. She stood firm in her support, lending her advice and consolation at the most difficult times and just when I needed it the most. This dissertation is a result of both my diligence and her encouragement.

Lastly, I wish to acknowledge everyone who has contributed to this work in ways both big and small, including those whose names may not be mentioned here. Whether you offered a word of encouragement, helped with logistics, or simply shared in the journey, your support has not gone unnoticed. This thesis is as much a product of your kindness and generosity as it is of my own efforts.

To everyone who played a part in this journey—thank you from the bottom of my heart.

Animesh Biswas

(Animesh Biswas)

Contents

List of Abbreviations

3-D	Three Dimensional
AC	Alternating Current
B.E.	Binding Energy
CB	Conduction Band
CIS	Copper Indium Selenide ($CuInSe_2$)
HF	Hydrogen Fluoride
CNT	Carbon Nanotube
CV	Cyclic Voltammetry
CVD	Chemical Vapour Deposition
DC	Direct Current
DI	Deionized
DMF	Dimethylformamide
EDX	Energy Dispersive X-ray Spectroscopy
EIS	Electrochemical Impedance Spectroscopy
e-h$^+$	Electron-hole
PVD	Physical Vapour Deposition
HT	Hydrothermal
IPA	Isopropyl alcohol
I-V	Current-voltage
IR	Infrared
IS	Impedance Spectroscopy
ITO	Indium tin oxide
JCPDS	Joint Committee on Powder Diffraction Standards
kV	Kilo Volt
LED	Light Emitting Diode
HOMO	Highest Occupied Molecular Orbital
LUMO	Lowest Unoccupied Molecular Orbital
MS	Metal-Semiconductor
NCs	Nanocomposites
NPs	Nanoparticles
PL	Photoluminescence

R.T.	Room temperature
SDs	Schottky Diodes
SMU	Source Measuring Unit
SCLC	Space Charge Limited Current
S.I.	Supplementary Information
TE	Thermionic Emission
TEM	Transmission Electron Microscopy
UV	Ultraviolet
VB	Valence Band
wt%	Weight Percent
XPS	X-ray Photoelectron Spectroscopy
XRD	X-ray Diffraction

Preface

This thesis is not only the outcome of my laboratory work but also the evidence of the detail understanding about the dynamical behavior of two different kinds of nanomaterials. This report is a note of the efforts that help me to develop my technical skill related with material characterizations. The materials, those attracted me because of their potential applicability in optoelectronic devices, had submitted its candidature to harvest renewable energy from the Sun.

For the sake of conservation of energy, a low cost sustainable power source is extremely essential for the wellbeing of the human kind. The conventional solar cells being very costly, it requires a search for advanced materials for solar energy conversion. Photovoltaic cells based on I–III–VI_2 compounds have shown a lot of promises for solar energy harvesting. Copper indium selenide ($CuInSe_2$) is one of those promising materials because of its alluring properties such as high optical absorption, suitable band gap which are essentially ideal for the photovoltaic and optoelectronic device applications. This material has gained much attention in research because of its good stability under radiation and low toxicity. Furthermore, the energy band gap of $CuInSe_2$ can also be tuned within the range 1.00 eV to 1.68 eV by tailoring the synthesis process.

Again, II-VI inorganic nanoparticles present great scientific and technological values in fabricating frequency-controlled portable electronic devices mostly due to their unique physical and chemical features deriving from their nanoscale size and morphology. The size and morphology dependent behavior makes them potential candidate for applications in several areas of research, specifically in optoelectronics and other applications including solar cells, photodiodes, and transparent electrodes and gas sensors.

This dissertation includes seven chapters in which I have illustrated the synthesis and characterization of the semiconductor nanomaterials $CuInSe_2$(I-III-VI_2) and CdO (II-VI). I have demonstrated its application in thin film Schottky barrier diodes and studied various properties via theoretical analysis of the experimental data. To study the morphological impact of CdO on carrier conduction and relaxation within junction device, it has been synthesized by Solvothermal route and investigated by using bias-dependent impedance spectroscopy.

Chapter 1 introduces the overview of past scientific efforts of finding the promises of inorganic I-III-VI_2 and II-VI semiconductors nanomaterials and their potential applicability in photo-electronic devices. An elaborative discussion on nanomaterials, nanocomposites and their advantages, challenges and opportunities is encompassed herewith. The chapter explains wide details of past and present synthesis methodological procedures of I-III-VI_2 and II-VI semiconductors nanomaterials. It enlightens on unique and important features of $CuInSe_2$.

The basic theory related to the various characterization, used in this thesis are illustrated in **Chapter 2**. Structural characterization has played an important role to identify the synthesized material and demonstrates the morphological analysis. Whereas the optical characterization has given an idea about the optical band gap energy and explored the dispersive and dielectric behavior of the synthesized material. A theoretical introduction of Schottky barrier diode and Impedance Spectroscopy (IS) analysis has been provided in detail. The device fabrication technique has also been discussed in this chapter. The electrical characterization using current voltage and impedance study has facilitated to get the insight of the charge transport mechanism of the material thin film and fabricated Schottky device. In the end, an overview of cyclic voltammetry has been provided which helps to estimate of HOMO-LUMO position of the synthesized material.

Chapter 3 describes the synthesis procedure of Copper Indium Selenide ($CuInSe_2$) and the fabrication of Schottky diode (SD) by using the material. The interface characteristics of Al/$CuInSe_2$/ITO have been investigated with the help of ac impedance spectroscopy (IS) analysis and dc current-voltage (I-V) measurements. The ac impedance spectroscopy (IS) helps to investigate and analyze the impedance at the boundary regions of SDs. From I-V characteristics, important parameters such as ideality factor (η), photosensitivity, barrier height (Φ_b), series resistance (R_S) of SD were obtained under dark and photo condition.

Chapter 4 reports the fluorescence resonance energy transfer mechanism for photo induced charge transfer from P3HT to solvothermally derived $CuInSe_2$. The HOMO and LUMO energy states of $CuInSe_2$ has also been determined from cyclic voltammetry and optical study. This HOMO-LUMO position agrees to select P3HT polymer as possible donor of excitons. Steady-state luminescence study of composite (P3HT:$CuInSe_2$) demonstrates possibility of successful charge transfer. To get insight the state of quenching, the

Photoluminescence spectra have been analyzed according to Stern–Volmer method. The Förster distance (R_0) of critical energy transfer has been estimated which ensures energy transfer from P3HT to $CuInSe_2$.

Chapter 5 includes the current rectification behavior of $CuInSe_2/TiO_2$ hetero-junction, identical to the I-V characteristics of p-n junction diode and the impact of white light on it. It has been discussed that how the current-rectification ratio of the configuration $Al/CuInSe_2/TiO_2$ /ITO is improved on white light illumination which actually offering an unprecedented way to realize the $CuInSe_2/TiO_2$ hetero-junction as photo-sensing p-n diode. How the device performance is improved further by replacing TiO_2 with HF treated TiO_2 has also been studied.

Chapter 6 describes the synthesis procedure of Cadmium Oxide (CdO). Two different crystallite size based CdOs are derived from hydrothermal route at different temperatures. The morphological impact of derived CdO on charge conduction and relaxation by using bias-dependent impedance spectroscopy (IS) has been investigated. Materials have been characterized by XRD, FESEM, UV-Vis spectroscopy technique. The dc conductivity is also evaluated by measuring current-voltage characteristics, and bias-dependent Impedance Spectroscopy at room temperature, which concludes the CdO with larger crystallite size, dominate the conduction mechanism.

An overview and conclusion of the entire work has been drawn in **Chapter 7.**

The **references** in this thesis are given in the following format:

Initial and surname of the authors, *Name of the Journal,* Year, **Volume,** Page number.
Example: A. Biswas, S. Sil, A. Dey, J. Datta, D. Das and P. P. Ray, *Journal of Physics and Chemistry of Solids*, 2021, **150**, 109878.

Books: Author, *Title*, Publisher, Place Published, Year.
Example: E. H. Rhoderick, *Metal-Semiconductor Contacts*, Clarendon Press, Oxford, 1978.

Book Section: Authors, *Chapter Title*, Publisher, Year, pp. Pages.

Example: J. H. Werner and U. Rau, in *Silicon-Based Millimeter-Wave Devices*, Springer, 1994, pp. 89-148.

Due acknowledgment has been given to the results of researchers in the relevant field, in accordance with the standard procedure for publishing scientific observations. Any inadvertent mistake or oversight that may have slipped in must be accepted as my fault.

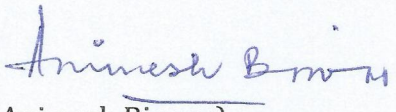

September 2024 (Animesh Biswas)

Chapter 1

Introduction

1.1. Promises of Inorganic Materials on Photo-electronic Devices

The influence of inorganic materials on civilization is extensive and wide-ranging, particularly when it comes to their promising use in photo-electronic systems. Specially these materials are essential to the advancement of technologies that boost economic growth, improve quality of life, and support environmental sustainability because of their remarkable electrical and optical capabilities. A new era of innovation and advancement in photo-electronic devices has been ushered by inorganic semiconductor materials, which provide unmatched advantages across several technological domains and societal dimensions. These materials, which stand out for their remarkable optical and electrical characteristics, provide the foundation for creating solar cells of high-efficiency, LEDs, photodetectors, LASER, diodes etc.[1-8] These are few examples of devices that take advantage of the special qualities of inorganic materials. Their flexibility extends their possibilities to a broad spectrum of applications. These materials may be seamlessly integrated with present-day technologies, such as Complementary Metal-Oxide-Semiconductor (CMOS) techniques,[9-11] to enable the creation of hybrid devices that combine the advantages of inorganic and organic compounds. In recent past to improve the brightness and energy efficiency of consumer devices, the display technology, by incorporating inorganic LEDs, has taken an excellent role.[12-15] Inorganic quantum dots are used to improve the brightness and color purity of displays, which propels improvements in screens of television and smartphone.[12, 16-18] The exceptional efficacy, resilience, adjustable characteristics, and adaptability of inorganic semiconductor materials, make them very significant and essential for the progression of contemporary technology. Therefore, the promises held by inorganic materials are numerous and include energy production, economic expansion, environmental sustainability, and general well-being of mankind.

Solar energy is becoming an appealing alternative to fossil fuels due to its exceptional efficiency of directly converting sunlight into electricity. By lowering air pollution, mitigating climate change, and reducing greenhouse gas emissions, this shift improves environmental and public health.[19, 20] To find the source of renewable energy materials is a tantalizing objective for Scientist and Researchers. It is obvious that the production of renewable energy is one of the most important societal effects of inorganic materials. A key component of the

worldwide transition to sustainable energy is the use of solar cells, which are mostly composed of silicon and other inorganic semiconductors.[21-24]

Environmentally, these materials support a circular economy by reducing ecological footprints through non-toxic manufacture and recycling programs. Their longevity reduces electronic waste. Ongoing research and development in this field ensure continuous innovation, fostering sustainable progress and improving global quality of life day by day. Undoubtedly, it greatly improves the performance and efficiency, which was essential for the advancement of photo-electronic devices.

Technology makes devices more capable of satisfying the changing demands of society followed by the chemical modification of the materials. A key concept in the modification of inorganic materials is doping. This is the process of introducing controlled impurities into a material's crystal lattice to change its electrical characteristics. To maximize the performance and efficiency of optoelectronic devices, doping silicon with phosphorus or boron, for example, leads to n-type and p-type materials, respectively.[25] Nanostructuring is another essential modification technique that uses material manipulation at the nanoscale to maximize certain qualities and take use of quantum mechanical processes. The size and surface characteristics of nanomaterials, such as quantum dots and nanowires, give rise to distinctive optical and electrical properties. For example, nanowires and nanotubes offer improved surface areas and charge transport channels, enhancing light absorption and efficiency in photodetectors and solar cells, while quantum dots offer adjustable emission wavelengths, perfect for high-definition displays and biomedical imaging. Another crucial modification method is surface passivation, which reduces charge carrier recombination by adding thin coatings of oxides or nitrides to semiconductor surfaces. This improves the stability and performance of inorganic materials in electronic devices. For example, passivating $CuInSe_2$ with titanium dioxide (TiO_2)[26] prolongs carrier longevity and improves device efficiency by reducing recombination centers. Inorganic components are combined with other materials, such polymers or ceramics, to make composite materials, which offer synergistic properties that individual elements cannot generate on their own. Composites are used in photo-electronic devices to increase device durability, reduce production expenses, and broaden application possibilities.

Another important way to change inorganic materials is by alloying, which is the process of combining two or more elements to produce alloys with certain characteristics. Cu(In,Ga)Se_2 (CIGS), for example, is created by alloying copper indium selenium ($CuInSe_2$) with gallium (Ga). By adjusting the Ga concentration, the band gap might be controlled from around 1.0 eV ($CuInSe_2$) to 1.7 eV ($CuGaSe_2$).[27-29] By improving the match with the solar spectrum, the tuning raises the efficiency of solar cells.[30] In applications where certain emission wavelengths are needed, this adjustment is essential for maximizing the performance of LEDs and laser diodes. Through the deposition of precise layers with regulated characteristics, thin film methods such as chemical vapor deposition (CVD) and molecular beam epitaxy (MBE) are essential for the modification of inorganic materials. These methods offer multi-junction solar cells with high conversion efficiencies by enabling the production of superior thin films, which are necessary for cutting-edge photovoltaic systems. Photo-electronic devices must consider the sustainability of the inorganic nano-materials used in their construction in order to reduce environmental impact, save resources, and ensure long-term viability; which is very crucial in the context of technological growth.

1.2. Nanomaterials and Nanocomposites

The history of nanomaterials effectively began when nanostructures first formed in early meteorites following the big bang. Later, the nature evolved many other nanostructures, such as skeletons and seashells.[31, 32] Nanoscaled smoke particles were formed during the use of fire by early humans. However, the scientific investigation of nanomaterials started much later. Michael Faraday synthesized colloidal gold particles as early as 1857,[33] which was one of the first scientific reports. For more than 70 years, researchers have been investigating nanostructured catalysts. Precipitated and fumed silica nanoparticles were manufactured and marketed in the United States and Germany by the early 1940s as an alternative to ultrafine carbon black for rubber reinforcements.[34, 35]

Both industry and academics have shown a great deal of interest in nanomaterials during the past three decades.[36, 37] The necessity for answers in real-life situations, where present approaches were encountering constraints, was the motivation behind this.

Improvements in characterization and processing methods helped scientists in their assessment of theoretical research on nanomaterials and this development made more sophisticated tools available for investigating and dealing with the nanoscale environment.[38, 39] Generally, materials that have at least one dimension in the nanometer (1 nm = 10^{-9} m) range are considered as nanomaterials.[40] This length scale, which falls between the atomic and the microscale, brings new physical and chemical properties to a material. This becomes notably evident when the nanomaterial has at least one dimension between 1 and 100 nm.[41]

Therefore, it has become widely accepted that the word "nanomaterial" refers to this very precise range. Nanomaterials can be either natural or synthesized (engineered nanomaterials). Examples for naturally occurring nanomaterials are volcanic ash, soot from forest fires, etc.[42-44] Engineered nanomaterials may be divided into many categories based on their shape and composition. The structural characteristics of their constituent components and the amount of dimensions that are outside the nanoscale provide a useful framework for classifying them. Depending on the size and shape, nanomaterials are classified into 0-D (quantam dots, nanoparticles), 1-D (carbon nanotubes, nanorods, and nanowires), 2-D (nanofilms), and 3-D nanomaterials, when 0-D, 1-D, and 2-D nanomaterials come into close contact to form interfaces (powders, fibrous, multilayer, and polycrystalline materials).[45, 46] The different arrangements of nanomaterials may create a wide range of nanostructures that are distinguished by their observable shape and dimensions. Consequently, for instance, a linear or a planar bonding of nanoparticles of a certain composition results in the production of a one-dimensional or two-dimensional nanostructured material, respectively.[47] Furthermore, strategies for the production of nano devices can be derived from the construction of ordered arrays of nanostructures.[48] In general, the surface area of a nanomaterial has a greater influence on its performance than its composition. The Recent developments in nanotechnology allow us to create nanomaterials that enhance the quality of life. Carbon nanotubes (CNTs), carbon nanofibers (CNFs), graphene, fullerenes, silica, clay, metal, and metal oxide nanomaterials are a few examples of engineered nanomaterials.

Because of their exceptional properties, nanomaterials are often mixed with bulk polymeric materials to enhance their characteristics. The class of nanocomposites is defined as the combination of two or more phases or components having distinct physical or

chemical characteristics, where at least one of these components is in the nanometer scale and resulting in differentiated properties compared to the individual elements. These present improved properties compared to their respective microcomposites are primarily attributed to the size effects of the nanomaterials involved.[49] The distinguished category of nanocomposites involves dispersing at least one discontinuous nanosized phase within a continuous medium, typically referred to as the matrix. Based on the type of matrix material used, nanocomposites are classified into polymer matrix composites, metal matrix composites, and ceramic matrix composites. The most crucial factor to take into account in polymer matrix composites is the dispersion of the nanofillers in the bulk polymer matrix. Improved properties arise from a homogeneous dispersion of nanoparticles. However, the weak van der Waals interactions between the nanomaterials cause a tendency for particle agglomeration, which deteriorates the properties of the material. For instance, homogeneous dispersion of CNTs, graphene, CNFs, and clay in the polymer matrix enhanced the mechanical, thermal, electrical, optical, gas barrier, and flame retardant qualities of the Nanocomposites.[50-52] It is now widely known that surface modification or functionalization of the nanomaterials can improve their dispersion in a polymer matrix.[53, 54] Recently, it has been demonstrated that the incorporation of compatibilizer also enhance dispersion of the nanomaterials inside the polymer matrix.[51] In order to develop high-performance lightweight composites for cutting-edge applications, surface modification and functionalization of nanomaterials strengthen the interfacial interaction or compatibility between the filler and matrix. This leads to better dispersion, which in turn facilitates effective stress transfer of the matrix and filler.

1.2.1. Advantages of Nanomaterials

A wide range of areas, including electronics, sensors, energy devices, medicine, cosmetics, and catalysis, have benefited significantly from the unique optical, magnetic, electrical, and chemical properties that nanomaterials exhibit.[55-57] For instance, the development of nanomaterials has led to the creation of numerous electronic devices, including organic light emitting diodes (OLED), plasma displays, and nanotransistors. Examples of how nanomaterials have an influence on energy include solar cells, fuel cells, and high performance portable batteries. Nanomaterials can be incorporated to polymers to

make them stronger and lighter in order to create smart uniforms, nonwetting textiles, fire-retardant fabrics, self-cleaning and self-healing fabrics, lightweight, high-performance military aircraft, cars, etc.[58] Large surface area and high gas sensitivity of metallic-based nanomaterials make them very suitable for gas sensors and hydrogen storage devices.[59] The applications of nanopesticides, nanofertilizers, and nanoherbicides on crops may be beneficial.[60] Nanocatalysis is a field that is expanding rapidly. Nanomaterials are an appealing catalyst choice due to their large surface area and excellent surface activity.

1.2.2. Challenges and Opportunities

Although nanomaterials have a wide range application, there are still a number of problems that need to be fixed. There is considerable worry about how nanoparticles affect the bodies of humans and animals. To address the safety concerns with nanoparticles, further investigation is necessary as there are still many unanswered questions regarding this regime. For instance, inhaling of nanoparticles may cause irritation in the lungs and increase the risk of lung damage which may lead to cancer. It is concerning when weak van der Waals forces lead nanoparticles to agglomerate. In order to preserve the characteristic properties of the nanoparticles, technology needs be developed to keep them separated. The cost of nanomaterials and their products is significantly higher than that of conventional materials. It has been proposed that the cost of nanomaterials can be reduced by extending their use in a variety of new applications, which will boost their manufacturing rate. The possibility of developing atomic weapons, which have the potential to be extremely devastating, must be understood. Nanomaterials should thus be used constructively. The extensive usage of nanoparticles in agriculture raises alarming concerns as it may release these particles into the environment and have an adverse effect on animals, plants growth, and soil fertility. Before employing metallic-based nanoparticles in gas sensors and hydrogen storage, controlling their structure and chemistry is another massive task. There are still issues with the need for new materials, performance enhancement, longer product life, and product pricing. All these facts suggest that new and advanced technologies are required to improve the performance of nanomaterials.

1.3. Group I-III-VI_2 Semiconductors: A Brief Review

It was the fact that numerous naturally occurring binary and ternary compounds exhibited behaviors currently associated with semiconductors even before the transistor was invented and this development was the reason that motivated systematic research for novel semiconductors in the early 1950s. The earliest materials investigated in this method were the III-V compounds that exhibit the diamond structure. Although InSb was reported to be a semiconductor by Blum et al. (1950)[61] and Goryunova and Obukhov (1950),[62] Welker (1952)[63] appears to be the first to recognize the significance of the III-V compounds as a new class of semiconductors.[64-67] Exploring ternary compounds with tetrahedral or diamond-like coordinate was an obvious next move in the hunt for novel semiconductors, and Goodman and Douglas (1954)[68] discussed about the potential semiconductivity in the I-III-VI_2 compounds that had been produced a year earlier by Hahn et al (1953).[69] Group I-III-VI_2 semiconductors, generally known as ternary compounds, are a family of materials that have attracted a lot of research attention owing to their distinctive optoelectronic and electrical characteristics. These semiconductors are comprised of elements from groups I (Cu, Ag), III (Al, Ga, In), and VI (Se, Te, S) of the periodic table and usually follow the formula I-III-VI_2. The synthesis and fundamental characterization of these materials were the main areas of attention during the early phases of research in the 1950s. Growing single crystals and figuring out their crystal structures were the initial tasks. Austin et al. (1956)[70] appear to be the first group systematically tries to grow large single crystals of these compounds without any cracks. They used evacuated quartz ampoules to prepare 50–100 g ingots of $AgInS_2$, $AgInSe_2$, $CuInSe_2$, $AgInTe_2$, and $CuInTe_2$. Their attempts to grow big crystals via zone melting, pulling techniques or directed solidification procedures were unsuccessful. Later, $CuInS_2$and $CuInSe_2$ compounds were synthesized and investigated by scientists John L. Shay et al. They found that these materials crystallize in the chalcopyrite structure, which is a tetragonal-distorted variant of the zinc-blend structure.[71] Group I-III-VI_2 semiconductors received a surge for attention throughout the 1960s and 1970s due to the potential applications they have in optoelectronics and photovoltaics. Better control over the material quality and composition was made possible by several significant advancements in the development of crystal growth techniques, including chemical vapor deposition (CVD) and molecular beam

epitaxy (MBE).[72] This period also witnessed the first extensive investigations of their electrical characteristics, such as bandgap measurements and carrier mobility analysis. It was found that these materials possessed a direct bandgap which makes them an ideal candidate for optoelectronic applications.[73] The understanding of Group I-III-VI_2 semiconductors and their applications in solar cell developed significantly in the 1980s. The creation of thin-film solar cells was made possible by the advancement of thin-film deposition methods such as sputtering and evaporation. $CuInSe_2$-based solar cells, in particular, exhibited encouraging efficiency, which led to an upsurge in research into improving their performance. Researchers like Ken Zweibel and Miguel A. Contreras concentrated on enhancing material quality, comprehending the function of defects, and optimizing the device architecture.[74, 75] Although their market presence was originally limited, this decade witnessed the first commercialization of $CuInSe_2$ based solar cells.[76, 77] Research on Group I-III-VI_2 semiconductors made great strides in both basic knowledge and useful applications throughout the 1990s. The utilization of alloying, such adding Ga to create $Cu(In,Ga)Se_2$ (CIGS), resulted in an additional boost in thin-film solar cells' efficiency.[78-80] Bandgap engineering was made possible by this alloying, which improved the absorption properties of material. Furthermore, a new developments in characterisation techniques, such photoluminescence spectroscopy and high-resolution transmission electron microscopy (HRTEM) provided deeper insights on microstructure and electrical characteristics of these materials.[74, 81]

Group I–III–VI_2 semiconductor technology advanced throughout the 2000s and 2010s, especially in the area of photovoltaics. CIGS solar cells exceeded conventional silicon-based solar cells with record efficiencies of over 20%. The development of manufacturing facilities for large-scale production and rising commercial interest has been driven by the scalability and cost-effectiveness of CIGS technology. Considering the unique properties of these materials, research efforts have been expanded to investigate further applications, such as light-emitting diodes (LEDs), photodetectors, and thermoelectric devices.[82-84] Enhancing the sustainability and environmental effect of Group I-III-VI_2 semiconductors has been more of a priority in recent years. To reduce the usage of hazardous metals like selenium and cadmium in the production of these semiconductors, researchers have been looking for substitute materials and manufacturing techniques.[85] Furthermore, there has

been a greater focus on creating lightweight and flexible devices, which increases the potential uses of these materials in wearable and portable electronics.[86-90]

1.4. Ternary $CuInSe_2$ Semiconductor (I-III-VI_2): Background and Motivation

Beyond just photovoltaics, ternary copper indium selenide ($CuInSe_2$) (composition of I-III-VI_2) semiconductor has attracted significant interest due to its unique electronic and optical properties which make it a versatile material for a range of technologies and photoelectronic applications, including optoelectronic devices and sensors. The background and motivation for research into $CuInSe_2$ are deeply rooted in its exceptional characteristics and the broad potential applications across different photoelectronic fields.

The story began since its inception when $CuInSe_2$, whose binary analogue $Cd_{0.5}Zn_{0.5}Se$, is one member of this family of compounds was originally studied by Hahn *et al.* in 1953.[69] Since then a considerable amount of effort has been invested to gain a better and deeper understanding of the electronic, electrical and optical properties of this material.[71, 91] In the early 1970s, when researchers started exploring new semiconductor materials for a variety of electronic and optoelectronic applications, $CuInSe_2$ was identified as potential material.[92] It crystallized in the chalcopyrite structure with lattice parameters a = 5.782Å, c = 11.620Å, with c/a = 2 at room temperature.[93] This structure is distinguished by a unique arrangement of copper, indium, and selenium atoms, which affects the electrical and physical characteristics of the material and is essential in figuring out its electronic band structure. Contrary to its II-VI binary counterparts, $CuInSe_2$ has a direct bandgap and may be produced either n- or p-type depending on the growth and annealing conditions.[92, 94] P-Type conductivity was achieved by annealing at maximum selenium pressure, while n-type conductivity has been reported[95] for samples made by in-diffusion of Cu and In. Extrinsic dopants such as Zn, Cl and Br[96] and Cd[97] act as donors when they are diffused or ion-implanted into p-type $CuInSe_2$.

The optical properties of $CuInSe_2$ are equally remarkable[98, 99] having a direct bandgap of 1.04 eV which is optimal for absorbing visible light and making it suitable for light-emitting and photo detection applications. This direct bandgap allows $CuInSe_2$ to be highly

efficient in converting photons into electrical signals, a property that is valuable not only for solar cells but also for other optoelectronic devices. It exhibits an absorption coefficient exceeding 10^5 cm^{-1} for photon energies greater than the bandgap,[100, 101] ensuring that a thin layer of the material can absorb a significant portion of the incident solar spectrum. The refractive index of $CuInSe_2$ varies with photon energy,[102] providing valuable insights into its interaction with light and guiding the design of efficient photo sensing devices.

$CuInSe_2$ has a number of challenges to mainstream use despite its intriguing characteristics.[103] Some serious concerns include the expense and availability as well as the potential environmental impact of selenium. To overcome these challenges, scientists are investigating other synthesis techniques and naturally occurring alternatives like zinc and sulfur.[104] Additionally, improving the stability and durability of $CuInSe_2$-based devices under real-world operating conditions is critical for their commercial viability.[105, 106]

The future of $CuInSe_2$ appears promising, with advancements in materials science and engineering expected to enhance its performance further. Innovations in nanostructuring, surface passivation, and interface engineering are anticipated to improve device efficiency and stability.

1.4.1. The phase relations in the Cu-In-Se system

The phase equilibrium of Cu-In-Se alloys has drawn attention because it offers a fundamental knowledge of material formation and may be used to match the parameters of technical applications based on the materials. Cu-In-Se thin films have a complex microstructure and a wide range of distinct phases, depending on the composition and processing parameters. Several researchers have investigated the Cu_2Se–In_2Se_3 system[107, 108] and majority of them believe that the stoichiometric phase of $CuInSe_2$ falls along the Cu_2Se-In_2Se_3 tie line on the ternary phase field of this system. One of more reliable pseudo-binary phase diagram that was determined by Ciszek and Fearheiley[107, 109] is shown in **Fig. 1.1.**[110] The given phase diagram indicates that a number of compounds including $Cu_2In_4Se_7$, $CuIn_3Se_5$, Cu_5InSe_4 and $CuInSe_2$ are expected to occur in this ternary system. The chalcopyrite, single-phase $CuInSe_2$ expands from a stoichiometric composition of 50 mole% In_2Se_3 to the in-rich composition of around 55 mole %In_2Se_3. The corresponding Cu/In atomic ratio for this single-phase region falls between 1.0 and 0.82. If the Cu/In atomic ratios

are larger than 1.0, the materials are expected to contain secondary phases of Cu_2Se and in contrast (Cu/In atomic ratio less than 0.82), the materials are expected to contain secondary phases of$Cu_2In_4Se_7$ and $CuIn_3Se_5$. Two solid state phase transformations have been observed by differential thermal analysis. Chalcopyrite structure has been reported to form at temperature below 810°C,[111, 112] although a second uncharacterized phase transformation has been observed at 665°C.[112] The melting point has been reported to be at 987°C.[112]

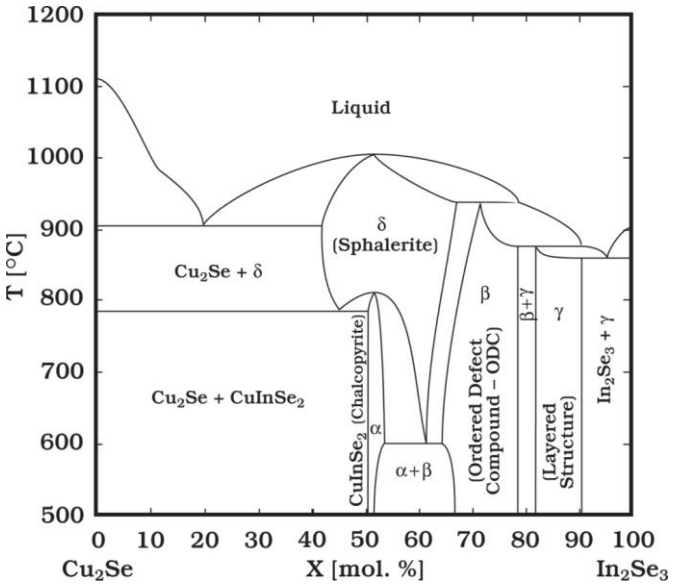

Fig. 1.1: Phase diagram along the Cu_2Se–In_2Se_3 pseudobinary section of the Cu–In–Se chemical system.

1.4.2. Crystallographic Structure of $CuInSe_2$

The Cu-In-Se composition polymorphs i.e. α-CIS, β-CIS, γ-CIS, and δ-CIS showcase different crystallographic structures each with unique atomic arrangements and coordination environments **(Annexure)**. Because of these structural differences, each polymorph has distinct electrical characteristics that make it appropriate for a variety of uses. Comprehending these variations is important in order to optimize $CuInSe_2$-based materials for particular technological uses, especially in the domains of optoelectronics and photovoltaics. In this section only the phase α-CIS system will be briefed.

1.4.2.1. α–CIS Phase (Chalcopyrite $CuInSe_2$)

The most extensively researched and technologically relevant polymorph of $CuInSe_2$ is α-CIS. It crystallizes in the tetragonally distorted zinc blende structure, known as chalcopyrite. It is classified under the space group I42d and the unit cell is characterized by lattice constants a≈5.78 Å and c≈11.62 Å, with c≈2a.[113] Within the framework of selenium (Se), copper (Cu) and indium (In) atoms occupy distinct tetrahedral positions in this structure.

The Se atoms form a distorted face-centered cubic sub-lattice. Each Se atom is tetrahedrally coordinated by two Cu and two In atoms as shown in the **Fig. 1.2.**[113]

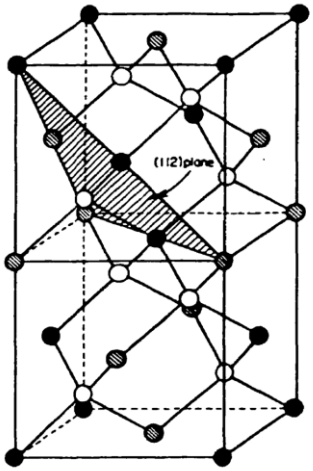

Fig. 1.2: The chalcopyrite crystal structure of $CuInSe_2$

1.4.3. Properties

In concern to the synopsis of thesis, the electrical and optical properties of Cu-In-Se compound are explored as follows:

1.4.3.1. Electrical property

The performance of $CuInSe_2$ (CIS) in optoelectronic devices is greatly influenced by a number of significant electrical characteristics that it possesses. The electrical property of ternary compounds $CuInSe_2$ is influenced by the presence of intrinsic point defects and the stoichiometry and the thermal history of the specimens are related to these defects.[114] In fact, the non-stoichiometry of the crystal governs the conductivity type of $CuInSe_2$ rather than being influenced by shallow level impurities through external doping. Thus, the donor or acceptor levels are the results of the crystal lattice defects. Copper-rich films and indium-rich films are usually reported to be p-type and n-type, respectively.[115, 116] Here it is discussed about p-type $CuInSe_2$, as it generally demonstrates p-type conductivity, arises from copper vacancies. These vacancies produce holes in the valence band where they become the primary charge carriers and contribute to create effective junctions within devices. $CuInSe_2$ exhibits significant hole mobility as well, facilitating effective charge transfer through the material itself.[117] This high mobility lowers charge carrier scattering and resistive losses, enhancing the performance of thin-film solar cells where efficient carrier transport is important. The resistivity of $CuInSe_2$ can be controlled by doping which in turn controls its electrical properties. One may tune resistivity to fit a variety of applications by changing the composition or adding different dopants. For example, doping with elements like sodium (Na) or zinc (Zn) can affect resistivity and carrier concentration, improving the compatibility of the material for particular applications.[118, 119]

By adjusting its stoichiometry or adding elements like gallium (Ga), band gap of $CuInSe_2$ may also be changed. Due to this tunability, CIS may be used in a variety of optoelectronic applications by optimizing the band gap for improved solar spectrum absorption. $Cu(In,Ga)Se_2$, for instance, is produced by alloying gallium with a band gap that may vary from around 1.0 to 1.7 eV.[120] Furthermore, CIS maintains excellent electrical performance throughout a range of temperatures,[121, 122] which adds to its reliability and longevity under various environmental circumstances. These electrical behaviors collectively make $CuInSe_2$ a versatile and effective material for optoelectronic devices.

1.4.3.2. Optical properties

Due to its exceptional optical characteristic $CuInSe_2$ is a highly desirable material for optoelectronic applications. It possesses an optical band gap of approximately 1.0 eV to 1.2 eV and can be modified to higher values by incorporation of elements like Ga.[120] Thus, according to Loferski,[123] it falls within the range of optimum band gap materials (1.1 eV <Eg<1.6 eV). Due to the excellent photon absorption made possible by this direct band gap, electrons can go directly from the valence band to the conduction band without requiring a change in momentum. As a result, CIS has a high absorption coefficient, generally greater than 10^5 cm^{-1}[100] for photons with energies above the band gap. Because of its high absorption efficiency, a thin layer of CIS may effectively photogenerate electron-hole pairs and increase photovoltaic efficiency by absorbing a wide range of the solar spectrum, including both visible and near-infrared region. A further significant optical property of $CuInSe_2$ is its moderate refractive index,[124] which amplifies details of light trapping within the material. The light trapping results multiple internal reflections, increasing the possibility of photon absorption and enhancing light utilization. Strong PL peaks near the band gap energy of $CuInSe_2$ demonstrate efficient radiative recombination of electron-hole pairs.[125, 126] The intensity and position of these peaks can reveal defect levels, impurity states, and carrier recombination processes as reported earlier. Precise and strong PL peaks indicate reduced defect densities and superior crystalline material with few non-radiative recombination centers. These properties of $CuInSe_2$ make the material an outstanding one for various advanced optoelectronic applications.

1.4.4. Growth techniques of $CuInSe_2$

The scientists and researchers have been paying their skill based effort to produce $CuInSe_2$ in different chemical and technical routes in surging it for the application for mankind. Here are few glimpses:

1.4.4.1. Hydrothermal Method

The hydrothermal method is a bulk growth technique that is used in a closed system to create the necessary chemicals at high pressures (above 1 atm) and temperatures (above 100°C). The desired materials would be practically insoluble in the water solution as a result of the physical and chemical processes that occur during the entire process. The resultant compounds depend on the pH of the medium, the time duration, the temperature of the growth process and the pressure in the closed system. The final compounds depend on the pressure inside the closed system, the temperature of the development process, the time duration and the pH of the medium.

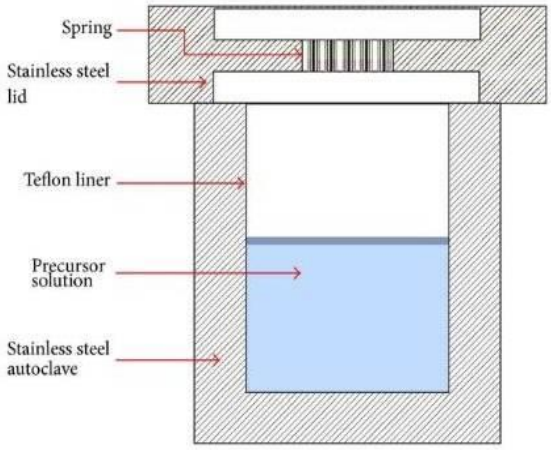

Fig.1.3: Schematic diagram of the auto clave used in solvothermal

One type of reaction vessel where the growth process is carried out under hydrothermal conditions is the autoclave. The material used in the autoclave is carefully chosen to withstand the extremely corrosive water solvent at high temperatures and pressures for a longer period of time. To prevent solution corrosion, autoclaves are often equipped with the most widely used lining material, Teflon, from inside. In order to achieve a hermetic sealing during the expansion at a higher temperature, the Teflon liner is very carefully installed inside the autoclave. **Fig. 1.3** (Adapted from[127]) depicts a Teflon lined steel autoclave for the hydrothermal and solvothermal synthesis.

It is possible to directly create nanoparticles of different chemicals by hydrolysis reactions in a high-temperature autoclave. The products derived from solution reactions can

also be subjected to a hydrothermal treatment under ambient conditions. The aqueous solution containing precursor salts (carbonate, sulfide, acetate, oxide, etc.) fill up more than 50% of the total capacity of Teflon liner in the autoclave used for the direct synthesis process. For the second case, the aqueous medium that contains the reaction product suspension is filled to half of the capacity of the autoclave. Typically, amorphous phases of bulk semiconductor compounds crystallize more quickly after undergoing this partial hydrothermal treatment step.

The hydrothermal method of crystal growth has many advantages:

(1) it uses a closed system, making it easier to control oxidization or maintain conditions that allow the synthesis of phases, which could be difficult to achieve with other methods; (2) crystals grow under lower thermal strain, which may also result in a lower dislocation density than when the crystals are grown from melts, which have large thermal gradients;
(3) the method has been proven to be useful for synthesizing the so-called low-temperature phases;
(4) it might be used to the large-scale synthesis of magnetic, optical, piezoelectric, clay, and many other novel materials,
(5) Hydrothermal synthesis produces massive, purer, and dislocation-free crystals rather quickly due to quick convection and incredibly effective solute transfer.

1.4.4.2. Solvothermal Method

Similar to hydrothermal synthesis, solvothermal synthesis uses organic reagents in place of water. **Fig. 1.4** depicts technical details for the hydrothermal and solvothermal synthesis schematically. Solvothermal synthesis is preferable than other techniques in several of reasons. First, rapid convection in solution is made possible by solvothermal conditions. The relatively mild environment makes it possible to create crystals with minimal lattice defects and permits exact control over the distribution of sizes, shapes, and

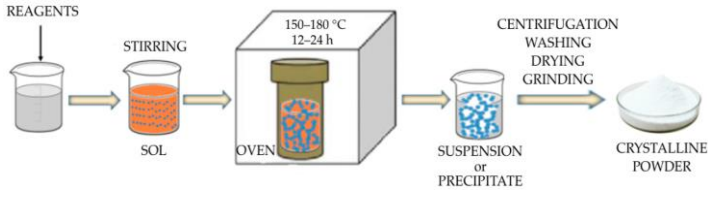

Fig.1.4: Schematic diagram of solvothermal synthesis route

crystallinity of nanoparticles. Second, when carried out at high temperatures, the low boiling point of organic solvent can give a larger reaction pressure, which can help in the crystallization process. Third, the mild temperature permits the transfer of unique structural characteristics from the precursors to the products enabling the control of the products' morphology. Additionally, solvents can supply functional groups, which can then react with the products or precursors to create new compounds. Lastly, solvothermal synthesis may reduce the release of hazardous vapour during some reaction systems, such as the one with poisonous starting ingredients. In addition to helping to practice "green chemistry," the sealed system effectively lowers the risk of oxidation and contamination from the air or oxygen, which is crucial for high-purity products.

1.4.4.3. Chemical vapor deposition (CVD)

Chemical Vapor Deposition (CVD) is a commonly used method for the synthesis of numerous materials, including thin films, semiconductors, and nanocomposites. Through a chemical reaction that takes place on a heated substrate surface, a thin layer is deposited from a gaseous phase in the CVD process. A brief schematic diagram of CVD technique is illustrated in **Fig. 1.5.**

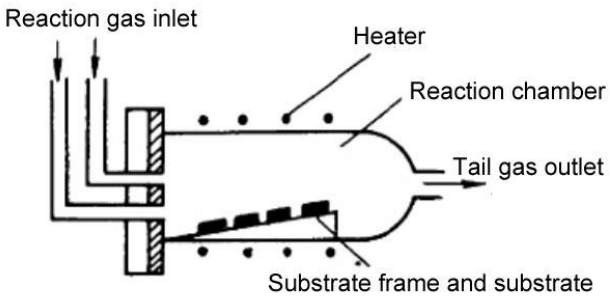

Fig.1.5: Schematic diagram of CVD route

Several CVD techniques have been used to manufacture high-quality $CuInSe_2$ thin films.[128] Metalorganic precursors for copper (Cu) and indium (In) are employed in metalorganic chemical vapour deposition (MOCVD), where they react with hydrogen selenide (H_2Se) to generate a $CuInSe_2$ layer with a controlled thickness and composition.[129] Jones et al. used plasma-enhanced chemical vapour deposition to create stoichiometric CIS films.[130] The gaseous reactant mixture, that is kept under a radio frequency (RF) plasma at a pressure of 0.1 to 1 torr, produces a glow discharge in this particular case. Close space chemical vapour transort (CSCVT) has also been used to create $CuInSe_2$.[128] In CSCVT, a sintered CIS source is mixed with a gas, hydrogen iodide, to create a volatile chemical. Following that, this volatile species

reacts chemically in the opposite way on the substrate to produce homogenous $CuInSe_2$ thin films.

1.4.4.4. Molecular beam epitaxy (MBE)

MBE emerged at the beginning of the 1970s to produce high-purity and high-quality compound semiconductor epitaxial layers on certain substrates.[131] A brief schematic diagram of MBE technique is illustrated in **Fig. 1.6.**

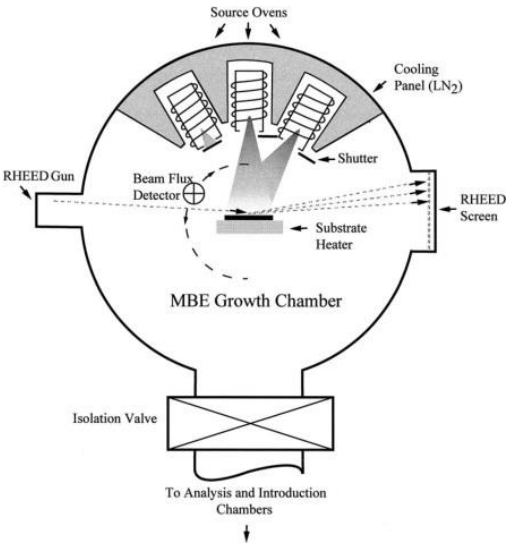

Fig.1.6: Schematic diagram of MBE technique

Almost all semiconductor epilayers have been developed using this significant approach thus far. MBE has produced $CuInSe_2$ films of superior quality.[132] Basically, an MBE is vacuum evaporation equipment with a chamber pressure maintained at below ≈ 10^{-11} torr. Certain features of MBE are usually seen as advantageous for the growth of semiconducting films, including: The extremely low growth temperature reduces any unwanted thermally activated strategies, such as diffusion. The epilayer thickness can be precisely controlled, and the introduction of various vapor species to change the alloy composition and regulate the dopant awareness can be easily carried out by incorporating separate beam cells with the appropriate shutters. These roles prove to be very crucial for creating structures including junctions.

1.4.4.5. Other conventional growth techniques

Numerous different methods are used in addition of the above-mentioned techniques to grow the crystal of ternary $CuInSe_2$ chalcopyrite compounds. Thermal evaporation**,** sputtering, pulsed laser deposition (PLD), spray pyrolysis technique, chemical bath deposition, etc. are very common method to grow $CuInSe_2$ compounds. Thermal evaporation is the most widely used technique for creating $CuInSe_2$ thin films among them. Electrical heating is used in a vacuum method to evaporate elemental Cu, In, and Se, or certain

compounds containing all three of these elements. The atoms that have evaporated follow a straight line until they collide with the substrate and create the expected $CuInSe_2$ thin film. Heating the substrate during evaporation might be performed in a sequential or simultaneous manner to enhance the quality of the layers.[133] Sputter deposition is a vacuum process that consists of the ejection of atoms from a material through the collision of fast non-reactive ions with its surface. The growth of $CuInSe_2$ by the spray pyrolysis technique involves spraying a solution containing soluble salts of copper and indium and N, N-dimethyl selenourea (NDSU) onto a heated substrate. The sprayed droplets undergo pyrolytic decomposition and subsequent reactions at the surface of the substrate to form a well-crystallized thin film. Excess NDSU over stoichiometric amount is used to compensate for the loss of selenium during pyrolysis.[134] Chemical bath deposition involves producing the required ions in a solution by chemical means, which combine and precipitate out onto the substrate, if the right equilibrium conditions are met.[135]

This research work is also subject to find out the hidden dynamic characteristics of II-VI ternary nanomaterials. Thereafter, the details of the work are introduced as follows:

1.5. II-VI Semiconductor: A Brief Review

The discovery of phosphorescence property of ZnS crystal in 1866, may be considered as the beginning of journey towards the research on II-VI semiconductors. However, in 1920, research on the luminescence and optical characteristics of II-VI semiconductors, such as ZnS, began, and these materials are still being thoroughly studied in the present day. For many years, the scientific world was unable to employ II-VI semiconductors in devices like lasers and LEDs because they were difficult to dope. The problem of doping in II-VI semiconductors was initially tackled by researchers in 1950. By the end of 1970, growth technique advancements had improved the quality of II-VI compound crystal. The development of metal organic vapor phase epitaxy and molecular beam epitaxy has accelerated up the process of characterizing the material properties. However, the doping issue remained unresolved. The first time ZnSe was doped as p-type was in 1991,[136] and eventually a blue LED was created using that particular p-type ZnSe semiconductor.[137] The researchers were motivated by this achievement to investigate novel

characteristics of II-VI and III-V semiconductors. Since then, researchers have concentrated on the fundamental dominating aspects for doping into II-VI semiconductors in addition to trying to maximize the efficiency of semiconductor devices. ZnS, ZnSe, CdS, and ZnTe semiconductors were found to become n-type, whereas ZnTe was doped as p-type. In general, acceptor impurities are compensated by vacancies on anion sites, while donor impurities are compensated by the acceptor-like behavior of the cation vacancies. Doping a semiconductor caused vacancies similar to native defect development and minimized the impact of impurities. Mandel developed a hypothesis of "Self-Compensation Limited Conductivity in Binary Semiconductors" in 1964, expanding on the concept of impurity compensation by doping.[138] The theory suggests that doping in II-VI compounds is impossible when they are unable to overcome the self-compensation threshold, which corresponds to the bond energy. An important addition to the optoelectronic application has been the ability to tune the band gap energy and other characteristics of II-VI ternary material. Hence, by varying the nanostructure, growth technique, and application to various devices, research on II-VI ternary nanomaterials continues to advance.

1.5.1. II-VI Oxide Semiconductor (CdO): Overview

The II-VI semiconductor cadmium oxide (CdO) possesses a cubic crystalline structure with a direct bandgap that ranges from 2.2 to 2.5 eV with high electrical conductivity. Its increased grain size at high substrate temperatures, moderate electron mobility, and high carrier concentration all contribute to its excellent electrical conductivity. Some process parameters, such as film thickness, substrate temperature, and solution flow rate, may be controlled to precisely regulate the characteristics of CdO for specific applications. Though CdO was the first transparent conducting oxide film that Bedekar studied in 1907,[139-141] it's been a while since there were many investigations conducted. In the past several years, CdO has been the subject of intense research in both bulk and thin-film form. CdO is an ideal choice owing to its exceptional electrical conductivity and transparency in the visible spectrum for optoelectronics[142] and other applications including solar cells[143] photodiodes[144] and transparent electrodes.[145] Furthermore, CdO is used in photodetectors and gas sensors[146] due to its sensitivity to environmental changes. Owing to its adaptable flexibility, several attempts have been made to grow CdO nanoparticles by customizing different synthesis methods including chemical

bath deposition,[147] electrodeposition,[148] chemical spray pyrolysis,[149] solvothermal technique.[150] In this dissertation, hydrothermal approach has been adopted, which is an effective choice for industrial application and much more straightforward and affordable than other traditional methods.

But the toxicity of cadmium prevents it from being used in much larger quantities, which causes environmental and health issues.[151] The goal of current research is to maximize the performance of CdO in these applications while simultaneously investigating substitute materials that could provide comparable advantages without the corresponding dangers. CdO is still a material of interest in optoelectronics and advanced electronics despite its difficulties, especially in applications where its special qualities may be used in a safe manner.

In this thesis, therefore, two different crystallite size based Cadmium Oxide (CdO)s have been synthesized via hydrothermal route at two different temperatures, 500^0C and 600^0C. The influence of crystallite size of derived Cadmium Oxide (CdO)s upon the conduction and relaxation mechanism have been studied in detail. Impedance behavior has been investigated which approved the better conducting performance of CdO derived at a higher temperature. Moreover, the relaxation time for grain and grain boundary also decreases for the sample derived from higher temperatures. The work explored the experimental and theoretical view of relaxation and conduction mechanism and offers insightful information about the behavioral and morphological impacts of synthesized CdO in different aspects.

1.6. Outline of the thesis

This thesis covered synthesis and characterization study of I-II-VI_2 ternary $CuInSe_2$ and group II-VI oxide material CdO nanocomposites and their improvisation in charge transfer phenomena. Lots of studies about the structural to electrical properties of the above mentioned semiconductors have been already done by various researchers. But the charge transfer dynamics and conduction kinetics within the junction devices based on these semiconductor nanocomposites has been the main focus of this dissertation. A thorough Theoretical study and their Experimental verification have been provided in different

chapters. First chapter introduces the overview of past scientific efforts of finding the promises of inorganic I-III-VI_2 and II-VI semiconductors nanomaterials and their potential applicability in photo-electronic devices. An elaborative discussion on nanomaterials, nanocomposites and their advantages, challenges and opportunities is encompassed herewith. Second chapter illustrates the basic theories related to the various characterizations, used in this thesis. Third chapter describes the synthesis procedure of Copper Indium Selenide ($CuInSe_2$) and the fabrication of Schottky diode (SD) by using the material. Various characteristics of SD have been investigated with the help of ac impedance spectroscopy (IS) analysis and dc current-voltage (I-V) measurements. Fourth chapter reports the fluorescence resonance energy transfer mechanism for photo induced charge transfer from P3HT to solvothermally derived $CuInSe_2$. The HOMO and LUMO energy states of $CuInSe_2$ have also been determined from cyclic voltammetry and optical study. The next chapter includes the current rectification behavior of $CuInSe_2/TiO_2$ and $CuInSe_2$/HF-TiO_2 hetero-junctions, identical to the I-V characteristics of p-n junction diode and the impact of white light on it. Sixth chapter describes the synthesis procedure of Cadmium Oxide (CdO). Two different crystallite sizes based CdOs are derived from hydrothermal route at different temperatures. The morphological impact of derived CdO on charge conduction and relaxation is by using bias-dependent impedance spectroscopy (IS) has been investigated. An overview and conclusion of the entire work has been drawn in the end at the last chapter.

References

1. H. J. Snaith, *The journal of physical chemistry letters*, 2013, **4**, 3623-3630.
2. A. Kojima, K. Teshima, Y. Shirai and T. Miyasaka, *Journal of the american chemical society*, 2009, **131**, 6050-6051.
3. W. Xu, Q. Hu, S. Bai, C. Bao, Y. Miao, Z. Yuan, T. Borzda, A. J. Barker, E. Tyukalova and Z. Hu, *Nature Photonics*, 2019, **13**, 418-424.
4. S. Yakunin, M. Sytnyk, D. Kriegner, S. Shrestha, M. Richter, G. Matt, H. Azimi, C. Brabec, J. Stangl and M. Kovalenko, 2015.
5. H. Dong, C. Ran, W. Gao, N. Sun, X. Liu, Y. Xia, Y. Chen and W. Huang, *Advanced Energy Materials*, 2022, **12**, 2102213.
6. H. Dong, C. Ran, W. Gao, M. Li, Y. Xia and W. Huang, *ELight*, 2023, **3**, 3.
7. X. Zhao, Y. Du, W. Li, Z. Zhao and M. Lei, *Advanced Composites and Hybrid Materials*, 2023, **6**, 176.
8. M. Dada and P. Popoola, *Beni-Suef University Journal of Basic and Applied Sciences*, 2023, **12**, 1-15.
9. W. Honda, T. Arie, S. Akita and K. Takei, 2015 Transducers-2015 18th International Conference on Solid-State Sensors, Actuators and Microsystems (TRANSDUCERS), 2015.
10. H. Chen, Y. Cao, J. Zhang and C. Zhou, *Nature communications*, 2014, **5**, 4097.
11. S. Kumagai, H. Murakami, K. Tsuzuku, T. Makita, C. Mitsui, T. Okamoto, S. Watanabe and J. Takeya, *Organic Electronics*, 2017, **48**, 127-131.
12. L. F. Weber, *IEEE transactions on plasma science*, 2006, **34**, 268-278.
13. T. Wu, C.-W. Sher, Y. Lin, C.-F. Lee, S. Liang, Y. Lu, S.-W. Huang Chen, W. Guo, H.-C. Kuo and Z. Chen, *Applied sciences*, 2018, **8**, 1557.
14. X. Lv, K. H. Loo, Y.-M. Lai and K. T. Chi, *IEEE Transactions on Industrial Electronics*, 2013, **61**, 4665-4673.
15. F. Templier, *Journal of the Society for Information Display*, 2016, **24**, 669-675.
16. V. Wood and V. Bulović, *Nano reviews*, 2010, **1**, 5202.

17. V. Wood, M. Panzer, J. Long, M. Bradley, J. Halpert and M. Bawendi, *Adv Mater*, 2009, **21**, 2151-2155.
18. M. K. Choi, J. Yang, T. Hyeon and D.-H. Kim, *npj Flexible Electronics*, 2018, **2**, 10.
19. H. L. Tuller, *Materials for renewable and sustainable energy*, 2017, **6**, 1-16.
20. M. Grätzel, *Philosophical Transactions of the Royal Society A: Mathematical, Physical and Engineering Sciences*, 2007, **365**, 993-1005.
21. N. A. Ludin, N. I. Mustafa, M. M. Hanafiah, M. A. Ibrahim, M. A. M. Teridi, S. Sepeai, A. Zaharim and K. Sopian, *Renewable and Sustainable Energy Reviews*, 2018, **96**, 11-28.
22. K. Ranabhat, L. Patrikeev, A. A. e. Revina, K. Andrianov, V. Lapshinsky and E. Sofronova, *Journal of Applied Engineering Science*, 2016, **14**.
23. M. Tao, *The Electrochemical Society Interface*, 2008, **17**, 30.
24. M. P. Paranthaman, W. Wong-Ng and R. N. Bhattacharya, *Semiconductor materials for solar photovoltaic cells*, Springer, 2016.
25. S. Kohiki, M. Nishitani, T. Negami and T. Wada, *Applied physics letters*, 1993, **62**, 1656-1657.
26. G. S. Park, S. Lee, D. S. Kim, S. Y. Park, J. H. Koh, D. H. Won, P. Lee, Y. R. Do and B. K. Min, *Advanced Energy Materials*, 2023, **13**, 2203183.
27. W. Hörig, W. Möller, H. Neumann, E. Reccius and G. Kühn, *physica status solidi (b)*, 1979, **92**, K1-K4.
28. S.-H. Wei, S. Zhang and A. Zunger, *Applied physics letters*, 1998, **72**, 3199-3201.
29. B. Schumann, H. Neumann, A. Tempel, G. Kühn and E. Nowak, *Kristall und Technik*, 1980, **15**, 71-76.
30. A. M. Gabor, J. R. Tuttle, D. S. Albin, M. A. Contreras, R. Noufi and A. M. Hermann, *Applied physics letters*, 1994, **65**, 198-200.
31. X. Li, *Jom*, 2007, **59**, 71-74.
32. X. Li and P. Nardi, *Nanotechnology*, 2003, **15**, 211.
33. M. Faraday, *Philosophical transactions of the Royal Society of London*, 1857, 145-181.
34. B. Mubeen, A. Hasnain, J. Wang, H. Zheng, S. A. H. Naqvi, R. Prasad, A. u. Rehman, M. A. Sohail, M. Z. Hassan and M. Farhan, *Coatings*, 2023, **13**, 212.
35. S. C. Dipak and D. Srirama, Proceedings of the 50th Indian Geotech. Conference, Maharashtra, India, 2015.

36. Y. Yin and D. Talapin, *Chemical Society Reviews*, 2013, **42**, 2484-2487.
37. A. E. Shalan, A. S. H. Makhlouf and S. Lanceros-Méndez, *Advances in Nanocomposite Materials for Environmental and Energy Harvesting Applications*, 2022, 3-14.
38. A. Nabok, *Organic and Inorganic Nanostructures*, Artech House, Inc:, Norwood, 2005.
39. J. K. Patel, A. Patel and D. Bhatia, in *Emerging technologies for nanoparticle manufacturing*, Springer, 2021, pp. 3-23.
40. C. Rao and A. Cheetham, in *Nanomaterials handbook*, ed. Y. Gogotsi, FL: CRC Press/Taylor & Francis, Boca Raton, Yury Gogotsi edn., 2006, pp. 1-12.
41. C. Murphy, N. Jana, L. Gearheart, S. Obare, K. Caswell, S. Mann, C. Johnson, S. Davis, E. Dujardin and K. Edler, in *The Chemistry of Nanomaterials: Synthesis, Properties and Applications*, eds. C. N. R. Rao, A. Müller and A. K. Cheetham, Wiley, Weinheim, 2004, pp. 285-307.
42. S. Prasad, V. Kumar, S. Kirubanandam and A. Barhoum, in *Emerging applications of nanoparticles and architecture nanostructures*, Elsevier, 2018, pp. 305-340.
43. A. Barhoum, M. L. García-Betancourt, J. Jeevanandam, E. A. Hussien, S. A. Mekkawy, M. Mostafa, M. M. Omran, M. S. Abdalla and M. Bechelany, *Nanomaterials*, 2022, **12**, 177.
44. D. B. Resnik, *AMA Journal of Ethics*, 2019, **21**, 363-369.
45. C. Lv, X. Zhang, Y. Liu, T. Zhang, H. Chen, J. Zang, B. Zheng and G. Zhao, *Chemical Society Reviews*, 2021, **50**, 3957-3989.
46. G. Paramasivam, V. V. Palem, T. Sundaram, V. Sundaram, S. C. Kishore and S. Bellucci, *Nanomaterials*, 2021, **11**, 3228.
47. D. Roy, A. K. Srivastava, K. Mukhopadhyay and E. P. Namburi, in *Novel Defence Functional and Engineering Materials (NDFEM) Volume 1: Functional Materials for Defence Applications*, Springer, 2024, pp. 73-91.
48. C. Rao and A. Cheetham, *Journal of Materials Chemistry*, 2001, **11**, 2887-2894.
49. V. Pokropivny, R. Lohmus, I. Hussainova, A. Pokropivny and S. Vlassov, *Introduction to nanomaterials and nanotechnology*, Tartu University Press, Tartu, 2007.
50. N. Domun, H. Hadavinia, T. Zhang, T. Sainsbury, G. Liaghat and S. Vahid, *Nanoscale*, 2015, **7**, 10294-10329.
51. J. Parameswaranpillai, G. Joseph, K. Shinu, S. Jose, N. V. Salim and N. Hameed, *RSC Advances*, 2015, **5**, 25634-25641.

52. L. Liu, M. Yu, J. Zhang, B. Wang, W. Liu and Y. Tang, *Journal of Materials Chemistry C*, 2015, **3**, 2326-2333.
53. E. Glogowski, R. Tangirala, T. P. Russell and T. Emrick, *Journal of Polymer Science Part A: Polymer Chemistry*, 2006, **44**, 5076-5086.
54. W. R. Glomm, *Journal of Dispersion Science and Technology*, 2005, **26**, 389-414.
55. Z. Liu, J. Xu, D. Chen and G. Shen, *Chemical Society Reviews*, 2015, **44**, 161-192.
56. W. Yang, P. Wan, H. Meng, J. Hu and L. Feng, *CrystEngComm*, 2015, **17**, 2989-2995.
57. V. Chabot, D. Higgins, A. Yu, X. Xiao, Z. Chen and J. Zhang, *Energy & Environmental Science*, 2014, **7**, 1564-1596.
58. R. Bogue, *Assembly Automation*, 2011, **31**, 106-112.
59. S. Gupta, A. Joshi and M. Kaur, *Journal of Chemical Sciences*, 2010, **122**, 57-62.
60. C. Chinnamuthu and P. M. Boopathi, *Madras Agricultural Journal*, 2009, **96**, 17-31.
61. A. Blum, N. Mokrovski and A. Regel, in *Seventh All-Union Conference on the Properties of Semiconductors (1950)*, Izv. Akad. Nauk SSSR Ser. Fiz, Kiev, USSR, 1952, vol. 16, p. 139.
62. N.A. Goryunova and A. P. Obukhov, in *Seventh All-Union Conference on the Properties of Semiconductors*, Kiev, 1950.
63. H. Welker, *Zeitschrift für Naturforschung A*, 1952, **7**, 744-749.
64. R. Breckenridge, W. Hosier and W. Oshinsky, *Phys. Rev.*, 1953, **91**, 243.
65. A. Ioffe, *Izv. Akad. Nauk. SSSR Ser. Fiz*, 1951, **15**, 477.
66. H. J. Welker, *IEEE Transactions on Electron Devices*, 1976, **23**, 664-674.
67. H. Welker, *Physica*, 1954, **20**, 893-909.
68. C. Goodman and R. Douglas, *Physica*, 1954, **20**, 1107-1109.
69. H. Hahn, G. Frank, W. Klingler, A. Meyer and G. Storger, *Anorg. Allg. Chem*, 1953, **271**, 153-170.
70. I. G. Austin, C. H. L. Goodman and A. E. Pengelly, *Journal of The Electrochemical Society*, 1956, **103**, 609.
71. J. L. Shay and H. Jack, *Ternary Chalcopyrite Semiconductors: Growth, Electronic Properties, and Applications, International Series on Science of the Solid State*, Pergamon Press, New York, 1975.

72. G. Fourcaudot, M. Gourmala and J. Mercier, *Journal of Crystal Growth*, 1979, **46**, 132-135.
73. A. Biswas, S. Sil, A. Dey, J. Datta, D. Das and P. P. Ray, *Journal of Physics and Chemistry of Solids*, 2021, **150**, 109878.
74. R. Noufi and K. Zweibel, *2006 IEEE 4th World Conference on Photovoltaic Energy Conference*, 2006, **1**, 317-320.
75. M. A. Contreras, B. Egaas, K. Ramanathan, J. Hiltner, A. Swartzlander, F. Hasoon and R. Noufi, *Progress in Photovoltaics: Research and applications*, 1999, **7**, 311-316.
76. T. J. Coutts, L. L. Kazmerski and S. Wagner, *Copper indium diselenide for photovoltaic applications*, Solar Energy Research Inst., Golden, Co., 1986.
77. H. Neumann and R. Tomlinson, *Solar cells*, 1990, **28**, 301-313.
78. J. F. Guillemoles, U. Rau, L. Kronik, H. W. Schock and D. Cahen, *Advanced Materials*, 1999, **11**, 957-961.
79. B. Dimmler and H. W. Schock, *Progress in Photovoltaics: Research and Applications*, 1996, **4**, 425-433.
80. H. S. Ullal, K. Zwelbel and B. Von Roedern, *Conference Record of the Twenty Sixth IEEE Photovoltaic Specialists Conference-1997*, 1997, 301-305.
81. P. Jackson, D. Hariskos, E. Lotter, S. Paetel, R. Wuerz, R. Menner, W. Wischmann and M. Powalla, *Progress in photovoltaics: research and applications*, 2011, **19**, 894-897.
82. T. K. Todorov, O. Gunawan, T. Gokmen and D. B. Mitzi, *Progress in Photovoltaics: Research and Applications*, 2013, **21**, 82-87.
83. J. Ramanujam and U. P. Singh, *Energy & Environmental Science*, 2017, **10**, 1306-1319.
84. Q. Han, Y.-T. Hsieh, L. Meng, J.-L. Wu, P. Sun, E.-P. Yao, S.-Y. Chang, S.-H. Bae, T. Kato and V. Bermudez, *Science*, 2018, **361**, 904-908.
85. M. Kumar, A. Seth, A. K. Singh, M. S. Rajput and M. Sikandar, *Environmental and Sustainability Indicators*, 2021, **12**, 100155.
86. M. Green, E. Dunlop, J. Hohl-Ebinger, M. Yoshita, N. Kopidakis and X. Hao, *Progress in photovoltaics: research and applications*, 2021, **29**, 3-15.
87. A. C. Berends, M. J. Mangnus, C. Xia, F. T. Rabouw and C. de Mello Donega, *The journal of physical chemistry letters*, 2019, **10**, 1600-1616.

88. J. Xu, O. Voznyy, M. Liu, A. R. Kirmani, G. Walters, R. Munir, M. Abdelsamie, A. H. Proppe, A. Sarkar and F. P. García de Arquer, *Nature nanotechnology*, 2018, **13**, 456-462.
89. J. Kolny-Olesiak and H. Weller, *ACS applied materials & interfaces*, 2013, **5**, 12221-12237.
90. O. Yarema, M. Yarema and V. Wood, *Chemistry of Materials*, 2018, **30**, 1446-1461.
91. S. Wagner, J. Shay, P. Migliorato and H. Kasper, *Applied Physics Letters*, 1974, **25**, 434-435.
92. P. Migliorato, J. Shay, H. Kasper and S. Wagner, *Journal of Applied Physics*, 1975, **46**, 1777-1782.
93. J. Parkes, R. Tomlinson and M. Hampshire, *Journal of Applied Crystallography*, 1973, **6**, 414-416.
94. S. Wagner and P. Bridenbaugh, *Journal of Crystal Growth*, 1977, **39**, 151-159.
95. J. Parkes, R. Tomlinson and M. Hampshire, *Journal of Crystal Growth*, 1973, **20**, 315-318.
96. P. W. Yu, Y. Park and J. Grant, *Applied Physics Letters*, 1976, **28**, 214-216.
97. P. W. Yu, Y. Park, S. Faile and J. Ehret, *Applied Physics Letters*, 1975, **26**, 717-719.
98. S. Fouad and S. Youssef, *Acta Physica Polonica A*, 1992, **82**, 495-501.
99. H. Soliman, M. El-Nahas, O. Jamjoum and K. A. Mady, *Journal of materials science*, 1988, **23**, 4071-4075.
100. H. Neumann, *Solar Cells*, 1986, **16**, 317-333.
101. J. Müller, J. Nowoczin and H. Schmitt, *Thin Solid Films*, 2006, **496**, 364-370.
102. S. Prabahar, V. Balasubramanin, N. Suryanarayanan and N. Muthukumarasamy, *Chalcogenide letters*, 2010, **7**, 49-58.
103. J. Ermer, R. Gay, D. Pier and D. Tarrant, *Journal of Vacuum Science & Technology A: Vacuum, Surfaces, and Films*, 1993, **11**, 1888-1895.
104. T. Amrillah, *Solar Energy*, 2023, **263**, 111982.
105. V. R. Voggu, J. Sham, S. Pfeffer, J. Pate, L. Fillip, T. B. Harvey, R. M. Brown Jr and B. A. Korgel, *ACS Energy Letters*, 2017, **2**, 574-581.
106. J. Ermer, C. Fredric, J. Hummel, C. Jensen, D. Pier, D. Tarrant and K. Mitchell, IEEE Conference on Photovoltaic Specialists, 1990.

107. M. L. Fearheiley, *Solar Cells*, 1986, **16**, 91-100.
108. U.-C. Boehnke and G. Kühn, *Journal of materials science*, 1987, **22**, 1635-1641.
109. T. Ciszek, *Journal of Crystal Growth*, 1986, **75**, 61-66.
110. B. Stanbery, S. Kincal, S. Kim, C. Chang, S. Ahrenkiel, G. Lippold, H. Neumann, T. Anderson and O. Crisalle, *Journal of applied physics*, 2002, **91**, 3598-3604.
111. K. Bachmann, M. Fearheiley, Y. Shing and N. Tran, *Applied physics letters*, 1984, **44**, 407-409.
112. K. Becker and S. Wagner, *Physical Review B*, 1983, **27**, 5240.
113. I. Shih, C. Champness and A. V. Shahidi, *Solar cells*, 1986, **16**, 27-41.
114. C. Stephan, D. Greiner, S. Schorr and C. A. Kaufmann, *Journal of Physics and Chemistry of Solids*, 2016, **98**, 309-315.
115. S. Kohiki, M. Nishitani, K. Nishikura, T. Negami, M. Terauchi and T. Hirao, *Thin Solid Films*, 1992, **207**, 265-269.
116. S. Siebentritt, M. Igalson, C. Persson and S. Lany, *Progress in Photovoltaics: Research and Applications*, 2010, **18**, 390-410.
117. Z.D. Kovalyuk, O.M. Sydor and a. V. V. Netyaga, *Semiconductor Physics, Quantum Electronics & Optoelectronics*, 2004, **7(4)**, 360-362.
118. K. Timmo, M. Altosaar, J. Raudoja, E. Mellikov, T. Varema, M. Danilson and M. Grossberg, *Thin solid films*, 2007, **515**, 5887-5890.
119. M. Benabdeslem, N. Benslim, L. Bechiri, L. Mahdjoubi, E. Hannech and G. Nouet, *Journal of crystal growth*, 2005, **274**, 144-148.
120. T. Dullweber, G. Hanna, W. Shams-Kolahi, A. Schwartzlander, M. Contreras, R. Noufi and H. Schock, *Thin Solid Films*, 2000, **361**, 478-481.
121. S. Agilan, D. Mangalaraj, S. K. Narayandass, G. M. Rao and S. Velumani, *Vacuum*, 2010, **84**, 1220-1225.
122. F. Luckert, M. Yakushev, C. Faugeras, A. Karotki, A. Mudryi and R. Martin, *Journal of Applied Physics*, 2012, **111**.
123. J. J. Loferski, *Journal of Applied Physics*, 1956, **27**, 777-784.
124. A. Bouich, S. Ullah, H. Ullah, B. Mari, M. E. Touhami, B. Hartiti and D. M. Santos, 2018 6th International Renewable and Sustainable Energy Conference (IRSEC), 2018.

125. I. Svitsiankou, V. Pavlovskii, E. Lutsenko, G. Yablonskii, A. Mudryi, O. Borodavchenko, V. Zhivulko, R. Martin and M. Yakushev, *Applied Physics Letters*, 2021, **119**.
126. M. Tanda, S. Manaka, J. R. E. Marin, K. Kushiya, H. Sano, A. Yamada and M. K. Takahashi, *Japanese journal of applied physics*, 1992, **31**, L753.
127. S. Ahmadi, N. Asim, M. Alghoul, F. Hammadi, K. Saeedfar, N. Ludin, S. H. Zaidi and K. Sopian, *International Journal of Photoenergy*, 2014, **2014**, 198734.
128. A. Zouaoui, M. Lachab, M. Hidalgo, A. Chaffa, C. Llinares and N. Kesri, *Thin Solid Films*, 1999, **339**, 10-18.
129. M. Artaud, F. Ouchen, L. Martin and S. Duchemin, *Thin Solid Films*, 1998, **324**, 115-123.
130. P. A. Jones, A. D. Jackson, P. D. Lickiss, R. D. Pilkington and R. D. Tomlinson, *Thin Solid Films*, 1994, **238**, 4-7.
131. A. Y. Cho, *Journal of Vacuum Science and Technology*, 1971, **8**, S31-S38.
132. S. Grindle, A. Clark, S. Rezaie-Serej, E. Falconer, J. McNeily and L. Kazmerski, *Journal of Applied Physics*, 1980, **51**, 5464-5469.
133. T. Negami, M. Nishitani, M. Ikeda and T. Wada, *Solar energy materials and solar cells*, 1994, **35**, 215-222.
134. K. S. Ramaiah, V. S. Raja, A. K. Bhatnagar, F. S. Juang, S. J. Chang and Y. K. Su, *Materials Letters*, 2000, **45**, 251-261.
135. P. V. Pillai and K. Vijayakumar, *Solar energy materials and solar cells*, 1998, **51**, 47-54.
136. K. Ohkawa and T. Mitsuyu, *Journal of Applied Physics*, 1991, **70**, 439-442.
137. D. Eason, Z. Yu, W. Hughes, W. Roland, C. Boney, Cook, Jr., J. Schetzina, G. Cantwell and W. Harsch, *Applied Physics Letters*, 1995, **66**, 115-117.
138. G. Mandel and F. Morehead, *Physical Review*, 1964, **136**, A300.
139. M. Grundmann, *physica status solidi (a)*, 2015, **212**, 1409-1426.
140. K. Baedeker, *Über die elektrische Leitfähigkeit und die thermoelektrische Kraft einiger Schwermetallverbindungen*, JA Barth, 1906.
141. D. Jayathilake and T. N. Peiris, *SF Journal of Material and Chemical Engineering*, 2018, **1**, 1004.
142. S. Senthil, S. Srinivasan, T. Thangeeswari, B. Madhu and M. Silambarasan, *Nano-Structures & Nano-Objects*, 2020, **24**, 100554.

143. R. Mane, H. Pathan, C. Lokhande and S.-H. Han, *Solar Energy*, 2006, **80**, 185-190.
144. B. A. Gozeh, A. Karabulut, C. B. Ismael, S. I. Saleh and F. Yakuphanoglu, *Journal of Alloys and Compounds*, 2021, **872**, 159624.
145. W.-M. Cho, G.-R. He, T.-H. Su and Y.-J. Lin, *Applied Surface Science*, 2012, **258**, 4632-4635.
146. R. Bulakhe and C. Lokhande, *Sensors and Actuators B: Chemical*, 2014, **200**, 245-250.
147. D. Dhawale, A. More, S. Latthe, K. Rajpure and C. Lokhande, *Applied Surface Science*, 2008, **254**, 3269-3273.
148. T. Singh, D. Pandya and R. Singh, *Materials chemistry and physics*, 2011, **130**, 1366-1371.
149. R. Ferro and J. Rodrıguez, *Thin solid films*, 1999, **347**, 295-298.
150. K. Kaviyarasu, E. Manikandan, J. Kennedy and M. Jayachandran, *Materials Letters*, 2014, **120**, 243-245.
151. J. Godt, F. Scheidig, C. Grosse-Siestrup, V. Esche, P. Brandenburg, A. Reich and D. A. Groneberg, *Journal of occupational medicine and toxicology*, 2006, **1**, 1-6.

Chapter 2

Theoretical analysis of different material characterizations

The fundamental theories and related parameters associated with the material characterization, as well as the theory pertaining to the metal-semiconductor contact have been explored in this chapter. The way of analysis and understanding of the mechanism of charge transport within the Schottky device is illustrated in this part.

2.1. Crystallite size and strain from Powder X-Ray Diffraction (PXRD)

Powder X-Ray diffraction analysis (PXRD) is a nondestructive laboratory technique that provides detailed information about the crystallographic structure, chemical composition, and physical properties of a chemical compound. It is based on the constructive interference of monochromatic X-rays of CuK_α radiation having wavelength 1.54Å. The Fourier analysis of diffraction spectra obtained from the powder crystal sample, informs about all the details of crystal (e.g. lattice dimension; crystallite size; and crystal-strain). Few analytical methods for the purposes are illustrated aptly as follows:

2.1.1. Debye-Scherrer and Williamson-Hall Method

The Scherrer equation, sometimes referred to as the Debye-Scherrer equation, has been a helpful and pronounced tool for estimating crystallite size. The width of the diffraction peak pattern could enable to get information about the average dimension of material using Debye-Scherrer equation, developed from the famous Bragg's Diffraction law. The equation that help to estimate crystal dimension, can be stated as

$$\beta_s = \frac{K\lambda}{D\cos\theta_{hkl}} \qquad (2.1)$$

Here, β_s is the full-width half maxima (FWHM) or the integral breadth of the peak (hkl plane) due to the crystallite size contribution (**Fig. 2.1**), K is considered as near about 1, D is the average thickness of the crystal which is normal to the hkl plane. θ is Bragg's angle and λ is the wavelength of CuK_α radiation. It is crucial to remember that the Scherrer equation interprets the size of the crystallite, not the aggregation of polycrystalline crystals.[1]

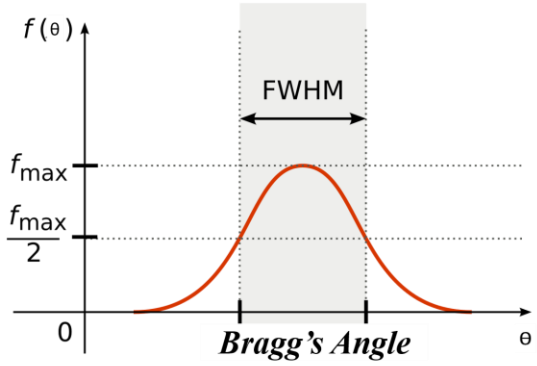

Fig. 2.1: Full-width half maxima (FWHM) or the integral breadth of the peak

Crystallite, in general, denotes the discrete diffracting zone that coherently scatters the applied X-ray.

However, the lattice distortion also plays a role in the broadening of the diffraction peak in addition to the size of the crystallite. Compressive and tensile stresses as well as compositional gradient within the sample could be the source of this distortion.[1] The bending or shearing in the crystals can be used to illustrate the coexistence of stress and strain gradients in the crystal. Peak broadening can also occasionally be attributed to variations in unit cell dimensions with negligible compositional differences in different crystals. If we consider the differential Bragg equation with respect to the d-spacing and the diffraction angle, then

$$\left|\frac{\Delta d}{d}\right| = \cot\theta\Delta\theta \Rightarrow \Delta(2\theta) = 2\left|\frac{\Delta d}{d}\right|\tan\theta \qquad (2.2)$$

Around the Bragg maximum, the fractional spread in the d spacing is considered to be 2η, and then the stress-induced broadening due to the strain (η) is expressed by[1]

$$\beta_\eta = 4\eta\tan\theta \qquad (2.3)$$

Hence, the broadening on the peak is convoluted by the effects of crystallite size and stress. Thus the total broadening can be written as,

$$\beta = \frac{K\lambda}{d\cos\theta} + 4\eta\tan\theta \qquad (2.4)$$

Or,

$$\beta\cos\theta = \frac{K\lambda}{D} + 4\varepsilon\sin\theta \qquad (2.5)$$

the plot of βcosθ versus sinθ which is also referred as Williamson-Hall plot,[2] For a particular hkl planes, yields the values of crystallite size and strain deduced from the intercept and slope (**Fig. 2.2**), respectively. The effect of low angle reflections has decreased due to the dependency of stress broadening on tanθ. W-H plots are usually applied to smaller unit cell materials.

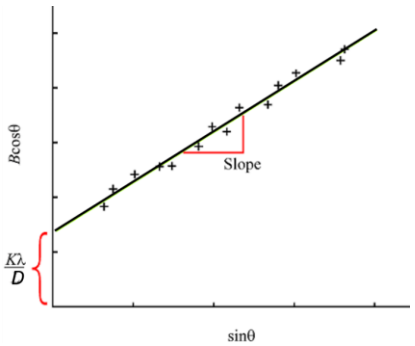

Fig. 2.2: Williamson-Hall plot

2.2. Determination of optical parameters from UV-Vis data: A theoretical study

The absorption coefficient, the optical energy band gap, the refractive index and the optical conductivity of the materials can be derived from the UV-Vis spectroscopy data, which could enable one to get better information about the optical characteristics of the materials.

2.2.1. Absorption coefficient; Optical Band gap and Optical conductivity

Beer Lambert's law states that the light's intensity drops exponentially with the depth in the material i.e., $I = I_0 e^{-\alpha d}$, where I is the intensity of light after passing through the sample, I_0 is the initial light intensity, α is the linear absorption coefficient, and d is the path travelled by the light. Generally, I/I_0 is defined as transmittance. So, absorbance A can be stated as

$$A = \log\left(\frac{I_0}{I}\right) = \log\left(\frac{I_0}{I_0 e^{-\alpha d}}\right) = \log e^{\alpha d} = \frac{\alpha d}{2.303} \qquad (2.6)$$

$$\Rightarrow \alpha = \frac{2.303A}{d}$$

Tauc's developed an equation to determine the optical band gap energy in the late 70's of the nineteenth century, which can be expressed as,[3]

$$\alpha h\nu = c\left(h\nu - E_g\right)^{\gamma} \qquad (2.7)$$

Here *c* is a constant related to valence band and conduction band,[4] *h* is the Planck's constant, ν is the frequency of light and E_g is the band gap energy, γ is associated to the electronic transition nature. The values of band gap E_g can be estimated from the extrapolation of the linear region of the $(\alpha h\nu)^{1/\gamma}$ versus $h\nu$ graph to the photon energy axis. The value of γ can be ½, 2, 3/2, 3 for the direct allowed, indirect allowed, direct forbidden and indirect forbidden transition, respectively, and can be obtained from the differential expression:

$$\frac{d[\ln(\alpha h\nu)]}{d[h\nu]} = \frac{\gamma}{h\nu - E_g} \qquad (2.8)$$

There is a discontinuity that corresponds to the band gap energy in the plot of $d[\ln(\alpha h\nu)]/d[h\nu]$ versus $h\nu$. This energy value is used in the plot of $\ln[(\alpha h\nu)]$ versus $\ln[h\nu - E_g]$, and the slope of the plot gives the value of γ.

The refractive index can also be estimated by using the absorbance data. It is well known that A+T+R=1, where, A, T, R are normalized absorbance, transmittance, and reflectance, respectively. According to Kramers-Kronig analysis, a material's optical reflectance is determined by the real and imaginary components of its dielectric constant and index of refraction. So,

$$R = \frac{\left|E^r\right|^2}{\left|E^i\right|^2} = \frac{\left|1-n^*\right|^2}{\left|1+n^*\right|^2} = \frac{\left|1-n-ik\right|^2}{\left|1+n+ik\right|^2} = \frac{\left(1-n\right)^2+k^2}{\left(1+n\right)^2+k^2} \tag{2.9}$$

Here 'R' is reflectivity at normal incidence, 'E^r' is the reflected light, 'E^i' is the incident light, n^*(=n+ik) is refractive index. 'n' and 'k' are the real and imaginary parts of the refractive index. By rearranging the equation (2.9), the refractive index can be estimated as,[5]

$$n = \frac{1+R}{1-R} + \sqrt{\frac{4R}{(1-R)^2} - k^2} \tag{2.10}$$

When light propagatesa distance d, the radiation wave can be expressed as

$$E = E_0 e^{[i2\pi\nu\{t+(d/v)\}]} \tag{2.11}$$

putting the value of wave velocity $v=c/n^*$, then,

$$E = E_0 e^{i2\pi\nu t}.e^{i2\pi nd/c}.e^{-2\pi kd/c} \tag{2.12}$$

we have the extinction coefficient

$$\frac{I}{I_0} \approx \frac{E^2}{E_0^2} = e^{-4\pi\nu kd/c} = e^{-\alpha d}$$

$$\Rightarrow \alpha = \frac{4\pi\nu k}{c} \tag{2.13}$$

$$\Rightarrow k = \frac{\alpha\lambda}{4\pi}$$

Furthermore, the velocity of light follows

$$\frac{1}{v^2} = \frac{n^2-k^2}{c} - i\frac{2nk}{c} \tag{2.14}$$

So, when a radiation obeys the Maxwell equation, then it can be obtained from the equation,[6]

$$\frac{1}{v^2} = \frac{\varepsilon}{c} - i\frac{2\sigma}{\nu c^2} \qquad (2.15)$$

Whereσ is the optical conductivity. By equation (2.14) and (2.15), it can be obtained as,

$$\frac{\sigma}{\nu} = nk$$

$$\Rightarrow \sigma = \nu nk \qquad (2.16)$$

$$\Rightarrow \sigma = \frac{\nu n \alpha \lambda}{4\pi} = \frac{\alpha nc}{4\pi}$$

2.3. Impedance Spectroscopy (IS)

In subject to study the electrical properties of the nanomaterials the term impedance has a significant value. Oliver Heaviside coined the word impedance in 1880. A. E. Kennelly later expanded it in terms of vector diagrams.[7] Impedance spectroscopy is a potent and very impactful technique for describing the electrical characteristics of materials and material-electrode interfaces. Investigating the dynamics of mobile or bound charges in the bulk or interface of different types of materials, such as semiconductors, insulators, and ionic materials, is made possible by this very helpful tool.

2.3.1. Basic functions

There are various fundamental functions exist in the impedance spectroscopy which plays an important role to apprehend the impedance (Z) behavior, admittance (Y), modulus function (M), dielectric permittivity (ε) of the materials. Impedance is expressed as the vector quantity, $Z(\omega)=Z'-jZ''$, where, $Z'(=|Z|\cos\theta)$ is the real part of the total impedance, $Z''(=|Z|\sin\theta)$ is the imaginary part, and θ $[=\tan^{-1}(Z''/Z')]$ is the phase angle. More-often, reactance ($X_C=1/\omega C$), susceptance ($B=\omega C$), conductance (G), resistance(R)

Table 2.1 Relation between the basic impedance function

	Z(=Z′-jZ″)	**Y(=Y′+jY″)**	**M(=M′+jM″)**	**ε (=ε′-jε″)**
Z(=Z′-jZ″)	Z	Y^{-1}	$M/j\omega C_0$	$(j\omega C_0\varepsilon)^{-1}$
Y(=Y′+jY″)	Z^{-1}	Y	$j\omega C_0/M$	$j\omega C_0\varepsilon$
M(=M′+jM″)	$j\omega C_0 Z$	$j\omega C_0\, Y^{-1}$	M	ε^{-1}
ε (=ε′-jε″)	$(j\omega C_0 Z)^{-1}$	$Y/j\omega C_0$	M^{-1}	ε

functions are also sometimes used to express those basic functions. The important relations between the basic functions are tabulated **in table 2.1**[7] for references.

2.3.2. Nyquist and Bode plot: Conduction of Carriers

The Nyquist diagram, sheds light on the conduction mechanism of the materials and the material-electrode interface, is the plot between the real and imaginary parts of the impedance. In an ideal scenario, the Nyquist plot shows one or more perfect or depressed semicircles, which provide insight into the quantity and kind of relaxations occurring within the conduction mechanism. Occasionally, the instrument's limitations prevent the semicircles from being completed. The materials and experiment type affect the frequency range. In Nyquist plot, the frequency increases from right to left of Z′ axis. In Impedance Spectroscopy, the Bode plot is yet another crucial presentation. For the applied frequency (logarithm), it shows the fluctuation in phase angle and the logarithm of the impedance magnitude. The information about the change in impedance nature from low frequency to high frequency can be found in the Bode plot. Additionally, it offers a fundamental understanding of the time constant and corresponding resonance frequency for any material electrode system or device.

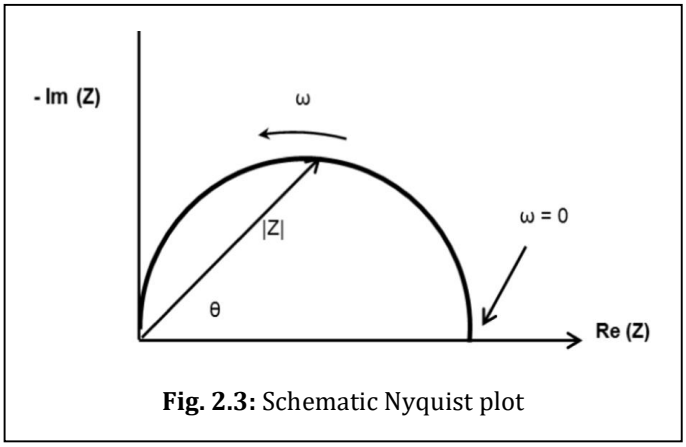

Fig. 2.3: Schematic Nyquist plot

2.3.3. Equivalent circuit modeling

Typically, the Nyquist plot data is examined through fitting using the relevant equivalent circuit. The conduction phenomenon's likely explanation is investigated by comparing the equivalent circuit to the best fit of experimentally obtained impedance data.

In this context, selecting the suitable equivalent circuit is crucial and ought to be done so by taking chemical and physical characteristics of the system into consideration. Generally, resistors, capacitors, and inductors are the most often used circuit components. However, in order to more properly illustrate the impedance response, other distributed circuit elements such constant phase element and Warburg diffusion impedance are occasionally employed.

Table 2.2 Component used in equivalent circuit model

Component	Equivalent Element	Impedance
Resistor	R[ohm]	R
Capacitor	C[F]	$1/j\omega C$
Inductor	L[H]	$j\omega L$
Infinite diffusion	Z_w[ohm]	$R_w/\sqrt{(j\omega)}$
Finite diffusion	Z_o[ohm]	$\frac{R_0 \tanh\left(\sqrt{j\omega L_0^2 / D}\right)}{\sqrt{j\omega L_0^2 / D}}$
Constant phase element(CPE)	Q[$ohm^{-1}s^{\alpha}$]	$1/Q(j\omega)^{\alpha}$

The most used components and their corresponding impedance are enlisted in **table 2.2.**[8]

2.4. Schottky diode: A theoretical view

Braun first reported asymmetric conduction between metal and semiconductor (lead sulfide) in 1874,[9] but Schottky et al. (1931)[10] were the first to realize the formation of a potential barrier between the metal-semiconductor contacts. The metal-semiconductor (MS) diode, also called the Schottky diode, has become increasingly popular over the years due to its extensive use in photovoltaic and sensor devices. In 1938, Schottky and Mott proposed a model to measure the shape of the barrier and the barrier height.[11, 12] Here, a quick overview of the Schottky formation and the underlying charge transport mechanism has been given.

2.4.1. Barrier in Schottky diode

A Schottky barrier is mainly a Metal-Semiconductor (M-S) junction that can produce rectifying current voltage at bias. The formation of barrier potential within the junction and the underlying charge transport mechanism through this junction can be understood by Schottky –Mott theory.

2.4.1.1. Schottky –Mott theory

According to Schottky and Mott, the rectifying nature of the MS contact results in the formation of an electrostatic barrier between metal and semiconductor, which is caused by the difference in work functions of the metal and semiconductor. The depletion region in the semiconductor is assumed to be entirely void of conduction electrons. As a result, space charge forms in this region due to the presence of uncompensated donor ions. When the space charge is evenly distributed throughout the depletion region, the electric field strength increases linearly with the distance from the edge of the depletion region towards the metal.As a result, the electrostatic potential increases quadratically, forming a parabolic potential barrier known as a Schottky barrier.

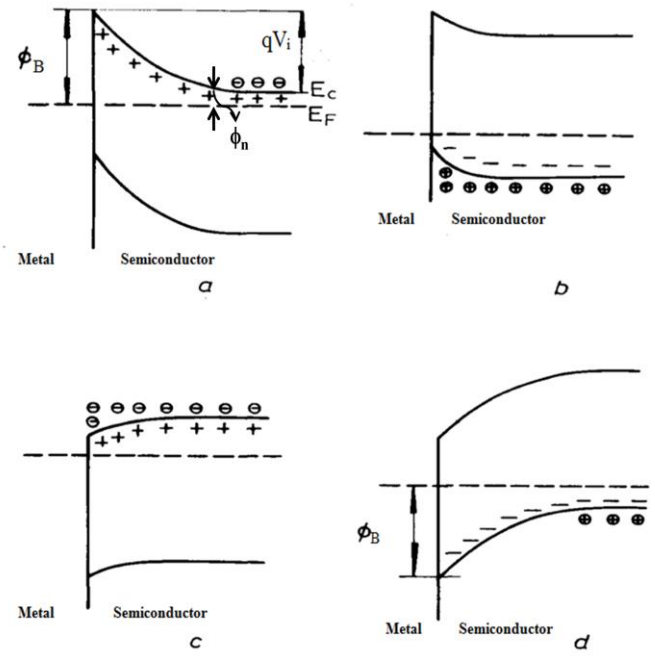

Fig.: 2.4: Schottky barrier formation in between the metal and different type of semiconductor. (a) $\phi_m > \phi_s$ (n-type), (b) $\phi_m > \phi_s$

The amount of band bending, shown as V_d (diffusion potential), is determined by the difference between the metal's (ϕ_m) and semiconductor's (ϕ_s) work functions=ϕ_m- ϕ_s. When ϕ_m for an n-type semiconductor is larger than ϕ_s, electrons from semiconductors enter metal to balance the Fermi level and create a depletion zone in the semiconductor, which leads to an upward band bending (**Fig. 2.4** (a)).[13]

Nevertheless, in p-type semiconductors, the circumstance where $\phi_m > \phi_s$ does not produce obstacles to the hole motion, resulting in the formation of an ohmic contact (**Fig. 2.4**(b)).[13] When the work function of the metal is smaller than that of the semiconductor, the n-type semiconductor also forms an ohmic contact ($\phi_m < \phi_s$) (**Fig. 2.4**(c)).[13] But, in that case ($\phi_m < \phi_s$), holes in a p-type semiconductor encounter a barrier, resulting in a rectifying

behavior at the metal-p-type semiconductor contact. (**Fig. 2.4**(d).[13] According to the Schottky–Mott approximation, the barrier height at the metal-semiconductor (MS) junction is conventionally expressed as,

$\phi_B=qV_i+E_c-E_F=\phi_m-\chi_s$ (2.17)

Where, χ_s (=ϕ_s- (E_c-E_F)) also referred to as the semiconductor's electron affinity, is the energy differential between the vacuum level and the bottom of the conduction band.

2.4.1.2. Modified Schottky–Mott theory

The contribution of the surface dipole to the metallic work function and the semiconductor's electron affinity during the creation of the MS contact was disregarded by Schottky-Mott theory. However, in the actual scenario, the surface dipole layers form at the surface and are active. The electron clouds of surface atoms get distorted as a result. The center corresponding to the positive and negative charge distributions does not overlap as a consequence. Bardeen[14] clarified the conundrum around surface dipoles in 1947 and emphasized the importance of the localized surface state in the barrier development as well as the nonlinear dependency of ϕ_B on ϕ_m. In actuality, the surface states function on the semiconductor surface as unfulfilled bonds. The unpaired electron in the confined orbital is associated with the atoms' one-sided neighbor at the surface. This orbital is pointed away from the surface and is referred to as a dangling bond.[13] Distributed throughout the prohibited gap energy, the surface states are occupied up to the neutral level. This neutral level does not correspond to by the Fermi level, resulting in a limited number of net charges in the surface states. In addition, between the MS contact, an oxide layer is formed, and the surface states charge and image charge on the metal surface aid in the creation of a dipole layer. In 1965, Cowly and Sze have revised the equation (2.17) which is given by,[15]

$$\phi_B = \xi(\phi_m - \phi_s) + (1-\xi)\left(E_g - \phi_0\right) \quad (2.18)$$

where, $\xi = \frac{\varepsilon_i}{\varepsilon_i + q\delta D_s}$, E_g is the band gap of the semiconductor, ϕ_0 is the neutral level energy, ε_I is the total permittivity, q is the charge, D_s is the density per electron-volt per area, δ is the thickness of the interfacial oxide layer.

2.4.2. Charge transport analysis via current-voltage characteristics

The carrier transfers from the semiconductor to the metal, or vice versa, happens via four distinct pathways. These include (a) thermionic emission over the barrier, (b) quantum mechanical tunneling through the barrier, (c) carrier recombination in the depletion region, and (d) recombination in the neutral region or hole injection.[13] The various charge transport mechanisms for n-type semiconductors are shown in **Fig. 2.5**.[16]

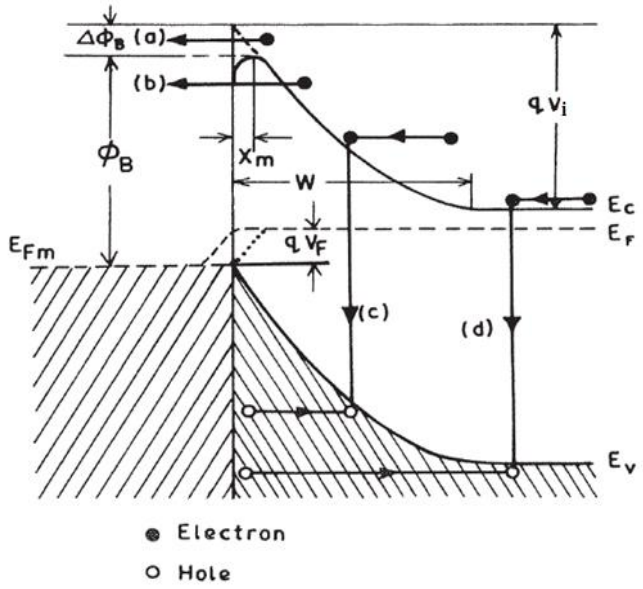

Fig.: 2.5: Energy band diagram for a Schottky diode under forward bias illustrating different transport process. (a) thermionic emission, (b) tunneling through the barrier, (c) carrier recombination in the depletion region, and (d) minority carrier injection.

2.4.2.1. Thermionic emission over the barrier

Previous studies by Wagner[17] (1931) and Schottky et al.[18] (1939) assumed that the current followed the drift and diffusion mechanisms. Their theory states that the diode current follows the equation as follows

$$I = qAN_c\mu E_m \exp\left(\frac{-\phi_B}{kT}\right)\left[\exp\left(\frac{qV}{kT}\right)-1\right] \qquad (2.19)$$

Where, A is the effective diode area, N_c is the effective density of states in the conduction band of the semiconductor, μ is the electron mobility, E_m is the maximum electric field. However, Bethe et al.[19] demonstrated that the diode current does not accurately follow equation (2.19) and established the presence of the thermionic emission effect. As per the previous assumption, during the forward bias, the electrons are in equilibrium with the lattice, and at the interface, the quasi-Fermi level equalizes the metal Fermi level. On the other hand, according to the thermionic emission hypothesis, the quasi-Fermi level is horizontal through the depletion zone and electrons are entering the metal with a greater

energy. In accordance with Bethe's proposal, the thermionic emission controls the diode current, drift and diffusion effect are therefore disregarded. His proposal also takes into account the fact that the barrier height is less than the value of kT but that electrons require a higher kinetic energy to cross the potential barrier. In that case, the electrons follow the Maxwell distribution of velocities, and the number of successfully emitted electrons can be written as,[16]

$$n^{*} = n_0 \exp\left[\frac{-q(V_i - V)}{kT}\right] \tag{2.20}$$

$$\text{Where, } n_0 = N_C \exp\left[\frac{-\phi_n}{kT}\right] \tag{2.21}$$

here, V is the applied bias, V_i is the built-in voltage, n_0 is the concentration of the electron at the outside of depletion region of the neutral semiconductor, ϕ_n represents the Fermi level penetration in the band gap of the semiconductor. Therefore, equation (2.20) can be rewritten as,

$$n^{*} = N_c \exp\left[\frac{-\left(\phi_B - qV\right)}{kT}\right] \tag{2.22}$$

where, $\phi_B = qV_i + \phi_n$. For the isotropic distribution, the number of electrons incident on the barrier is considered as $n^{*}\bar{v}/4$, and $\bar{v}$ is the defined as the average velocity due to thermal energy of the electron in the semiconductor. So, the current generated due to the electron transfer from the semiconductor to metal is followed as,

$$I_{SM} = \frac{qA\bar{v}}{4} N_c \exp\left[\frac{-\left(\phi_B - qV\right)}{kT}\right] \tag{2.23}$$

Whereas, the current due to the electron flow from metal into semiconductor can be expressed as,

$$I_{MS} = -\frac{qA\bar{v}}{4} N_c \exp\left[\frac{-\phi_B}{kT}\right] \tag{2.24}$$

Hence, the total current would be zero when the bias is not applied. Therefore, the total current under the bias can be written as,

$$I = I_0\left[\exp\left(\frac{qV}{kT}\right)-1\right] \quad (2.25)$$

Where, I_{MS} is equal to saturation current. For a Maxwell distribution, average velocity is considered as $\bar{v}=(8kT/\pi m^*)$. So, by substituting $N_c=2(2\pi m^* kT/h^2)^{3/2}$ and $\bar{v}$, equation (2.24) can be written as,

$$I_0 = AA^*T^2\exp\left[\frac{-\phi_B}{kT}\right] \quad (2.26)$$

Where, Richardson constant $A^*=4\pi qm^*k^2/h^3$.

In general, a basic diode is modeled with a series combination of resistance and diode and then the voltage drop across the diode is considered as V_D-IR_S. So, for V >3kT/q the equation (2.25) can be expressed in terms of current density(J=I/A) such as,[20]

$$J = J_0\left[\exp\left(\frac{q(V-R_SAJ)}{\eta KT}\right)\right] \quad (2.27)$$

By rearranging the equation (2.27), the applied voltage can be rewritten as

$$V = R_SAJ + n\phi_B + \frac{\eta kT}{q}\ln(J/A^*T^2) \quad (2.28)$$

By differentiating the voltage with respect to lnJ, equation (2.28) can be illustrated as[20]

$$\frac{dV}{d\ln(J)} = \frac{\eta kT}{q} + R_SAJ \quad (2.29)$$

The plot of dV/d lnJ versus the current density (J) gives the values of ideality factor and series resistance. Cheung et al. developed a formulation in 1986 that uses the current-voltage analysis to determine the barrier height and series resistance. According to their model, Cheung's function H(J) can be expressed as[20]

$$H(J) = V - \left(\frac{\eta kT}{q}\right)\ln\left(\frac{J}{A^*T^2}\right) = R_SAJ + \eta\phi_B \quad (2.30)$$

The values of barrier height and the series resistance can be obtained from the plot of H(J) versus current density.

2.4.2.2. Estimation of Mobility and Transit Time

One can further analyze the I-V characteristics by interpreting the carrier's mobility (μ_{eff}) and lifetime (τ) employing the space-charge limited current (SCLC) theory to explain the charge transport mechanism for different photo-induced applications.[21]

For positive bias, plotting log (I) vs log (V) yields multiple linear regions that represent various conduction methods. Interfacial trap states significantly impact the charge carrier conduction in metal-semiconductor junctions, changing I-V characteristic curves. Ohmic behavior (I α V) with a slope close to unity at low bias, demonstrates predominant conduction by intrinsic charge carriers.[22] Then, at the intermediate potential values, as the slope increases (usually reaching 2), injected carriers from the contacts start to predominate over intrinsic carriers, creating a spatially dispersed charge field. Mobility primarily governs quadratic current (I α V^2) in this region.[21, 23] Eventually, at higher applied voltages, the device surpasses the trap-filled limit, resulting in conduction primarily through 'trap-free space-charge limited current' characterized by power-law behavior (I α V^n, where n>2), corresponding to region III.[23] The mobility of electrons is estimated from the slope of the I vs. V^2 plot, according to the Mott-Gurney equation:[23]

$$\boldsymbol{I = \frac{9\mu_{eff}\varepsilon_0\varepsilon_r A_{eff}}{8}\frac{V^2}{d^3}} \qquad (2.31)$$

where, A_{eff}, ε_0, ε_r and d stands for the effective diode area, the free space permittivity, the dielectric constant of materials and the thickness of the diode, respectively. Here, the dielectric constant(ε_r) of the synthesized materials could be estimated from the capacitance (C) vs. frequency (f) plot, obtained from the measurement by an impedance analyser.

$$\boldsymbol{\varepsilon_r = \frac{C_0 d}{\varepsilon_0 A_{eff}}} \qquad (2.32)$$

where, C_0 is the saturated capacitance.[24]

Also, the life time or transient time (τ) of the charge carriers could be extracted employing the equation[25]:

$$\boldsymbol{\tau = \frac{9\varepsilon_0\varepsilon_r A_{eff}}{8d}\frac{V}{I}} \qquad (2.33)$$

2.4.2.3. Tunneling through the barrier

Wilson proposed the theory of quantum mechanical tunneling in 1934 to explain how the injected electrons may pass through the potential barrier. Due to a degenerate semiconductor's extremely high donor density at low temperatures, a thin potential barrier is formed, facilitating efficient tunneling. Therefore, a phenomenon known as field emission[13] occurs when the current develops in the forward direction. Conversely, when the temperature rises, electrons inhabit the higher energy level and the likelihood of tunneling increases. Consequently, the concentration of electrons with a definite energy rapidly decreases, while the contribution of electrons with a finite energy above the bottom of the conduction band causes the current to arise. This mechanism is known as Thermionic-field emission.[13] As the temperature rises, the electrons gain enough energy to flow through the barrier, reducing tunneling and preserving the charge transport mechanism via thermionic emission. In the presence of tunneling, the current-voltage characteristics can be explained as,

$$I = I_s \exp\left(\frac{qV}{E_0}\right) \tag{2.34}$$

$$\text{Where, } E_0 = E_{00}\coth\left(\frac{E_{00}}{kT}\right), \text{ and } E_{00} = \frac{qh}{4\pi}\left(\frac{N_d}{m^*\varepsilon_s}\right)^{1/2} \tag{2.35}$$

where m^* is the electron effective mass, h is Planck's constant, ε_s the semiconductor permittivity and N_d is the donor concentration,

2.4.2.4. Carrier recombination in the depletion region

Under zero bias voltage, the depletion region of the Schottky barrier is in thermal equilibrium. Subsequently, recombination plays a major role in the creation of electron-holes. Because of the applied bias voltage, the electron-hole product (n_i^2) at zero bias differs from its value. The excess electron-hole pairs ($>n_i^2$) generated in the depletion region of an n-type semiconductor-metal junction supply the reverse current when a reverse bias voltage is applied to the junction.

Moreover, forward recombination current is produced by the electron from the semiconductor and the holes from the metal recombining in the depletion region due to the forward bias. This current

dependents on the location of the recombination center, and it is most effective near the band gap center. The current (I_{rg}) due to this mechanism may be stated as,[26]

$$I_{rg} = I_{R0}\left[\exp\left(\frac{qV}{2kT}\right)-1\right] \quad (2.36)$$

Where, $I_{R0} = \frac{qAn_iW}{2\tau_0}$, τ_0 is the minority carrier lifetime in the depletion region, W is depletion region width.

2.4.2.5. Minority carrier injection

In an n-type semiconductor, the barrier height can occasionally be greater than the band gap. As a result, the region of the semiconductor vicinity to the metal contains a high amount of holes and behaves as p-type. Consequently, when a forward bias voltage is applied, the electrons flow to the metal from the semiconductors and diffuse the holes in that neutral region. Through this mechanism, some holes are injected from the metal into the semiconductor, where they eventually recombine with the electrons already there. The current due to the hole injection is defined by Yu and Snow and can be expressed as,[27]

$$I_p = \frac{qAD_pn_i^2}{N_dL_p}\left[\exp\left(\frac{qV}{kT}\right)-1\right] \quad (2.37)$$

Where N_d is donor concentration, L_p is the hole diffusion length, D_p is the hole diffusion constant.

2.4.3. Schottky Diode: Fabrication Technique

Material Selection: The particular type of semiconductor determines which metal is most appropriate for fabricating Schottky diodes. Platinum (Pt) or aluminum (Al) is frequently chosen for n-type semiconductors in order to establish a rectifying contact. Although silver (Ag) has great electrical conductivity, its application in metal-semiconductor junctions is limited by its oxidation susceptibility. Because of its resistance to high temperatures, indium tin oxide (ITO) onto glass substrate is used in thin film applications. For silicon-based Schottky diodes, silicon wafers are used with certain orientation, thickness, and resistivity.

Cleaning: ITO/wafers are carefully cleaned using trichloroethylene, acetone, and methanol solvents to make sure a clean surface. A 30–40% HF etching solution is used as the final cleansing step.[28]

Rinsing: Before beginning any further deposition processes, wafers are repeatedly washed in deionized (DI) water.

Deposition of Semiconducting Materials: Using spin coating units that rotate at a certain rpm, the materials to be utilized as the semiconducting layer are coated onto the ITO glass substrate. It is also possible to deposit the films of semiconducting materials using any other PVD technique, such as electron beam evaporation.

Ohmic Contact Formation: For effective electrical connections to semiconductor regions, Ohmic contacts are formed on the reverse side of silicon wafers. Vacuum coating units are used to deposit high-purity aluminium or any other chosen metal, keeping a steady low pressure for homogeneity up to a few tens of nanometers. By optimizing temperature, time, and pressure, annealing facilitates inter-diffusion and the formation of distinct Ohmic contacts.

Schottky Contacts: The native oxide layer is removed from silicon wafers by cleaning them and etching them in a 40% HF solution before metal deposition. Afterwards, a thin coating of the selected metal whose thickness can be optimized for desirable electrical properties, is placed onto the semiconductor surface employing deposition methods like sputtering or evaporation.

2.4.3.1. Importance of Aluminium in Fabrication of Devices

The most common metal on Earth, aluminium is distinguished for its remarkable flexibility, malleability, and lightweight nature. It is a comparatively soft metal when compared to many other metals. In addition to its mechanical properties, aluminum has excellent thermal and electrical conductivity and an excellent degree of corrosion resistance. Its inherent qualities may be preserved after recycling, making it extremely sustainable. Aluminum has a lower work function of 4.2 eV with electrical conductivity of 4.08×10^7 Sm^{-1},

while platinum, more cost effective and heavier metal, has a higher work function of 5.65 eV with electrical conductivity of $1.02x10^7$ Sm^{-1}.[29]

2.4.3.2. ITO Coated Glass Substrate in Fabrication of Devices: Features

Composed of indium (In), tin (Sn), and oxygen (O), indium tin oxide (ITO) has a composition of 74% In, 18% Sn, and 8% O. ITO is one of the most widely used transparent conducting oxides owing to its well-known properties of optical transparency, moisture resistance, electrical conductivity, and simplicity of deposition as a thin film. In general, physical vapour deposition methods are employed to create thin films of indium tin oxide onto glass surfaces. For thin layers, these films show an optical transmittance of more than 80% and a low electrical resistance of only 10^{-4} Ω-cm.[30]

2.4.3.3. Fabrication Technique: An Overview

Metal-semiconductor junctions are achieved using a vertical sandwich arrangement, particularly Al/synthesized material/ITO, which has been chosen due to the simplicity of junction fabrication. The thorough cleaning of the ITO is the first step in this process, requiring a comprehensive cleaning operation. The ITO-coated glass substrates are cleaned in stages. First, they are ultrasonically cleaned using a mild basic water solution that contains a tiny quantity of pure sodium hydroxide in distilled water. Next, they are rinsed with distilled water, acetone, and ethanol. The produced material is then spin-coated onto the previously cleaned ITO substrate at a predetermined rpm for several cycles after being dissolved or dispersed in an appropriate solution under ultra-sonication. After that, the produced films are dried for several hours in a vacuum chamber. The following step employs thermal evaporation to deposit aluminum metal onto the thin layer of the material. This method maintains a low pressure, generally at 10^{-6} mbar, by using an electron gun inside the vacuum coating unit. Applying a shadow mask while metal deposition ensures an efficient junctional area (7.065×10^{-6} m^2) and helps in defining the metal-semiconductor contact appropriately. The schematic representation of the device structure is provided in the following **Fig. 2.6.**

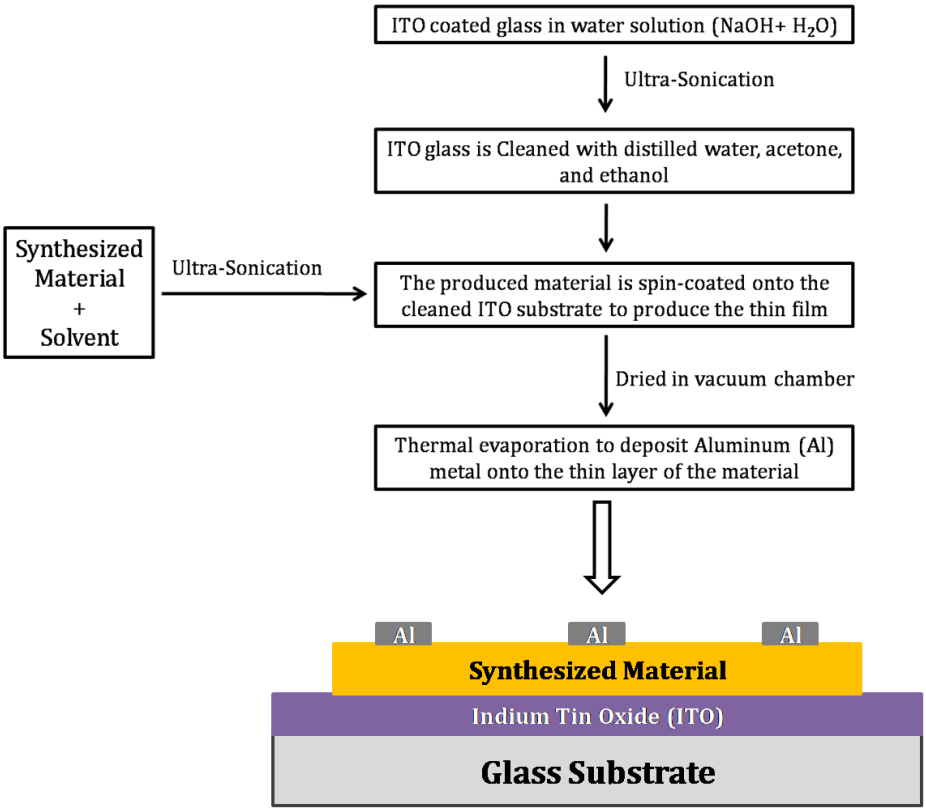

Fig. 2.6: The Schematic Representation of the Device

2.5. Estimation of HOMO-LUMO: An Overview of Cyclic Voltammetry

Cyclic voltammetry (CV) is a powerful and popular electrochemical technique commonly employed to investigate the reduction and oxidation processes of molecular species. CV is also invaluable to study electron transfer-initiated chemical reactions, which includes catalysis. Cyclic voltammetry is a sophisticated potentiometric and voltametric method. During a scan, the chemical either loses an electron (oxidation) or gains an electron (reduction). This will depend on the direction of the ramping potential. Cyclic voltammetry (CV) is a specific type of voltammetry, that is, an electrochemical potentio-dynamic

measurement that allows study of redox properties of compounds and interfacial structures. The graphical analysis of a cyclic voltammogram gives the redox peaks, which are reduction and oxidation peaks of the material, predicting the capacitive behaviour of the electrode. Hence, the potential at which the material is oxidized and reduced can be found.

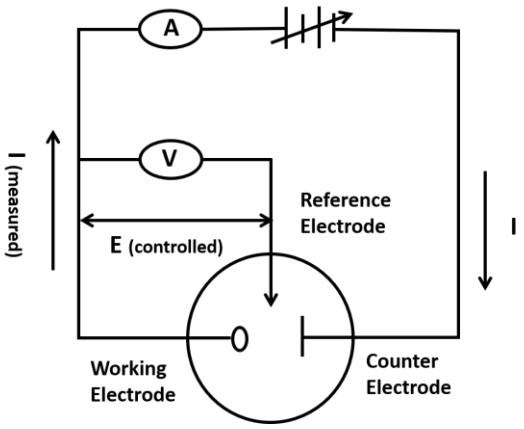

Fig. 2.7: Schematic view of Electrochemical Potential Analysis

By determining the oxidation peak (i.e. the ionization potential) and reduction peak (i.e. electron affinity) from the EC curve, the HOMO and LUMO energy position of the material can be estimated with the help of the following equations:

$$E_{HOMO} = -(E_{ox} + 4.4)\ eV \quad (2.38)$$

and

$$E_{LUMO} = -(E_{red} + 4.4)\ eV \quad (2.39)$$

where E_{ox} and E_{red} are the onset potentials of the oxidation and reduction relative to an Ag reference electrode. The value 4.4 eV represents the difference between the vacuum level potential of the normal hydrogen electrode and the potential of the Ag/AgCl electrode.[31, 32]

References

1. A. W. Burton, K. Ong, T. Rea and I. Y. Chan, *Microporous and Mesoporous Materials*, 2009, **117**, 75-90.
2. G. Williamson and W. Hall, *Acta metallurgica*, 1953, **1**, 22-31.
3. S. K. Suram, P. F. Newhouse and J. M. Gregoire, *ACS combinatorial science*, 2016, **18**, 673-681.
4. F. Reicha, M. Ishra and M. M. Gabr, *Journal of Physics and Chemistry of Solids*, 2003, **64**, 1157-1161.
5. T. S. Moss, *Optical properties of semi-conductors*, Butterworths Scientific Publications, London, 1959.
6. J. I. Pankove, *Optical processes in semiconductors*, Courier Corporation, 1975.
7. E. Barsoukov, *Impedance spectroscopy: theory, experiment, and applications*, 3rd edn., John Wiley & Sons, Hoboken, New Jersey, 2018.
8. V. F. Lvovich, *Equivalent-Circuit Elements and Modeling of the Impedance Phenomenon, Impedance Spectroscopy: Applications to Electrochemical and Dielectric Phenomena*, John Wiley & Sons, Hoboken, New Jersy, 2012.
9. F. Braun, *Annalen der Physik*, 1875, **229**, 556-563.
10. W. Schottky, R. Stormer and F. Waibel, *Z. Hoch Frequentztechnik*, 1931, **37**, 162.
11. W. Schottky, *Naturwissenschaften*, 1938, **26**, 843-843.
12. N. F. Mott, *Mathematical Proceedings of the Cambridge Philosophical Society*, 2008, **34**, 568-572.
13. E. H. Rhoderick, *IEE Proceedings-I, Solid-State and Electron Devices*, 1982, **129**, 1-14.
14. J. Bardeen, *Physical review*, 1947, **71**, 717.
15. A. Cowley and S. Sze, *Journal of Applied Physics*, 1965, **36**, 3212-3220.
16. M. Tyagi, in *Metal-Semiconductor Schottky Barrier Junctions and Their Applications*, ed. B. L. Sharma, Springer US, Plenum Press, New York, 1984, pp. 1-60.
17. C. Wagner, *Phys. Z*, 1931, **32**, 641-645.
18. W. Schottky and E. Spenke, *Wiss. Veroff. Siemens-Werken*, 1939, **18**, 225-291.
19. H. A. Bethe, *Theory of high frequency rectification by silicon crystals*, MIT Radiation Laboratory (US), United States, 1942.

20. S. Cheung and N. Cheung, *Applied physics letters*, 1986, **49**, 85-87.
21. I. Ullah, M. Shah, M. Khan and F. Wahab, *Journal of Electronic Materials*, 2016, **45**, 1175-1183.
22. İ. Taşçıoğlu, U. Aydemir and Ş. Altındal, *Journal of Applied Physics*, 2010, **108**, 064506.
23. M. Soylu and B. Abay, *Physica E: Low-dimensional Systems and Nanostructures*, 2010, **43**, 534-538.
24. K. C. Kao, *Dielectric phenomena in solids*, Elsevier, 2004.
25. S. Sil, A. Dey, J. Datta, M. Das, R. Jana, S. Halder, J. Dhar, D. Sanyal and P. P. Ray, *Materials Research Bulletin*, 2018, **106**, 337-345.
26. A. S. Grove, *Physics and technology of semiconductor devices*, John Wiley and Sons, New York 1967.
27. A. Yu and E. Snow, *Solid-State Electronics*, 1969, **12**, 155-160.
28. R. kumar and S. Chand, *Solid state science*, 2016, **58**, 115.
29. F. C. Walsh, *Transactions of the IMF*, 1991, **69**, 107-110.
30. J. Hass, R. Feng, T. Li, X. Li and Z. Zong, *Applied Physics Letters*, 2006, **89**, 143106.
31. E. Kucur, J. Riegler, G. A. Urban and T. Nann, *The Journal of chemical physics*, 2003, **119**, 2333-2337.
32. K. Deepa and J. Nagaraju, *Materials Science and Engineering: B*, 2012, **177**, 1023-1028.

Chapter 3

Investigation of conduction kinetics in Al/$CuInSe_2$ Schottky device utilizing Impedance Spectroscopy (IS) measurement and study of its photosensing behaviour

Investigation of conduction kinetics in Al/$CuInSe_2$ Schottky device utilizing Impedance Spectroscopy (IS) measurement and study of its photosensing behaviour

Abstract

Copper Indium Selenide ($CuInSe_2$) has been synthesized by solvothermal synthesis method. The Schottky diode (SD) has been fabricated by using the material and the interface characteristics of Al/$CuInSe_2$/ITO have been investigated with the help of ac impedance spectroscopy (IS) analysis (under dark condition) and dc current-voltage (I-V) measurements (under both dark and photo condition). IS is a very important and powerful technique to investigate and analyze the impedance at the boundary regions of SDs. Ac impedance spectra of Al/$CuInSe_2$ SD have been recorded in the wide range of frequency from 40 Hz to 20 MHz during dc bias scanning from -0.5 V to 0.5 V under dark condition. From forward I-V characteristics, important parameters such as ideality factor (η), photosensitivity, barrier height (Φ_b), series resistance (R_S) of SD were obtained under dark and photo condition. The photosensitivity of the Al/$CuInSe_2$ SD was found to be 3.36. For better realization of charge transport phenomena through the MS junction, space charge limited current (SCLC) theory has been employed. The effective mobility of the carrier is evaluated in dark and photo condition as 0.42×10^{-3} $m^2V^{-1}s^{-1}$ and 2.11×10^{-3} $m^2V^{-1}s^{-1}$ respectively. It has been observed that the mobility is improved 5 times under illumination compared to the dark condition.

3.1. Introduction

For the sake of conservation of energy, a low cost sustainable power source is extremely essential for the wellbeing of the human kind.[1] The conventional solar cells being very costly, it requires a search for materials for solar energy conversion. Photovoltaic cells based on I–III–VI compounds have shown a lot of promises for solar energy harvesting. Copper indium selenide ($CuInSe_2$) is one of those promising materials and a ternary chalcopyrite IB-IIIA-VIA compound semiconductor. It (CIS) has been one of the most potential absorber materials because few of its alluring characteristics for photovoltaic application such as high optical absorption coefficient, suitable band gap[2, 3] that can harvest a wide range of visible lights which are ideal for the development of photovoltaic devices. This material has gained much attention for the researchers everywhere throughout the world also because of its good stability under radiation, low toxicity and high efficiency of PV devices.[4] Furthermore, one can reduce the absorption layer up to a several micrometers and by substituting of In^{3+} by Ga^{3+} the band gap can be adjusted from 1.00 eV to 1.68 eV.[2] In view of such optical and electrical properties it has became one of the most significant photovoltaic materials. Various researchers have paid their attention for the measurements of thermal conductivity, optical absorption, Raman spectra and magneto-resistance on both single and polycrystalline samples.[5-9] R. Bouferra et al.[10] reported the AC conductivity of n-$CuInSe_2$ material utilizing impedance spectroscopy (IS) over a broad range of temperatures [80 K-300 K] and frequencies [20 Hz-1 MHz]. The report also provided some useful insight about the conduction mechanism in the material. However, metal-semiconductor (MS) contacts are mostly used as rectifying junction for different electronic devices like solar cells, ICs and photosensitive detectors.[11-15] As the MS junction plays a pivotal role in different microelectronic devices, the study of the influence of this material on the performance of electronic device is very important. Theoretically the MS junction will be Ohmic or Schottky depends on the work function of the metal and energy band position of the material but in practical application Fermi level pinning may play an important role in determining the Schottky junction. The quality of the interface between metal and semiconductor material dictates the performance and legitimacy of a Schottky diode (SD).[16]Few important parameters which give an idea about the junction are barrier height, ideality factor etc. In

recent past SDs have received considerable attention due to its simplistic fabrication procedure and it has a very fast recovery time which can be mostly used in the application of high-speed switching operation.[17, 18] Therefore, scientists are developing different materials for the application in SDs with improved performance which will be beneficial for future generation electronic devices.

While substantial research efforts have been given to fabricate photovoltaic devices using $CuInSe_2$, reports on the Schottky junctions using $CuInSe_2$ films is comparably low, though the Schottky junction of $CuInSe_2$ is an example of simple MS junction.

In this context, I have synthesized $CuInSe_2$ material with the help of solvothermal synthesis technique. Structural, optoelectronic and electrical properties of the newly synthesized material have been analyzed thoroughly. I have fabricated the Al/$CuInSe_2$/ITO sandwich structure and by current-voltage (I-V) measurements, the electrical transport properties of the SD have been studied under dark as well as illumination condition. The theoretical ideal thermionic emission current model has been employed to investigate the forward current-voltage (I-V) characteristics as the electrical behaviour of most of these junctions is close to this theory.[19, 20] In addition to the I-V study, Impedance Spectroscopy (IS) technique which has already been accepted as a powerful tool to understand the properties of the interfaces was applied. The charge transport conduction mechanism which is dominant at the interface has also been analyzed by IS technique. The IS analysis of Al/$CuInSe_2$/ITO SD is executed in the frequency range of 40 Hz to 20 MHz for different bias voltage under dark. The IS data of SD has been interpreted with the help of an ac equivalent circuit of RC parallel network. The work presented in this paper is of particular importance as we all know that IS is mostly used by researches to interpret the interface of various semiconductor devices. By utilizing this method, I obtained a proper equivalent circuit model for the analysis. The total variation of impedance which rapidly changes with the bias voltage is dependent on the Schottky contact formation at the interface of Al/$CuInSe_2$. The purpose to analyze the impedance behavior is to distinguish the impact of the interfaces in the total conduction mechanism. Here, the experimental analyses have assured us that the metal compound interface is behaving as the Schottky contact and dominates the conduction mechanism. Furthermore, utilizing I-V characteristics, I have extracted relevant parameters of the device, such as barrier height (φ_b), ideality factor (η) and series resistance (R_S). My

study unveils an important mechanism, which significantly contributes to the electrical transport in the Al/$CuInSe_2$ junctions. With the help of that Space Charge Limited Current (SCLC) theory, the charge transport mechanism within the device under dark and light condition has been well analyzed.

3.2. Experimental Section

3.2.1. Materials

Sodium Selenite (Na_2SeO_3, 99%) was purchased from Sisco Research Laboratories Pvt. Ltd., Indium (III) Chloride ($InCl_3$,99.99%) was purchased from Spectrochem Pvt. Ltd. And Copper (II) nitrate ($Cu(NO_3)_2$, $3H_2O$, 99%) and Dimethylformamide (DMF, >99%) were purchased from Sigma-Aldrich. All the materials were utilized as bought with no more purification.

3.2.2. Synthesis

In first reaction, 0.259 g (0.05 M) of Sodium Selenite (Na_2SeO_3) was mixed with 0.362 g (0.05 M) of Copper Nitrate $Cu(NO)_3$ in 30 ml of deionised water and stirred it for 15 minutes. The precipitation of green precursor indicates the successful synthesis of the Copper Selenite ($CuSeO_3$) particles.

In the second reaction, 0.777g (0.05 M) of Sodium Selenite (Na_2SeO_3) was mixed with 0.663 g (0.05 M) of Indium Chloride ($InCl_3$) in 30 ml of deionised water to get Indium Selenite ($In_2(SeO_3)_3$) and after 20 minutes the desired white-coloured precipitates ($In_2(SeO_3)_3$) were obtained. Before being dried up, the green ($CuSeO_3$) and white ($In_2(SeO_3)_3$) precipitates were filtered and washed a few times and collected.

Copper Indium Selenide ($CuInSe_2$) was prepared by reacting a suitable amount of $CuSeO_3$ and $In_2(SeO_3)_3$ (1:1 mol/ mol) in 30 ml of DMF. The solution was stirred for around an hour and afterward moved into a 50 ml Teflon-lined stainless-steel autoclave. The autoclave had to be fixed in a proper way and heated in an air-oven for 48 h at a temperature of 200 ºC. Once the reaction was over, it was allowed to cool to room temperature. The final precipitates (ppt) were collected and cleaned well with distilled water and ethanol more than once to get rid of the residual impurities and then dried.

The ultimate solution was shifted to an autoclave. It was vacuum-packed and heated nightlong at150 °C. Thereafter it had been left to cool to room temperature. The resultant precipitates (ppt) were cleaned with distilled water and ethanol over and again to dissociate all the dissolved species. It was heated at 80 °C within a vacuum oven for 4 h. This is how a dark black powder had been obtained and utilized for characterization.

3.2.3. Device Fabrication

In order to construct the Schottky device, at the start, the glass substrate coated with Indium Tin Oxide (ITO) was cleansed with acetone, distilled water and isopropanol over and again and consecutively in ultrasonication bath for about 20 min. At the same time a well dissolved solution of the $CuInSe_2$ in N, N-dimethylformamide (DMF) medium was prepared. With the help of SCU 2700 spin coating unit the solution was coated onto the pre-cleaned glass substrate at 800 rpm for 1 min. The above saidcoating stepwas repeated for 4 times. With the help of a Vacuum Coating Unit 12A4D of HINDHIVAC the Aluminium (Al) electrodes were deposited onto the film. A pressure of 10^{-6} Torr was maintained throughout during the deposition of the electrodes. The shadow mask was so arranged that the area of the Al electrodes can be kept up as 7.065×10^{-6} m^2. The current-voltage measurements of the device were performed in the voltage range -2V to +2V at room temperature by a Keithley 2635B source meter which was interfaced with a PC by two-probe technique under dark and illumination condition.

3.2.4. Characterization

By a Bruker D8 powder X-Ray Diffractometer, Powder X-ray diffraction experiment had been carried out ($\lambda_{CuK\alpha}$ = 0.15418 nm) in order to obtain the phase structures of the sample. Field emission scanning electron microscopy (FESEM) image was collected by an FEI Inspect F50. For FESEM, the powder samples were dispersed in DMF and drop casted on a glass substrate. The evaluation of the optical band gap energy was done with the help of the UV-vis absorption data which was recorded by Perkin Elmer UV-vis Lambda 365. The ac impedance spectroscopy study had been performed by computer interfaced Agilent 4294A precision impedance analyzer. The EIS spectrum analyzer software was utilized to fit the experimental data of Nyquist plot by means proper ac equivalent circuit. The electrical

conductivity of the material was estimated by measuring the current-voltage characteristic under dark and light (AM 1.5G radiation) condition using Keithley 2635B source meter interfaced with PC. All the arrangements and every measurement mentioned above were executed under ambient conditions.

3.3. Results and discussion:

3.3.1. Structural characterization:

Powder X-ray diffraction (PXRD) study is an effective technique to identify the phase and size of the crystalline nanoparticles. The PXRD patterns of synthesized sample are displayed in **Fig. 3.1**. The PXRD spectra shows the major diffraction peaks at 26.81°, 44.59° and52.70°, which are assigned to (112), (220/204) and (116/312) planes respectively. The detected diffraction peaks well correspond to the JCPDS file no. 40-1487of copper indium selenide ($CuInSe_2$) (Tetragonal).

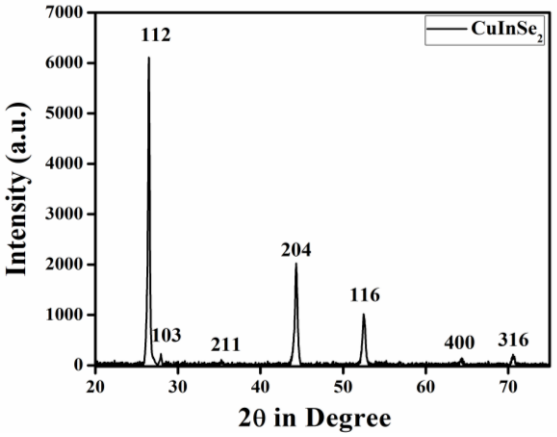

Fig.3.1: PXRD pattern of $CuInSe_2$

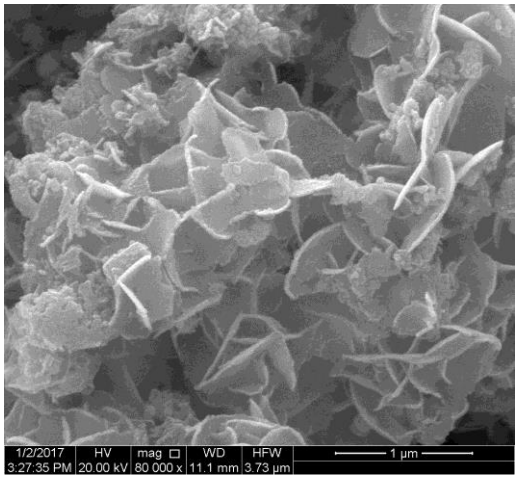

Fig. 3.2: FESEM image of $CuInSe_2$

The Field Effect Scanning Electron Microscopy (FESEM) image for $CuInSe_2$ material is shown in **Fig. 3.2**. The FESEM image exhibits the flower shape micro-architecture consists of nano-flakes.

3.3.2. Optical characterization:

The optical characterization of synthesized material had been carried out based on UV-vis spectrum. Since the synthesized material produces a consistent dispersion in N, N-dimethylformamide (DMF), thin films were prepared on regular glass substrate. The measurement of optical spectra of synthesized $CuInSe_2$ (**Fig. 3.3** inset) had been carried out

in the interval of 300-900 nm. The estimation of the optical band gap of $CuInSe_2$ thin film had been obtained from UV-vis spectrum using Tauc's equation (Eqn. 3.1)[21, 22]:

$$(\alpha h\nu) = A(h\nu - E_g)^n \quad (3.1)$$

Here α is the absorption coefficient, E_g the band gap, h the Planck's constant and ν frequency of incident photon. 'A' is a constant and taken to be 1 for ideal case. The exponent 'n' is a constant which can have different values depending on electron transition processes. In the above-stated equation the value of 'n' has been taken as ½ which corresponds to the direct allowed transition.[22] The direct band gap in this system has been calculated by plotting $(\alpha h\nu)^2$ *vs.* $h\nu$ as displayed in **Fig. 3.3** extrapolating the linear portion of the plot to α = 0 absorption. From data it has been found that the value of direct optical band gap (E_g) of my synthesized $CuInSe_2$ is 1.58 eV. This obtained value of band gap quite well matched with previously reported literature. [2, 23-25] Among them, Sakata et al. reported the direct optical band-gap energy of flash-evaporated amorphous $CuInSe_2$ films in the range of 1.21-1.41 eV.[23] Then, Guillen et al. obtained the direct optical band-gap energy of electrochemically deposited $CuInSe_2$ thin films in the range 1.32-1.41 eV.[24] Altındal et al. reported three different band gaps, which were determined as 1.06, 1.17 and 1.39 eV, respectively.[2] Similarly Kim et al. found the optical direct band-gap energy of as-deposited $CuInSe_2$ thin film as 1.54 eV.[25]

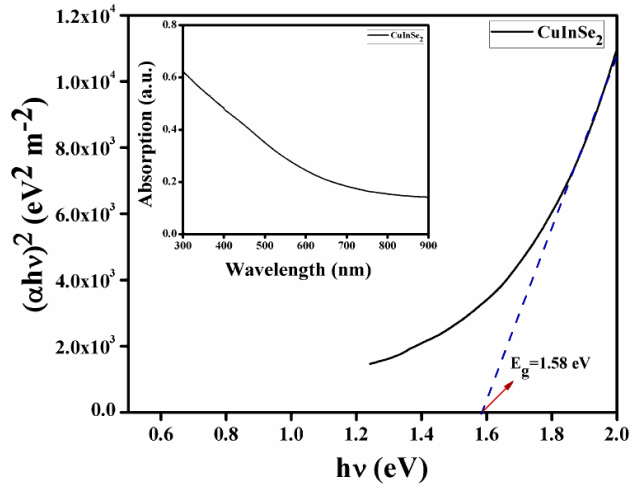

Fig. 3.3: Tauc's plot and UV absorption (inset) spectrum of $CuInSe_2$

3.3.3 Electrical characterization

3.3.3.1. Impedance Spectroscopy (IS)

IS is an impactful and convincing strategy to depict the event of conduction mechanism in the material or in any device. The study of AC impedance spectroscopy of Al/$CuInSe_2$/ITO Schottky diode (SD) has been explored in frequency interval of 40 Hz- 20 MHz under the

perturbation voltage of 100 mV. The bias voltage scanning has been carried out in the step of 0.1 V from -0.5 V to +0.5 V under dark condition at room temperature. **Fig. 3.4 and Fig. 3.5** exhibit the Nyquist plot of the diode.

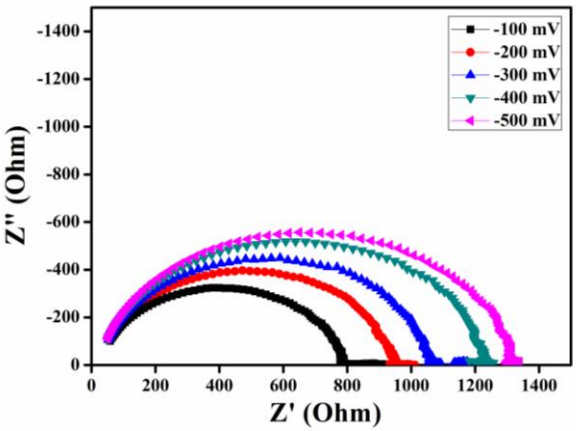

Fig. 3.4: Impedance spectra: under dark condition and reverse bias voltages

Fig. 3.4 shows the plot under reverse bias and the **Fig. 3.5** shows the same plot under zero and forward bias condition. The complex impedance plot referred as Nyquist plot consists of semicircles with various applied voltages and the arc of the semicircle is associated with the overall impedance behavior of the fabricated diode. It was noticed that as the positive dc bias decreases, the radius of the semicircles increases and it further increasesas the bias goes negative. This observation suggests that the device impedance is very much dependent on the dc bias applied. Due to the application of negative bias across the Schottky junction the semiconductor Fermi energy level reduces with respect to the Fermi energy level in the metal. That in turn raises the potential through the semiconductor, producing a widened depletion zone and a stronger electric field at the interface.[26] Under this reverse bias condition, the further flow of electrons is restricted as a barrier is produced at the metal-semiconductor interface. But incase of forward dc bias, the Fermi energy level of the semiconductor is increased compared to the metal which results potential reduction across the semiconductor. By raising the forward bias, the barrier height has been lowered which disturbs the total balance between diffusion and drift process. As results of that, more number of electrons is dominated by the diffusion in the direction of metal than the drifted electrons towards the

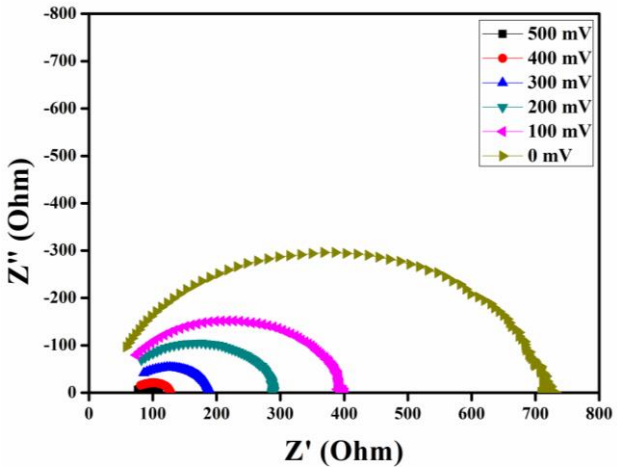

Fig. 3.5: Impedance spectra: under dark condition and zero and various forward bias voltages

semiconductor. The semi-circular like impedance spectra of the Schottky junction for a certain applied voltage may be explained by theoretical circuit model comprising of a resistance and a capacitance (RC network) connected in parallel connection.[27] The model of equivalent circuit is portrayed in **Fig. 3.6** which has two parallel RC networks connected in series with a series resistance and a supporting inductance.

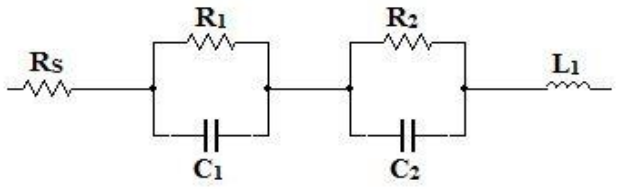

Fig. 3.6: Equivalent circuit of Al/$CuInSe_2$ Schottky Diode

One of the parallel RC systems is related to the interfaces of ITO/$CuInSe_2$ and another is related to that of $CuInSe_2$/Al. The complex impedance (Z^*) of the diodecan bewritten as:

$$Z^*(\omega) = Z' - jZ''$$

Where, ω denotes the angular frequency, Z' is the real part of the impedance and Z'' is the imaginary part of the impedance. The equivalent circuit model which is mathematically apprehended for Z' and Z'' of ac impedance can be written as:

$$Z'(\omega) = \frac{R_1}{1+(\omega R_1 C_1)^2} + \frac{R_2}{1+(\omega R_2 C_2)^2} + R_S$$

$$Z''(\omega) = \frac{\omega R_1^2 C_1}{1+(\omega R_1 C_1)^2} + \frac{\omega R_2^2 C_2}{1+(\omega R_2 C_2)^2} - \omega L$$

The depletion zone capacitance created at the contact is indicated by the capacitance component (C_1, C_2) in the equivalent circuit and the resistance component (R_1, R_2) of the same corresponds to the shunt resistance.[28]

The Nyquist curves have been fitted by EIS fitting software under different dc bias voltage fetching the experimental data subject to the above condition. **Fig. 3.7 (a, b)** exhibits every single fitted curve for reverse bias, zero and forward bias condition. It is evidently observed from the curve that the experimental and fitted information are perfectly matched. The value of R_S across the entire dc bias regime almost maintains a constant value (**Fig. 3.8**). It can be observed that once the biasing condition switches from reverse to forward regime, the value of R_1 encounters a distinctive reduction.

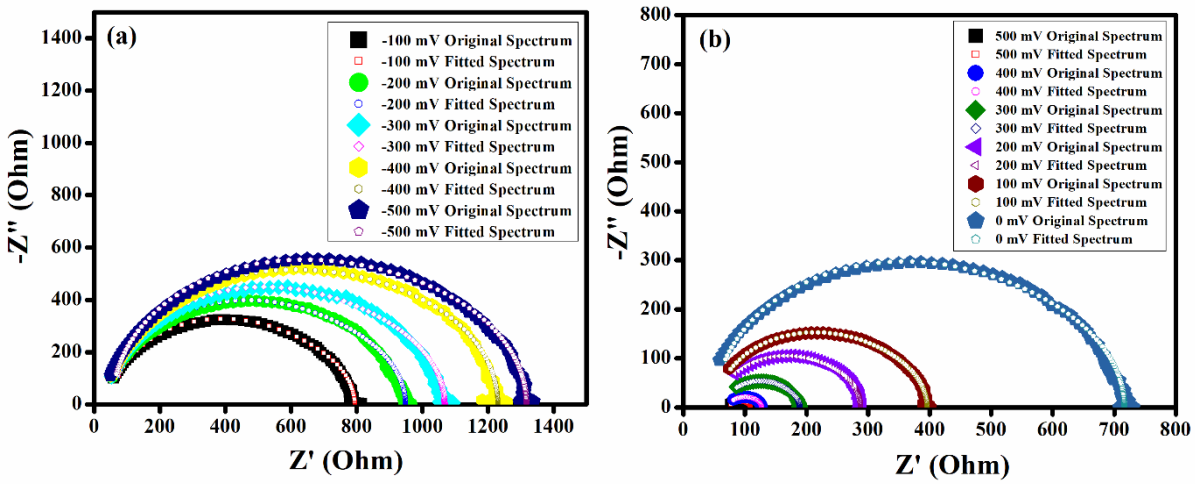

Fig. 3.7: Experimental and fitted Nyquist spectra of Al/$CuInSe_2$ SD under different dc bias voltages **(a)** -0.5V, -0.4V, -0.3V, -0.2V, -0.1V and **(b)** 0V, 0.1V, 0.2V, 0.3V, 0.4V, 0.5V

This implies that, the equivalent circuit component i.e. R_1C_1 is very much linked with the development of the Schottky barrier at the Al/$CuInSe_2$ junction in view of the fact that R_1 weakens the flow of current across the Schottky junction when the circuit is in reverse bias condition. Upon applying the forward dc biasing, R_1 immediately falls and it decreases considerably with the bias voltage advances. This is because of the fact that the flow of

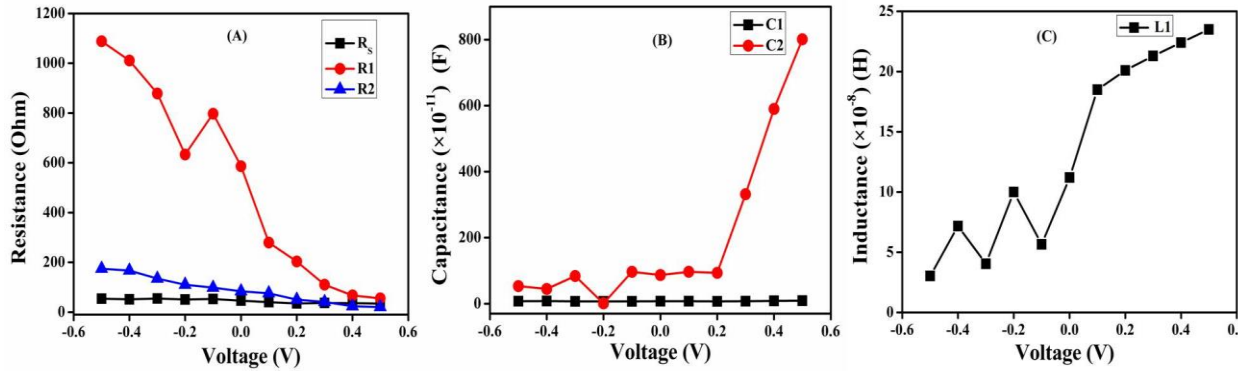

Fig. 3.8: The variation of R_S, R_1, C_1, R_2, C_2, and L_1 with the applied dc bias voltages achieved from the best fit of the measured impedance spectra of the Al/$CuInSe_2$ SD using the equivalent circuit model

current across the Schottky junction increases notably as forward bias brings down the barrier developed at the interface.[29] The second RC component (R_2C_2) which corresponds to the ITO/$CuInSe_2$ junction, does not exhibit much changes through the entire dc bias range. Actually, in perfect instances, the ITO/$CuInSe_2$ interface must not be affected by the externally applied bias voltage; however, some unavoidable defects produced at the interface may cause a little change in real cases.

3.3.3.2 Current - Voltage (I-V) characterization

The suitable optical band gap implies that $CuInSe_2$ I have synthesized is a semiconducting material. Henceforth, I have developed metal (Al)-semiconductor ($CuInSe_2$) (MS) junction thin film devices and by considering the charge transport behaviour I have studied its various electrical parameters. The I-V characteristics of the devices based on synthesized $CuInSe_2$ have been obtained under both dark and illumination condition and the same is shown in **Fig. 3.9**.

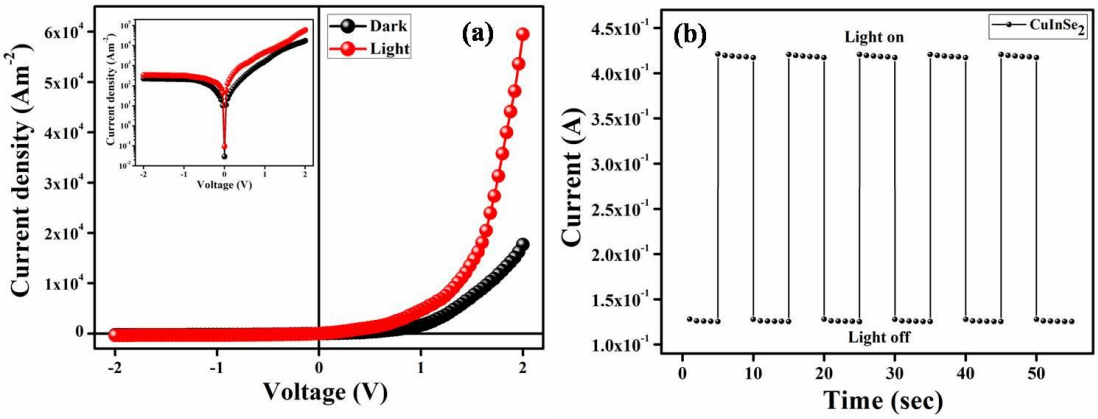

Fig. 3.9: (a) I-V characteristics curve of Al/$CuInSe_2$ SD under dark and photo illumination condition, **(b)** Transient photocurrent response

The electrical conductivity of the devices has been found to be as 1.26×10^{-3} Sm^{-1} at dark condition which is very likely that of a semiconductor. Though, after exposed at the photo-irradiation, the conductivity has been increased and found to be as 3.75×10^{-3} Sm^{-1}. It is very obvious from the above observation that the conductivity of the devices base on the synthesized material ($CuInSe_2$) has been significantly improved under the illumination conditions from the dark conditions. Nevertheless, the representative I-V characteristic of the Al/$CuInSe_2$ contact under both dark and illumination condition exhibits the nonlinear rectifying behaviour which is very likely to the Schottky diode (SD).

The rectification ratio (I_{on}/I_{off}) of the SDs under both dark and illumination conditions at ±2 V has been obtained as 78 and 172 respectively. The higher value of current from the characteristics curve under illumination demonstrates the photosensitivity of the devices and in my case it was found to be 3.36 for $CuInSe_2$ based SD. The photosensitivity (P_S) of the

diode is defined as the ratio of photocurrent (Iph= I_L-I_D; I_L is the current under light) to the dark current (I_D).[30, 31] The photosensitivity of the diode is expressed as:

$$P_S = \left(\frac{I_L - I_D}{I_D} \right)$$

Furthermore, the thermionic emission theory has been exploited to study the I-V characteristic of the SDs based on the material ($CuInSe_2$). The Cheung's method has been used to obtain some useful diode parameters.[32] The I-V characteristic curves have been studied thoroughly and quantitatively taking into account the under mentioned standard equations[32, 33]:

$$\boldsymbol{I = I_0\, exp\left(\frac{qV}{\eta kT}\right)\left[1 - exp\left(\frac{-qV}{kT}\right)\right]} \quad (3.2)$$

$$\boldsymbol{I_0 = AA^{*}T^{2} exp\left(\frac{-q\emptyset_B}{kT}\right)} \quad (3.3)$$

Here, I_0 represents the saturation current, q is the charge of electronic, k is the Boltzmann constant, T is temperature in Kelvin, V is the forward bias voltage, A is the effective diode area, η is the ideality factor, Φ_b is the barrier height and A^* denotes the effective Richardson constant. The effective diode area (A) was approximated as $7.065\times10^{-6}m^2$ whereas the effective Richardson constant (A^*) was considered to be as 32 $AK^{-2}\,cm^{-2}$ for every single device.[34]

The series resistance (R_S), η and Φ_b have further been determined by using the following referred equations (3.4) - (3.6) which have been derived from Cheung's equation,[33, 35]

$$\boldsymbol{\frac{dV}{dln(J)} = \left(\frac{\eta kT}{q}\right) + JR_SA} \quad (3.4)$$

$$\boldsymbol{H(J) = V - \left(\frac{\eta kT}{q}\right) ln\left(\frac{J}{A^{*}T^{2}}\right)} \quad (3.5)$$

$$\boldsymbol{H(J) = R_SJA + \eta\emptyset_B} \quad (3.6)$$

I have plotted a dV/dlnJ vs. J (**Fig. 3.10**) curve and from the intercept of it I have determine the ideality factor (η) under both dark and light condition. The slope of the plot corresponds to the series resistance (Rs) of the device. Table 3.1 displays the value of the determined ideality factors and which have been found to be as 1.93 and 1.35 respectively for dark and photo conditions for the SDs fabricated by the synthesized material ($CuInSe_2$). It is observed that the values of the ideality factors under both the conditions deviate a little from its ideal value (~1). The reason of the deviation may be because of the existence of inhomogeneities of Schottky barrier height, various interface states and series resistance at the junction.[36, 37] Nonetheless, it has been noticed that the value of ideality factor for the SDs under photo condition comes closer to the ideal value than that under the dark condition which is very important. Generally, it means a lesser number of recombination of interfacial charge carriers and it causes an improved homogeneity at the barrier of Schottky junctions.[26]

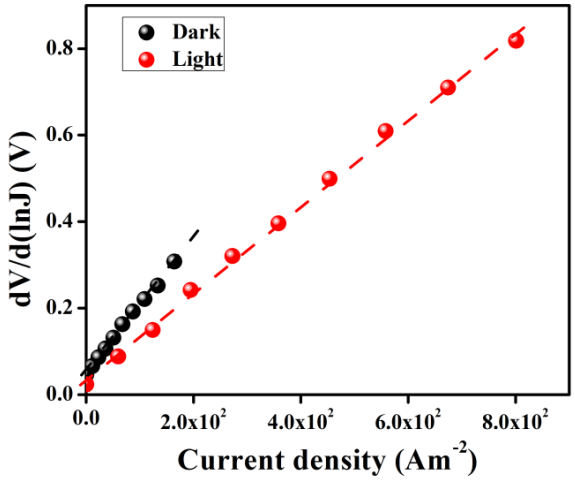

Fig. 3.10: dV/dlnJ vs. J curve for the devices based on $CuInSe_2$ under dark and photo illumination condition

By plotting H(J) vs. J curve (**Fig. 3.11**) and taking the intercepts of the curve I have determined the value of barrier height ($\emptyset_B$). Here I have utilised equation 3.6 mentioned above and the precalculated value of ideality factor (η).

I have noticed that the barrier potential height of the schottky device has been decreased significantly under photo illumination. In general, a considerable number of photo induced charge carriers are generated and these charges accumulate in the vicinity of the conduction band. This may be the reason of the reduction of barrier height. Furthermore, I can also measure the series resistance (R_S) of the devices by deducing the gradient of H(J) vs. J curve. Table 3.1 exhibits the values of potential barrier height (Φ_b), ideality factor (η) and series resistance (R_S) under both dark and irradiation condition of the metal (Al)-semiconductor ($CuInSe_2$) (MS) junctions that I have determined. It can be observed that the series resistance (R_S) that I have measured from both the methods appears to be very consistent and the value reduces when exposed under light as desired (Table 3.1). This particular characteristic of the constructed device confirms its relevance in the field of optoelectronics.

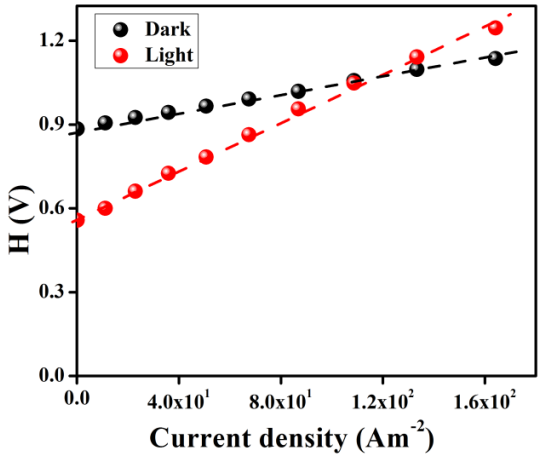

Fig. 3.11: H(J) vs. J curve for the devices based on$CuInSe_2$ under dark and photo illumination condition

Table 3.1: Schottky device parameters of $CuInSe_2$ based SDs

Condition	On/ Off	Conductivity σ (S-m^{-1})	Photo sensitivity	Ideality factor (η)	Barrier height ϕ_b (eV)	Series Resistance R_s	
						From dV/dlnJvs.J (Ω)	From H(J)vs.J (Ω)
Dark	78	1.26x10^{-3}		1.93	0.46	222.22	217.97
Light	172	3.75x10^{-3}	3.36	1.35	0.41	141.54	123.49

For better insight of the charge transport mechanism at MS junction, it is essential to explore the I-V curves very extensively. **Fig. 3.12** shows the characteristic I-V curves of the

device under both dark and light conditions in logarithmic scale. It appears that the I-V characteristic curve can be distinguished in two different slopes (**Fig. 3.12**) which has been labelled as Region-I and Region-II.

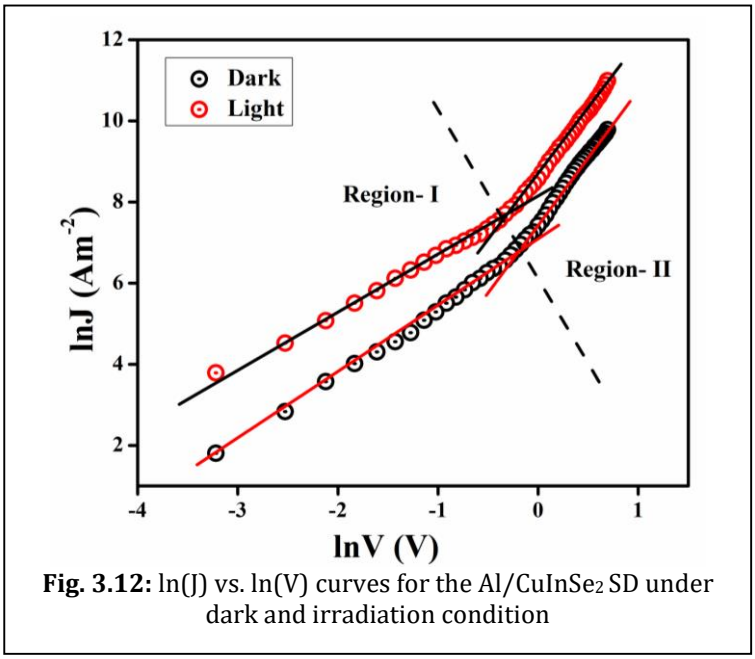

Fig. 3.12: ln(J) vs. ln(V) curves for the Al/$CuInSe_2$ SD under dark and irradiation condition

It can be observed that in the Region-I, the slope of the curve is near about 1. This makes sure that the current acts accordance with I∝V relation which is referred to as the Ohmic regime. In Region-II, the slope of the curve is about 2 which correspond to the current-voltage relation as $I \propto V^2$. This value of the slope specifies the regime as trap free space charge limited current (SCLC) regime.[22, 38] When the injected carriers exceed that of the background carriers, it outspread over the region and create a space charge field. This space charge field dominates the currents and thus the phenomenon is called as SCLC.[26, 38] In order to determine the performance of the device I have utilized this SCLC theory. According to this theory, the effective carrier mobility was predicted from higher voltage region of Jvs.V^2plot (**Fig. 3.13**) by Mott-Gurney equation[26, 35, 38]:

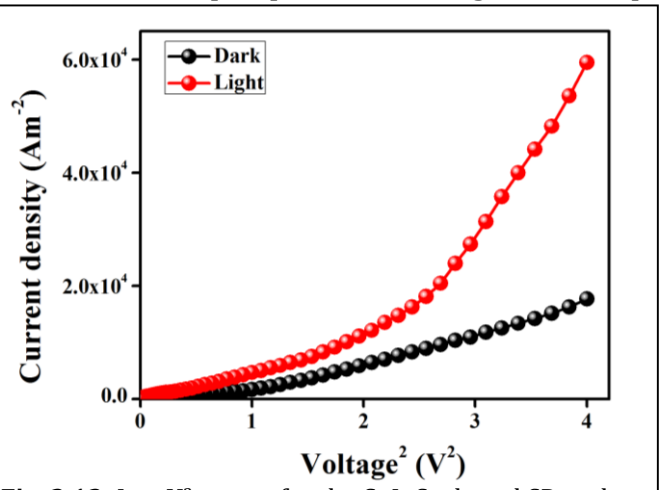

Fig. 3.13: J vs. V^2 curves for the $CuInSe_2$ based SD under dark and irradiation condition

$$J = \frac{9\mu_{eff}\varepsilon_0\varepsilon_r}{8}\left(\frac{V^2}{d^3}\right) \qquad (3.7)$$

Here, J is the current density, ε_0 is the permittivity of free space, ε_r is the relative dielectric constant of the synthesized material, μ_{eff} is the effective mobility of the carrier.

In order to determine the relative dielectric constant, I have plotted the capacitance against frequency at a constant bias potential of the material in film format (**Fig. 3.14**).

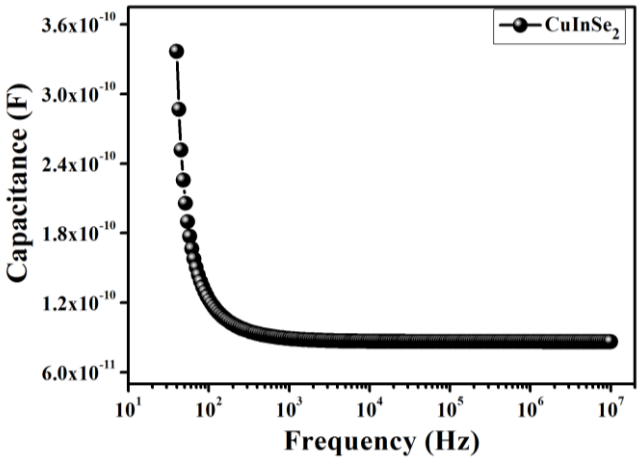

Fig. 3.14: Capacitance vs. Frequency graph to determine the dielectric constant

At the higher frequency regime where the value of capacitance gets saturated (**Fig. 3.13**), the dielectric constant of the material is evaluated utilising the equation mentioned below[22, 26]:

$$\varepsilon_r = \frac{Cd}{\varepsilon_0 A} \qquad (3.8)$$

Here, C is the capacitance at saturation, d is the film thickness (supposed as ~1 μm) and A is the effective area (7.065×10^{-6} m^2). Utilising the formula mentioned above I have calculated the relative dielectric constant which was found to be 1.38. I have also determined some crucial parameters like transit time (τ) and diffusion length (L_D) to investigate the charge transport mechanism through the junction. To study this mechanism, I have utilized the slope of the forward I-V curve (logarithmic representation) in SCLC region (region-II) displayed in **Fig. 3.12** and determined the transit time (τ).[21] The transit time (τ) of the charge carrier was deduced from the slope of I vs. V plot in region-II.

$$\tau = \frac{9\varepsilon_0\varepsilon_r}{8d}\left(\frac{V}{J}\right) \qquad (3.9)$$

$$\mu_{eff} = \frac{qD}{kT} \qquad (3.10)$$

$$L_D = \sqrt{2D\tau} \qquad (3.11)$$

Here, D is the diffusion coefficient and was estimated with the help of Einstein-Smoluchowski equation (Eqn. 3.10).[22] When a metal semiconductor junction is developed, the performance of the device is very much influenced by the diffusion length (L_D) of charge carriers and thus it has further been obtained from the above equation (Eqn. 3.11). For a

deep understanding of the charge transport mechanism, the DOS near the Fermi level has been determined from the SCLC region of the I-V characteristics. The distribution of the DOS of the films close to the Fermi level $N'(E_F)$ was obtained from I-V characteristics by employing the following relation:

$$N'(E_F) = \frac{2\varepsilon_0\varepsilon_r \Delta V}{qd^2 \Delta E_F} \quad (3.12)$$

Here $N'(E_F)$ is the density of localized states close to the Fermi level and the rest of the parameters are explained earlier. Near the Fermi level under dark and light induced condition, the density of localized states have been calculated as 3.55×10^{-39} and 5.41×10^{-39} $m^{-3}eV^{-1}$ consecutively. The value indicates that the DOS near the Fermi level is quite higher in magnitude upon photo illumination. So the performance as well as the rectification ratio of the device has increased once it is exposed in light. All the device parameters obtained in the SCLC region indicates the improvement of the charge transport properties after light absorption (Table 3.2). The higher mobility indicates the higher

Table 3.2: Charge conducting parameters of Al/$CuInSe_2$ SD

Condition	μ_{eff} ($m^2 V^{-1} s^{-1}$)	τ (s^{-1})	$\mu_{eff}\tau$ ($m^2 V^{-1}$)	D	L_D (m)	DOS N' ($m^{-3} eV^{-1}$)
Dark	4.21×10^{-4}	6.23×10^{-5}	2.62×10^{-8}	1.05×10^{-5}	3.62×10^{-5}	3.55×10^{-39}
Light	2.11×10^{-3}	1.84×10^{-5}	3.88×10^{-8}	5.27×10^{-5}	4.40×10^{-5}	5.41×10^{-39}

transport rate under illumination. The number of charge carriers has also been increased under illumination condition. The longer diffusion length under illumination reveals that the charge carriers got to traverse more length before being recombined. This results an expected current growth shown by the device under light. All the diode parameters of the $CuInSe_2$ based SD demonstrate much improved conduction mechanism after being light soaked. Therefore, it can be a highly potential material for application in light sensing device.

A schematic illustration of the band structure of the Al/$CuInSe_2$ junction is often helpful in understanding the mechanism of the diode action, which I have drawn on the basis of the estimated barrier height. **Fig. 3.15** shows a schematic diagram of the band structure of the synthesized $CuInSe_2$ based SD in this study

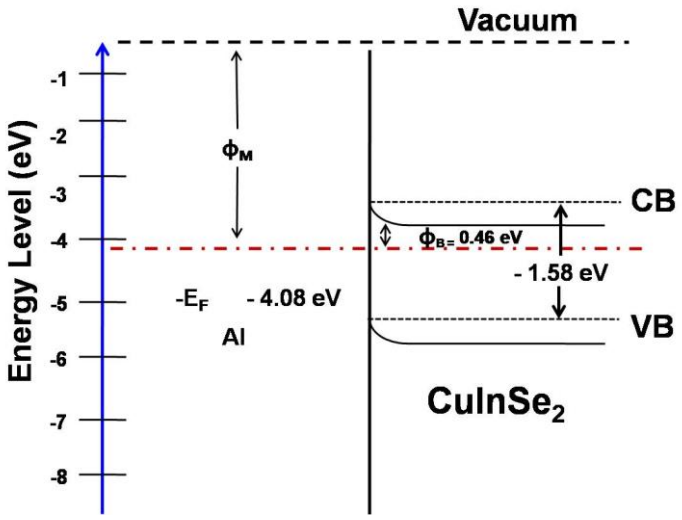

Fig. 3.15: Schematic band structure of the $CuInSe_2$ based SD

3.4. Conclusions

In this report, I have synthesized $CuInSe_2$ via solvothermal synthesis route and characterized the structural, optical and electrical properties. Al/$CuInSe_2$ SD was fabricated and investigated the electrical properties with the help of dc current-voltage (I-V) and ac impedance spectroscopy (IS) analysis. Fundamental diode parameters like ideality factor, barrier height and series resistance are obtained from conventional current-voltage characteristics (under dark and illumination) by adopting thermionic emission theory. Metal-semiconductor interfaces are properly identified by using impedance spectroscopy analysis at different dc bias under dark condition. Moreover, the charge transport mechanism through Al/$CuInSe_2$ is extensively analyzed by employing space charge limited current (SCLC) theory. After illumination of light the mobility is increased ~5 fold. In this study, I shed light upon charge transport properties and evaluation of Schottky interfaces with the help of I-V and IS measurement techniques.

References:

1. P. Hankare, K. Rathod, P. Chate, A. Jadhav and I. Mulla, *Journal of alloys and compounds*, 2010, **500**, 78-81.
2. H. Tecimer, S. Aksu, H. Uslu, Y. Atasoy, E. Bacaksız and Ş. Altındal, *Sensors and Actuators A: Physical*, 2012, **185**, 73-81.
3. M. Wang, S. K. Batabyal, Z. Li, D. Li, S. G. Mhaisalkar and Y. M. Lam, *RSC advances*, 2013, **3**, 9829-9834.
4. K.-J. Kim, R. P. Oleksak, C. Pan, M. W. Knapp, P. B. Kreider, G. S. Herman and C.-H. Chang, *RSC Advances*, 2014, **4**, 16418-16424.
5. A. Tiwari, D. Pandya and K. Chopra, *Solar cells*, 1987, **22**, 263-273.
6. I. Khatri, H. Fukai, H. Yamaguchi, M. Sugiyama and T. Nakada, *Solar Energy Materials and Solar Cells*, 2016, **155**, 280-287.
7. H. Shaban, M. Mobarak and M. Nassary, *Physica B: Condensed Matter*, 2007, **389**, 351-354.
8. S. Wasim, *Solar cells*, 1986, **16**, 289-316.
9. C. Rincon and F. Ramirez, *Journal of applied physics*, 1992, **72**, 4321-4324.
10. R. Bouferra, G. Marín, S. Amhil, S. Wasim and L. Essaleh, *Physica B: Condensed Matter*, 2019, **565**, 14-17.
11. N. G. Chopra, R. Luyken, K. Cherrey, V. H. Crespi, M. L. Cohen, S. G. Louie and A. Zettl, *science*, 1995, **269**, 966-967.
12. N. Dmitruk, O. Y. Borkovskaya, I. Dmitruk, S. Mamykin, Z. J. Horvath and I. Mamontova, *Applied Surface Science*, 2002, **190**, 455-460.
13. A. Saha, S. Chattopadhyay, R. Das, C. Bose and C. Maiti, *Solid-state electronics*, 2006, **50**, 1269-1275.
14. J. Osvald and Z. J. Horvath, *Applied surface science*, 2004, **234**, 349-354.
15. S. Chand and J. Kumar, *Journal of Applied Physics*, 1997, **82**, 5005-5010.
16. M. E. Aydın, N. Yıldırım and A. Türüt, *Journal of applied physics*, 2007, **102**, 43701-43707.
17. A. Di Bartolomeo, G. Luongo, L. Iemmo, F. Urban and F. Giubileo, *IEEE Transactions on Nanotechnology*, 2018, **17**, 1133-1137.

18. A. Di Bartolomeo, G. Luongo, F. Giubileo, N. Funicello, G. Niu, T. Schroeder, M. Lisker and G. Lupina, *2D Materials*, 2017, **4**, 025075.
19. S. M. Sze, *Physics of Semiconductor Devices*, Wiley, New York, 1981.
20. E. H. Rhoderick, *Metal-Semiconductor Contacts*, Clarendon Press, Oxford, 1978.
21. J. Tauc, *Amorphous and Liquid Semiconductors*, Plenum Press, New York, 1974.
22. A. Dey, S. Middya, R. Jana, M. Das, J. Datta, A. Layek and P. P. Ray, *Journal of Materials Science: Materials in Electronics*, 2016, **27**, 6325-6335.
23. H. Sakata and H. Ogawa, *Solar Energy Materials and Solar Cells*, 2000, **63**, 259-265.
24. C. Guillen and J. Herrero, *Solar energy materials*, 1991, **23**, 31-45.
25. C. R. Kim, S. Y. Han, C. H. Chang, T. J. Lee and S. O. Ryu, *Current Applied Physics*, 2010, **10**, S383-S386.
26. S. Sil, A. Dey, J. Datta, M. Das, R. Jana, S. Halder, J. Dhar, D. Sanyal and P. P. Ray, *Materials Research Bulletin*, 2018, **106**, 337-345.
27. S. Sil, J. Datta, M. Das, R. Jana, S. Halder, A. Biswas, D. Sanyal and P. P. Ray, *Journal of Materials Science: Materials in Electronics*, 2018, **29**, 5014-5024.
28. C. Yim, N. McEvoy, H.-Y. Kim, E. Rezvani and G. S. Duesberg, *ACS applied materials & interfaces*, 2013, **5**, 6951-6958.
29. A. Dey, J. Dhar, S. Sil, R. Jana and P. P. Ray, *Journal of Materials Engineering and Performance*, 2018, **27**, 2727-2733.
30. Q. Yang, X. Guo, W. Wang, Y. Zhang, S. Xu, D. H. Lien and Z. L. Wang, *ACS nano*, 2010, **4**, 6285-6291.
31. L. Dou, Y. Yang, J. You, Z. Hong, W.-H. Chang, G. Li and Y. Yang, *Nature communications*, 2014, **5**, 5404.
32. A. Dey, R. Jana, J. Dhar, P. Das and P. P. Ray, *Materials Today: Proceedings*, 2018, **5**, 9958-9964.
33. S. Cheung and N. Cheung, *Applied physics letters*, 1986, **49**, 85-87.
34. J. H. Werner and U. Rau, in *Silicon-Based Millimeter-Wave Devices*, Springer, 1994, pp. 89-148.
35. A. Dey, A. Layek, A. Roychowdhury, M. Das, J. Datta, S. Middya, D. Das and P. P. Ray, *RSC Advances*, 2015, **5**, 36560-36567.
36. R. Gupta and F. Yakuphanoglu, *Solar Energy*, 2012, **86**, 1539-1545.

37. X. Miao, S. Tongay, M. K. Petterson, K. Berke, A. G. Rinzler, B. R. Appleton and A. F. Hebard, *Nano letters*, 2012, **12**, 2745-2750.

38. P. W. Blom, M. d. de Jong and M. v. van Munster, *Physical Review B*, 1997, **55**, R656-R659.

Chapter 4

An experimental approach to ensure energy quenching and Fluorescence Resonance Energy Transfer of excitons from P3HT to $CuInSe_2$

An experimental approach to ensure energy quenching and Fluorescence Resonance Energy Transfer of excitons from P3HT to $CuInSe_2$

Abstract

This letter reports the paramount fluorescence resonance energy transfer mechanism for photo induced charge transfer from P3HT to solvothermally derived $CuInSe_2$. The HOMO (-4.85eV) and LUMO (-3.38 eV) energy states of $CuInSe_2$ (electrical conductivity =1.1x 10^{-7} Scm^{-1}) are determined from cyclic voltammetry and optical study. This HOMO-LUMO position agrees to select P3HT polymer as possible donor of excitons. Steady-state luminescence study of composite (P3HT:$CuInSe_2$) demonstrates possibility of successful charge transfer. Stern–Volmer analysis of absorption and emission spectroscopy ensures static energy quenching phenomena. The Förster distance (R_0) of critical energy transfer is estimated as 3.61 nm. The average distance between donor-acceptor (r_{avg}= 4.71nm) is less than 8 nm and within the range $0.5R_0 < r < 1.5R_0$ (1.81nm < r < 5.42nm), which ensures energy transfer from P3HT to $CuInSe_2$.

4.1. Introduction

In recent past $CuInSe_2$ (CIS) composite and its application as electron acceptors in photovoltaics has become more popular because of its semiconductor nature with narrow band gap, non-toxicity, high reproducibility, tuneable optical energy gap, and good stability.[1]In order to attain higher performance of organic-inorganic solar cell, conjugated polymer like poly(3-hexylthiophene) (P3HT) is appreciated yet as electron donor. Extensive studied had been performed by several scientists and researchers on energy harvesting from the P3HT: $CuInSe_2$composite based solar cells.[2] The understanding of underline physics of resonance energy transfer by quenching phenomena is an obvious commissioning task of charge transfer from donor to acceptor. However, the underline charge transport mechanism by fluorescence resonance energy transfer theory within this composite is not reported so far. Hence the field remains unexplored.

In this section the solvothermally derived $CuInSe_2$ is composited with P3HT to study the state of quenching which is highly responsible for understanding the hopping of excitons from donor to acceptor.[3] Even though CIS's applications in Schottky diode has been reported earlier,[4] perhaps this is the first approach to report the quenching phenomena and photo-induced charge transfer by utilizing FRET mechanism within the composite P3HT:$CuInSe_2$.

In this context, solvothermally derived CIS is characterized accordingly and the energy band positions are determined to find out the organic P3HT as appreciable donor with respect to CIS one. To get better insight the mechanism of energy quenching and the physics behind of hopping of excitons from donor to acceptor, the optical spectral (absorption and emission) analyses are performed pertinently. The analysis deserves a thorough inspection which is carried out by employing Stern-Volmer theory and Förster's equation for non-radiative energy transfer.[5, 6]

4.2. Materials and Methods

Poly(3-hexylthiophene) (P3HT) purchased from Sigma-Aldrich. Flake like $CuInSe_2$ is derived by Solvothermal technique (reported elsewhere).[4]FESEM and EDAX spectroscopy are performed with a FEI make Inspect F-50 scanning electron microscope equipped with energy-dispersive X-ray analysis system. Bruker D8 Advanced PXRD is used to record

diffraction. The absorption spectra are obtained from Perkin Elmer Lambda 365 spectrophotometer. Fluorescence spectra are recorded via Perkin Elmer LS-45 fluorimeter. The electrical conductivity (σ) is measuredbyKeithley2400 source meter unit. Electro-chemical (EC) voltammetry is performed with the help of (AUT204.S) electrochemical work station of Autolab make.

4.2.1. Preparation of thin film for Electrical measurement

The electrical conductivity of the sample is measured by thin film (sandwich structured) technique. In this regards a thin film of the sample is deposited on pre-cleaned Aluminium coated glass substrate. The film of the sample is spin coated and dried inside a vacuum heater. For top contact, aluminium is deposited by thermal evaporation technique with shadow masking. For the very purpose of measurement of conductivity thickness of the sample film is measured as 900nm (using surface profiler) and the active area is estimated from the dimension of mask as 7.065×10^{-6} m^2. The schematic presentation of conductivity measurement is illustrated in **Fig. 4.1**.

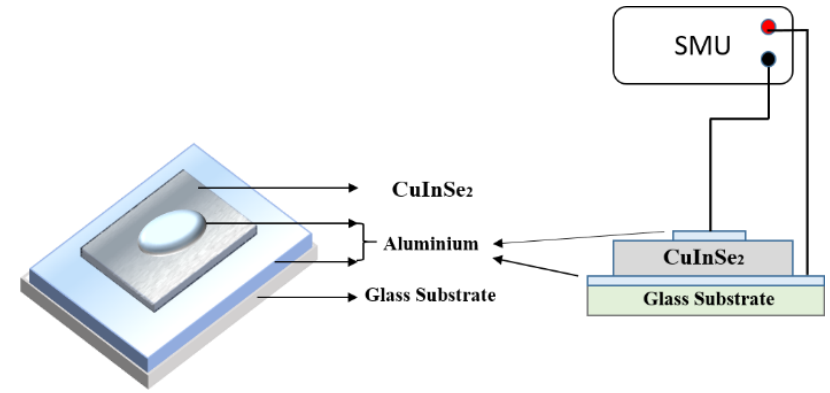

Fig. 4.1: Schematic Presentation: Electric conductivity measurement

4.2.2. Electro-chemical Measurement

In electro-chemical measurement a photo-catalyst powder-modified glassy carbon electrode (GCE) is considered as working electrode, the reference electrode is an Ag/AgCl (in 0.5 M KOH), and the counter electrode is a platinum wire. In determining the lowest unoccupied molecular orbital (LUMO) level from oxidation state, a value 4.4 eV is considered for the difference between the vacuum level potential of the normal hydrogen electrode and the potential of the Ag/AgCl electrode.

4.2.3. Sample Preparation for Optical data

A disperse solution of the synthesized CIS in chlorobenzene is prepared by ultra-sonication technique. The absorption and emission spectroscopy are performed by taking two stocks of 10 ml of P3HT and CIS separately. Spectra are recorded for P3HT and the solutions iteratively titrated by incorporating the stock of CIS accordingly by maintaining weight ratio.

4.3. Results and Discussions

4.3.1. Structural Analysis

The field emission scanning electron microscopy (FESEM) image (**Fig. 4.4**(a)) depicts that the particles are flake like with coagulations. The energy dispersive X-ray spectroscopy (EDAX) with automated atomic number-absorption and fluorescence (ZAF) corrections indicates the occurrence of Cu, In and Se in the sample at 22.49%, 24.45% and 53.06% respectively (Fig. 4.4(b)). The molar ratio from quantitative analysis of EDAX approves the stoichiometric formation of $CuInSe_2$.The responsible Bragg's diffraction peaks at angles 2θ = 26.48, 44.32, 52.48, 64.36, and 70.58 for (hkl) = (112), (204), (116), (400) and (316) approves tetragonal $CuInSe_2$, supported by the JCPDS Card No: 40-1487.[4] Fig. 4.2 illustrates the XRD spectra of $CuInSe_2$ (CIS).

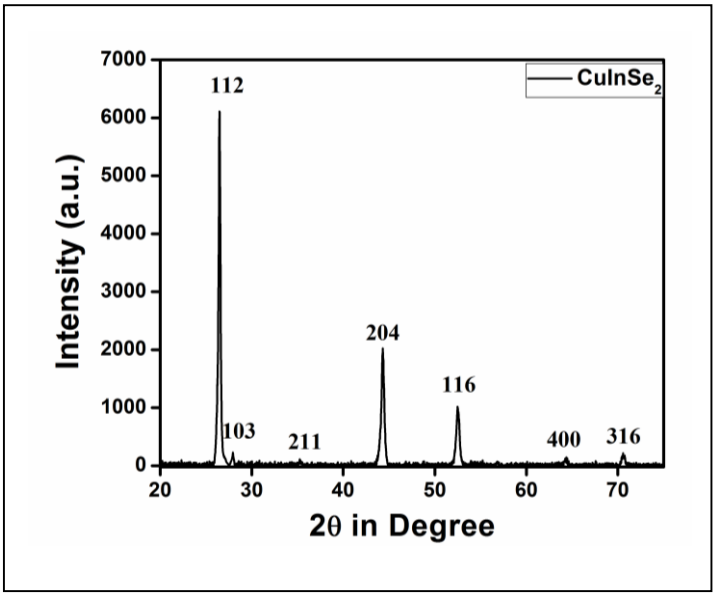

In the approach to estimate average crystallite size (D), Scherrer's equation of peak broadening (Eqn. 4.1) is considered for each typical peak of XRD spectrum and is determined as 26.25 nm (Given in Table 4.1).

$$\beta = \frac{K\lambda}{D}\left(\frac{1}{\cos\theta}\right) \qquad (4.1)$$

Here, β is the full width at half maxima of broadened peak, k (=0.9) is shape factor, λ (= 1.5406 Å) is X-Ray radiation (of CuKα) and θ is the Bragg's angle. The inter-planer distances (d_{hkl}) of the crystal are estimated as 3.34Å, 2.05Å, 1.75Å, 1.45Å, and 1.33Å from the Millar's planes at corresponding Bragg's respective angles accordingly. These distances are determined (enlisted in Table 4.1) for tetragonal $CuInSe_2$ by employing the equation:

Table 4.1: Value of inter planer spacing (d_{hkl}) and the crystallite size (D)

2θ	hkl	d_{hkl} (Å)	D value (nm)	Avg D (nm)
26.48	(1 1 2)	3.34	37.92	26.25
44.32	(2 0 4)	2.05	26.36	
52.48	(1 1 6)	1.75	23.14	
64.36	(4 0 0)	1.45	19.62	
70.58	(3 1 6)	1.33	24.22	

$$\frac{1}{d_{hkl}^2} = \frac{h^2+k^2}{a^2} + \frac{l^2}{c^2} \qquad (4.2)$$

Where a (= 5.782 **Å**) and c (= 11.61 **Å**) are lattice constants.

By considering logarithm in both hand sides of Eqn. 4.1, one can end up with the following extended Scherrer's equation[7]:

$$\ln \beta = \ln \frac{K\lambda}{D} + \ln\left(\frac{1}{\cos\theta}\right) \qquad (4.3)$$

It is possible to estimate the particle size more precisely from the intercept of fitted straight-line curve of lnβ vs ln(1/cosθ) (**Fig. 4.3**) drawn from the above equation. The precise estimated particle size is 33.4 nm. Both these analytical studies, result the particles are within proportion of nano (10 nm to 100 nm) in dimension.

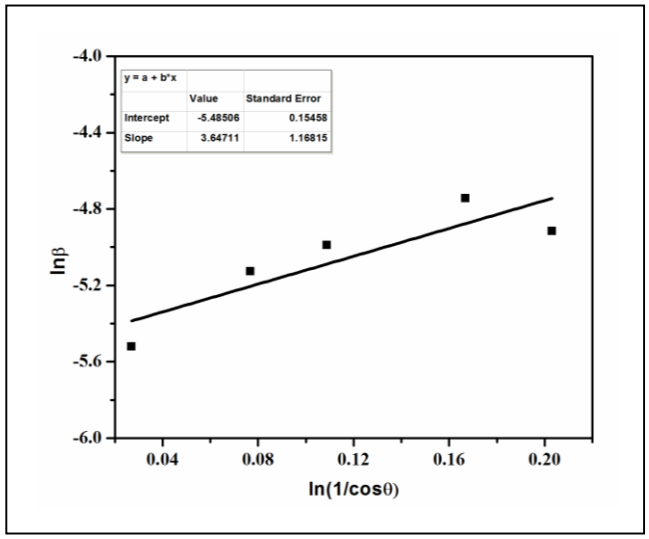

4.3.2. Electrical and optical analysis

The conductivity (at room temperature) of $CuInSe_2$ is determined as 1.1x 10^{-7} Scm^{-1} from Current-Voltage characteristic (**Fig. 4.4**(c)), recorded at bias voltage region 0 V to 1 V at 0.02

V interval by thin film technique. Using absorption data (inset of **Fig. 4.4**(d)) the optical band gap of the material is estimated by applying Tauc's equation:

$$(\alpha h\gamma) = A\sqrt{(h\gamma - E_g)} \qquad (4.4)$$

Where α is the absorption coefficient, h is Planck's constant, and ν is the frequency of incident photon. For direct transition, measuring the intercept of the extrapolated linear plot: $(\alpha h\gamma)^2$ vs. $(h\gamma)$, band gap is estimated as 1.47 eV (**Fig. 4.4** (d)). The value indicates that the synthesized material belongs to narrow bandgap semiconductors family.

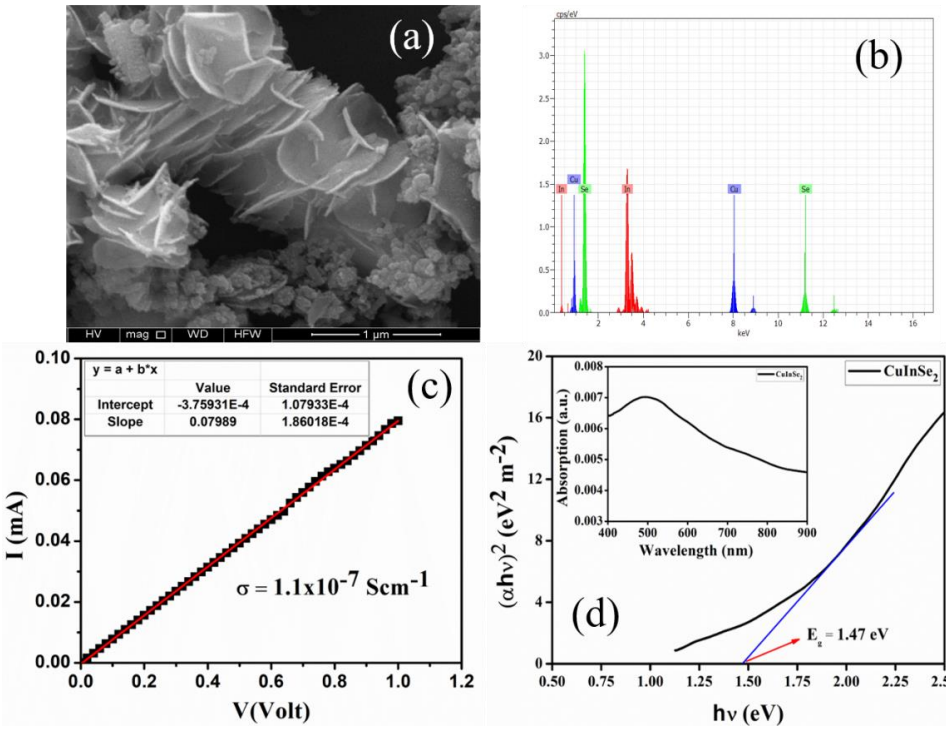

Fig. 4.4: (a) FESEM image**; (b)** EDAX of synthesized $CuInSe_2$; **(c)** I-V characteristic and **(d)** UV-vis spectra and Tauc's plot.

To determine band positions followed by the onset state of oxidation and reduction of the material, EC voltamogram (three-electrode) is implemented. **Fig. 4.5**(a) represents the EC curve, shows an oxidation peak (i.e. the ionization potential) at around +0.45 V and a reduction peak (i.e. electron affinity) at around -0.19 V. As the oxidation state corresponds to electron extraction from the HOMO level. The HOMO energy positions are estimated at -4.85 eV with the help of equation:

$$E_{HOMO} = -(E_{ox} + 4.4)\ eV \qquad (4.5)$$

where E_{ox} is the onset potentials of the oxidation relative to an Ag reference. Introducing band gap of material (1.47eV), E_{LUMO} is estimated as -3.38eV with the help of equation:

$$E_{LUMO} = E_{HOMO} + E_g \qquad (4.6)$$

The HOMO and LUMO level of P3HT reported at -4.76 eV and-2.74 eV having band gap energy 2.02 eV.[8] Thus the LUMO level of CIS (-3.38 eV) is energetically lower than that of LUMO of P3HT (-2.74 eV) **Fig. 4.5**(b)), approaches a high probability of transport of the photo-excited carrier electrons from P3HT to $CuInSe_2$ in order to achieve thermal stability. To analyze the resonance charge-transfer phenomena from P3HT to $CuInSe_2$, few compositions of composite (P3HT:$CuInSe_2$) are prepared at different weight ratio.

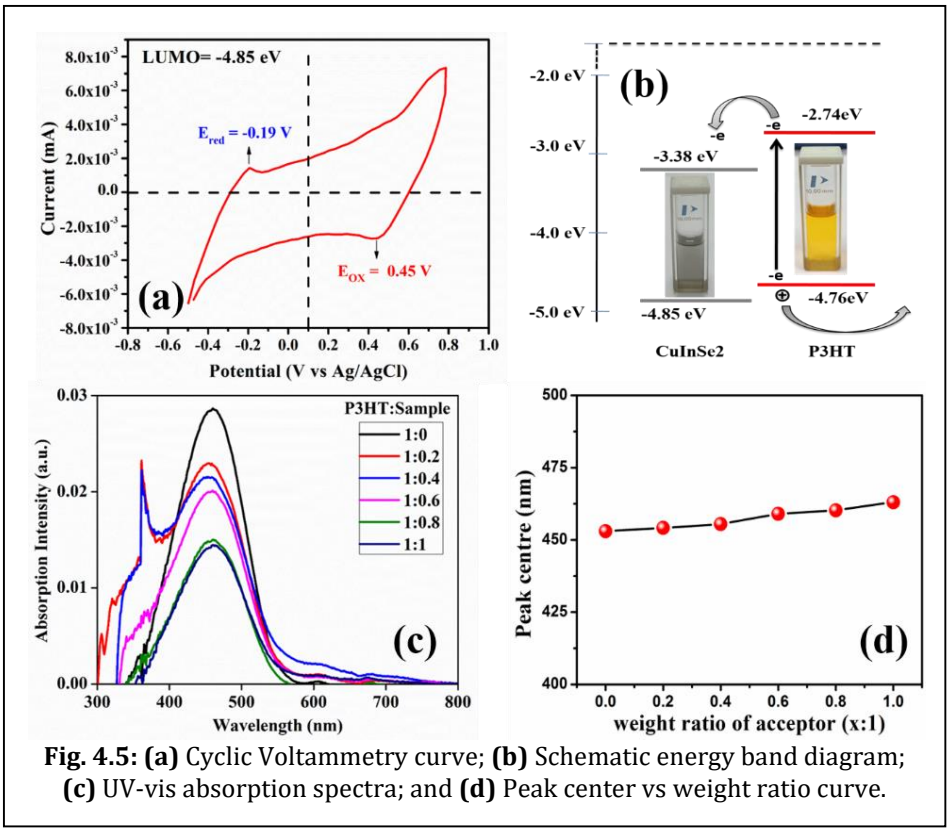

Fig. 4.5: (a) Cyclic Voltammetry curve; **(b)** Schematic energy band diagram; **(c)** UV-vis absorption spectra; and **(d)** Peak center vs weight ratio curve.

The UV-vis absorption spectra of P3HT:$CuInSe_2$ composites are recorded sequentially (**Fig. 4.5**(c)), which shows change in absorption spectra of the composite with increasing weight ratio of $CuInSe_2$. Absorption peak is found to be red shifted (**Fig. 4.5**(d)) with increase in weight concentration of acceptor. The systematic red shift in the absorption peaks indicates decrease in frequency and enhancement of photo reaction within donor and acceptor materials. **Fig. 4.6**(a), the Photoluminescence spectra, illustrates the emission intensity of steady state of donor, is decreased with addition of acceptor material by increasing weight concentration. These features ensure the energy quenching causes by electron transfer from donor (P3HT) to acceptor ($CuInSe_2$).

To get insight the state of quenching the PL-spectra are analyzed according to Stern–Volmer equation[5]:

$$\frac{F_0}{F} = 1 + K_{sv}[Q] \qquad (4.7)$$

where, F_0 and F are the emission intensity observed in absence and in presence of quencher, [Q] is quencher concentrations. The linearity of the Stern–Volmer plot(Fig.4.6(b)) with intercept nearly equal to unity indicates the static quenching phenomena. For ratification, the fluorescence data has also been analyzed with modified Stern–Volmer equation[6]:

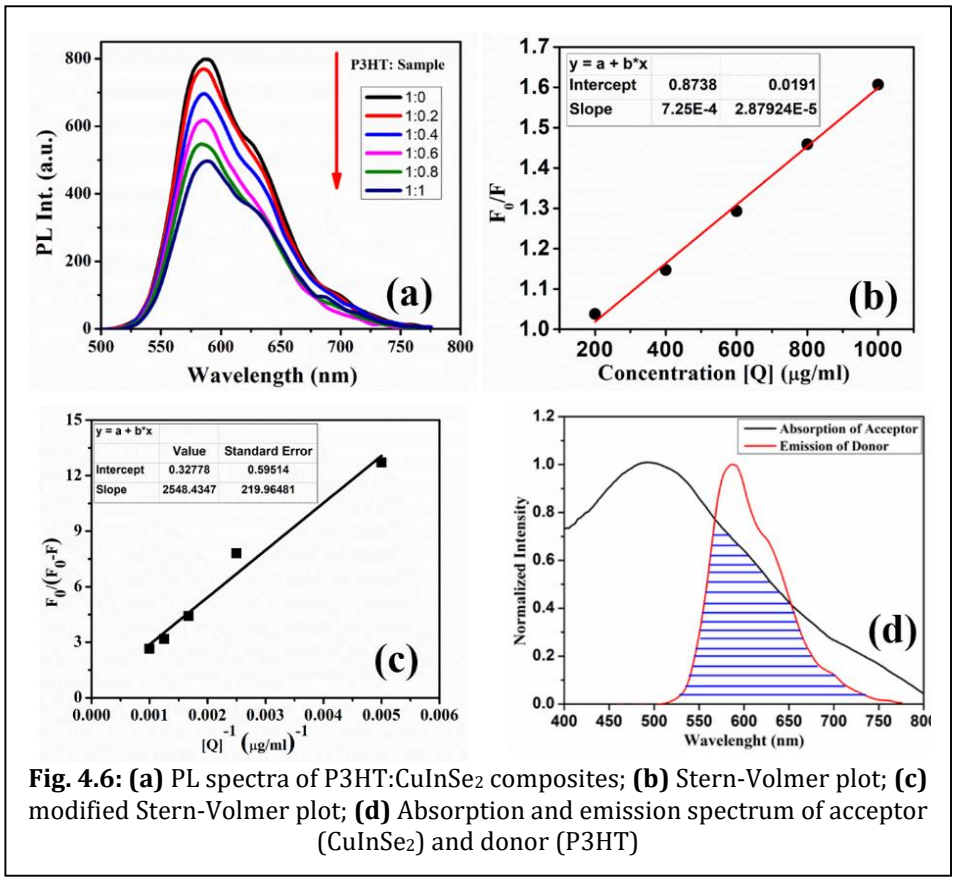

Fig. 4.6: (a) PL spectra of P3HT:$CuInSe_2$ composites; **(b)** Stern-Volmer plot; **(c)** modified Stern-Volmer plot; **(d)** Absorption and emission spectrum of acceptor ($CuInSe_2$) and donor (P3HT)

$$\frac{F_0}{F_0-F} = \frac{1}{f_a K_{sv}}\frac{1}{[Q]} + \frac{1}{f_a} \qquad (4.8)$$

The slope and intercept of plot of Fig. 4.6(c)attribute fraction of initial fluorescence (f_a) = 3.05andStern–Volmer quenching constant(K_{sv})=12.86 x 10^{-5} cm^3M^{-1}, which ensure the quenching is static in type.

Fig. 4.6(d) demonstrates considerable overlap between the absorption spectrum of CIS and the fluorescence spectrum of P3HT, assures the basis of FRET. For positive energy transfer between donor-acceptor, the Förster's distance (r) must be lesser than 8 nm.[6] This distance (r) is estimated by using Förster's equation of non-radiative energy transfer[5, 6]:

$$E = 1 - \frac{F}{F_0} = \frac{R_0^6}{(R_0^6 + r^6)} \qquad (4.9)$$

where, $R_0$is the critical energy transfer distance, at which 50% of the excitation energy is transferred to the acceptor.[5, 6]R_0 (=3.61nm) is determined from the equation:

$$R_0^6 = 8.79X10^{-25}\, k^2 m^{-4}\, \mathrm{J}\, \emptyset \qquad (4.10)$$

where, the orientation factor is $K^2 (= 2/3)$, m is refractive index of medium (considered as =1.522),[9] Ø is the fluorescence quantum yield of the donor, and J is the degree of spectral overlap between the donor's emission and the acceptor's absorption. J is related with fluorescence intensity of the fluorescent donor at wavelength (λ) i.e. F(λ) and the molar absorption coefficient of the acceptor at λ i.e. ε(λ) by the equation:

$$\mathbf{J} = \frac{[\sum \mathbf{F(\lambda)\varepsilon(\lambda)\lambda^4 \Delta\lambda}]}{[\sum \mathbf{F(\lambda)\Delta\lambda}]} \qquad (4.11)$$

The value of J is found to be 10.142 x 10^{-12} LM^{-1} cm^3 and fluorescence quantum yield (Ø) is determined as 0.128.

Here, the estimated 'r's are tabulated in **Table 4.2**. Interestingly, the conditions are fulfilled as r_{avg} (=4.71 nm) is less than 8 nm and within the range $0.5R_0 < r_{avg} < 1.5R_0$ (1.805 nm < r_{avg} < 5.415nm), which confirm every possibility of occurrence of energy transfer from P3HT (donor) to $CuInSe_2$ (acceptor). This analysis undoubtedly impacts upon the moderation in device grade by making use of this composite of optimum weight ratio in near future.

Table 4.2: Values of 'E' and 'r'

$E= 1-F/F_0$	(r/R_0)	r (nm)	r_{Avg} (nm)
0.378	1.0866	3.9268	4.7137
0.321	1.1331	4.0949	
0.226	1.2272	4.4349	
0.128	1.3762	4.9734	
0.089	1.4961	5.4067	
0.037	1.5069	5.4457	

4.4. Determination of Quantum Yield

The fluorescence quantum yield (Ø) is determined with the help of the following equation[10]:

$$\emptyset = \frac{I_F^X I_0^S - I_T^S n_X^2}{I_F^S I_0^X - I_T^X n_S^2} \emptyset_r \qquad (4.12)$$

Where I_F, I_T, I_o, and n are indications of fluorescence intensity, transmission intensity, transmission intensity of solvent and refractive index. S and X stand for P3HT and CIS

respectively. Quantum yield ($Ø_r$) of P3HT fluorescence in chlorobenzene solution is considered as 0.33 ± 0.07.[11]

4.5. Characterizations for FRET

Fluorescence energy transfer (FRET) is the transfer of the excited state energy of a donor (P3HT) to an acceptor ($CuInSe_2$) without the emission of light. The energy transfer can be considered as an energy exchange of an oscillating dipole to a dipole with similar resonance frequency.

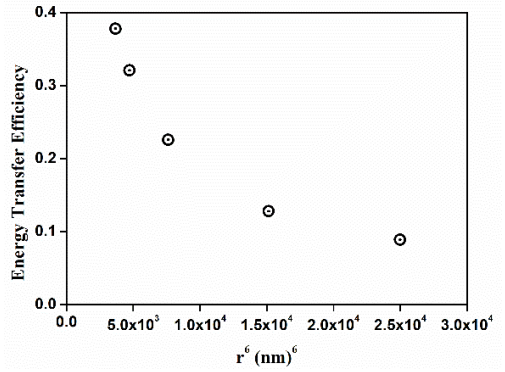

Fig. 4.7: Plot of energy transfer efficiency against

The energy transfer efficiency depends on the extent of the overlap of the emission spectrum of the donor with the absorption spectrum of the acceptor, the relative orientation of the donor and acceptor transition dipoles, and the distance r between donor and acceptor (within 8nm). Fig. 4.7 shows that the energy transfers efficiency decreases exponentially by r^6,[12] which reveals the fact of FRET.

4.6. Stokes shift

The absorption and emission spectra of P3HT (Donor) and the absorption spectra of $CuInSe_2$ (Acceptor) are presented in Fig. 4.8. The estimated stokes shifts for the donor is quite larger than the composite's which assisted technical possibility of resonance energy transfer within the composite rather self-absorption of Donor.[13]

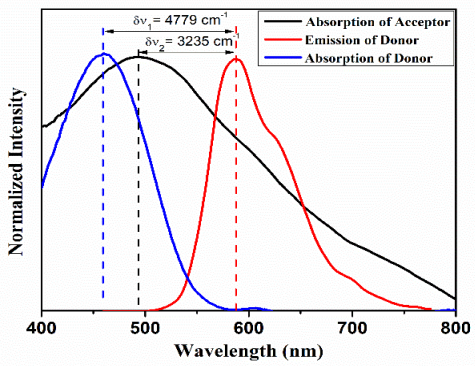

Fig. 4.8: Stokes shift for P3HT (Donor) is 4779 cm^{-1}

4.7. Conclusions

This is the first report of FRET analysis using composite P3HT:$CuInSe_2$, firmly establishes the successful energy quenching and resonance energy transfer from P3HT to $CuInSe_2$. The photo-induced charge transport phenomenon is explained with band diagram. In this art of work, solvothermally derived $CuInSe_2$ (conductivity 1.1×10^{-7} Scm^{-1} and band gap 1.47 eV) reveals its immense potential as an acceptor of excitons, excited from P3HT organic polymer. These thorough studies of absorption and emission highly ensure the possibility of resonance energy transfer within P3HT:$CuInSe_2$ followed by energy quenching technique.

References

1. M. Wang, S. K. Batabyal, Z. Li, D. Li, S. G. Mhaisalkar and Y. M. Lam, *RSC advances*, 2013, **3**, 9829-9834.
2. Y. Yang, H. Zhong, Z. Bai, B. Zou, Y. Li and G. D. Scholes, *The Journal of Physical Chemistry C*, 2012, **116**, 7280-7286.
3. J. G. Müller, E. Atas, C. Tan, K. S. Schanze and V. D. Kleiman, *Journal of the American Chemical Society*, 2006, **128**, 4007-4016.
4. A. Biswas, S. Sil, A. Dey, J. Datta, D. Das and P. P. Ray, *Journal of Physics and Chemistry of Solids*, 2021, **150**, 109878.
5. S. Patel and A. Datta, *The Journal of Physical Chemistry B*, 2007, **111**, 10557-10562.
6. Y.-J. Hu, Y. Liu, L.-X. Zhang, R.-M. Zhao and S.-S. Qu, *Journal of Molecular Structure*, 2005, **750**, 174-178.
7. A. Monshi, M. R. Foroughi and M. R. Monshi, *World journal of nano science and engineering*, 2012, **2**, 154-160.
8. A. Ergete, F. Sabir, Y. Li and T. Anshebo, *Journal of Photonics for Energy*, 2015, **5**, 057209.
9. J. N. Nayak, M. I. Aralaguppi and T. M. Aminabhavi, *Journal of Chemical & Engineering Data*, 2003, **48**, 628-631.
10. A. M. Brouwer, *Pure and Applied Chemistry*, 2011, **83**, 2213-2228.
11. S. Cook, A. Furube and R. Katoh, *Energy & Environmental Science*, 2008, **1**, 294-299.
12. S. Saini, H. Singh and B. Bagchi, *Journal of Chemical Sciences*, 2006, **118**, 23-35.
13. Z. Gao, Y. Hao, M. Zheng and Y. Chen, *Rsc Advances*, 2017, **7**, 7604-7609.

Chapter 5

Recognition of Light Sensing p-n Junction for Hetero-Structure $CuInSe_2/TiO_2$ and $CuInSe_2/HF\text{-}TiO_2$: Study of Carrier Transport Mechanism

Recognition of Light Sensing p-n Junction for Hetero-Structure $CuInSe_2/TiO_2$ and $CuInSe_2$/HF-TiO_2: Study of Carrier Transport Mechanism

Abstract

Searching of electronic system with functionality is the epitome of the material research and in this context nanomaterials $CuInSe_2$ and TiO_2 are the promising stars whose possible applications in electronic devices are just endless. However, the fabrication of junction based device using these two materials is most tantalizing prospect in material science is still at its rudimentary stage. In this letter, we report our recognition of current rectification behavior of $CuInSe_2/TiO_2$ hetero-junction, identical to the I-V characteristics of p-n junction diode and the impact of white light on it. The HOMO-LUMO band positions of hydrothermally derived $CuInSe_2$ and TiO_2 nanomaterials indicate that in thermal equilibrium a built-in-potential must arise across the junction. The current-rectification ratio of the configuration Al/$CuInSe_2/TiO_2$ /ITO is improved from 560 to 627 at voltage ±2 V on white light illumination and this kind of behavior is certainly offering us an unprecedented way to realize the $CuInSe_2/TiO_2$ hetero-junction as photo-sensing p-n diode. The device performance is improved further by replacing TiO_2 with HF treated TiO_2.

5.1. Introduction

The inorganic semiconductors and their derivatives have become popular over conventional organic semiconductors in designing p-n diodes and field-effect transistors.[1, 2] This has been made possible due to their easy fabrication, modulation capabilities, and low cost device characterization compared to organic semiconductors. However, the key limitation of the inorganic semiconductors is their insolubility.[3, 4] In this context, the formation of junction between two solid inorganic potential candidates is made to strike a balance device. With this background, in this present study we have fabricated a hetero-junction based device of configuration ITO/TiO_2/$CuInSe_2$/Al, using our derived $CuInSe_2$ and TiO_2 semiconductor nanomaterials,[5, 6] shows substantial response of incident light, which of course is the first example of its own kind.

There are lots of reports of p-n junction of hetero-structure by using inorganic nanomaterials.[7] This is the first approach to check potential applicability of TiO_2 and $CuInSe_2$in fabrication of p-n device. The current rectification at forward bias and the impact of incident light on the characteristic I-V as well as on the carrier transport mechanism of configuration of ITO/TiO_2/$CuInSe_2$/Al have been noticed. The carrier transport mechanism was demonstrated employing band theory. Estimated energy bands helped to realize the carrier transport and I-V characteristic. The impact of white light in performance was also studied. Likewise, the dynamical change in carrier transport behavior and the device performance was also investigated for ITO/HF-TiO_2/$CuInSe_2$/Al device.

5.2. Experimental

5.2.1. Device Fabrication

The synthesis and characterization of $CuInSe_2$, TiO_2 and HF treatment on later one are illustrated elsewhere.[5, 6] In prior to fabricate the device, the well dispersed solutions of the ready $CuInSe_2$, TiO_2 and HF-TiO_2 in the medium of ethanol were prepared. For its transparent conducting behavior, indium-tin-oxide (ITO) coated glass substrate was selected as the base material. In prior to making junction device of configuration of ITO/TiO_2/$CuInSe_2$/Al, firstly TiO_2 was deposited on ITO substrate by spin-coating (at 1200rpm) followed by drop cast technique. Then the film was dried at 80°C in vacuum. The uniformity of the film was checked

by tracing under light. After confirmation about film profile the dispersed solution of $CuInSe_2$ was coated onto the film by adopting spray pyrolysis method and was dried at 80°C inside a vacuum chamber. To get final configuration of ITO/TiO_2/$CuInSe_2$/Al, as front contact Aluminium was deposited by thermal evaporation technique with proper shadow mask. The schematic diagram of the device and its real image are shown in **Fig. 5.1**. In the same and simple manner another device ITO/HF-TiO_2/$CuInSe_2$/Al was fabricated by using HF-TiO_2 in place of TiO_2. The device characterization was performed by measuring I-V using Keithley 2635B SMU for both the devices. The carrier transport phenomenon was investigated from the I-V characteristic of the junction.

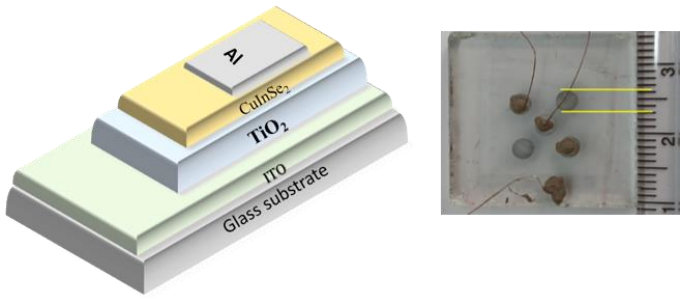

Fig. 5.1: Schematic presentation of device and its real image

5.3. Results and Discussion

5.3.1. Analysis of Cyclic Voltammetry for estimation of HOMO-LUMO

In the present work the LUMO energy levels of the synthesized TiO_2 and HF-TiO_2 are calculated using cyclic voltammetry (CV) measurement. Fig. 5.2 shows the CV plot of TiO_2 and HF treated TiO_2 nanoparticles. The CV graphs show no oxidation peak- i.e., the ionization potential- at positive potential region but only the reduction peaks – i.e., the electron affinity- at about -0.89 V and -0.36 V for TiO_2 and HF-TiO_2 respectively. In order to estimate the valence band (HOMO) and conduction band (LUMO) energy, the following equations were considered:

$E_{HOMO} = -(E_{ox} + 4.4)$ eV

and

$E_{LUMO} = -(E_{red} + 4.4)$ eV,

where E_{ox} and E_{red} are the onset potentials of the oxidation and reduction relative to an Ag reference electrode. The value 4.4 eV represents the difference between the vacuum level potential of the normal hydrogen electrode and the potential of the Ag/AgCl electrode.[8, 9]

Calculating the difference $\Delta E = E_{LUMO} - E_{HOMO}$, the band-gap energy was estimated. Since there is no oxidation peak in the positive region of the curve, so it is difficult to estimate the HOMO energy level for TiO_2 and HF-TiO_2 nanoparticles. In negative potential region the sharp reduction peaks are obtained as given in **Fig. 5.2**. From this plot the onset reduction potential E_{red} for both the materials are observed to measure the LUMO energy level. The LUMO levels for TiO_2 and HF-TiO_2 are -4.04 eV and -3.51 eV respectively. In optical characterization part using UV-Vis absorption data the band-gap of the materials was estimated. Using these band-gap energy 3.02 eV and 2.83 eV (reported elsewhere),[6] the HOMO levels were determined as -7.06 eV and -6.34 eV for TiO_2andHF-TiO_2 respectively.

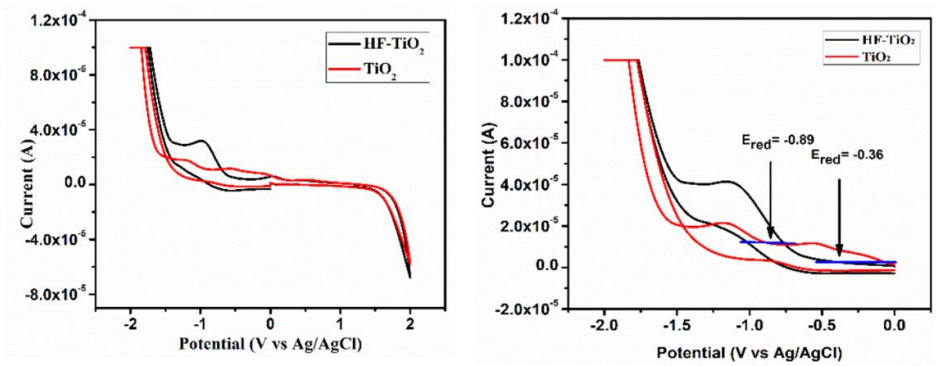

Fig. 5.2: C-V curves for TiO_2 and HF-TiO_2

Considering the onset oxidation and reduction potential for $CuInSe_2$ the LUMO and HOMO energy levels were estimated elsewhere.[5] The HOMO-LUMO energy levels for the above materials are tabulated in **Table-5.1.**

Table-5.1: HOMO-LUMO of derived materials.

Nanoparticles	*E_{red} (Volt)*	*HOMO (eV)*	*LUMO (eV)*	*Band-Gap E_g (eV)*
TiO_2	-0.89	-7.06	-4.04	3.02
HF-TiO_2	-0.36	-6.34	-3.51	2.83
$CuInSe_2$	-0.19	-4.85	-3.27	1.58

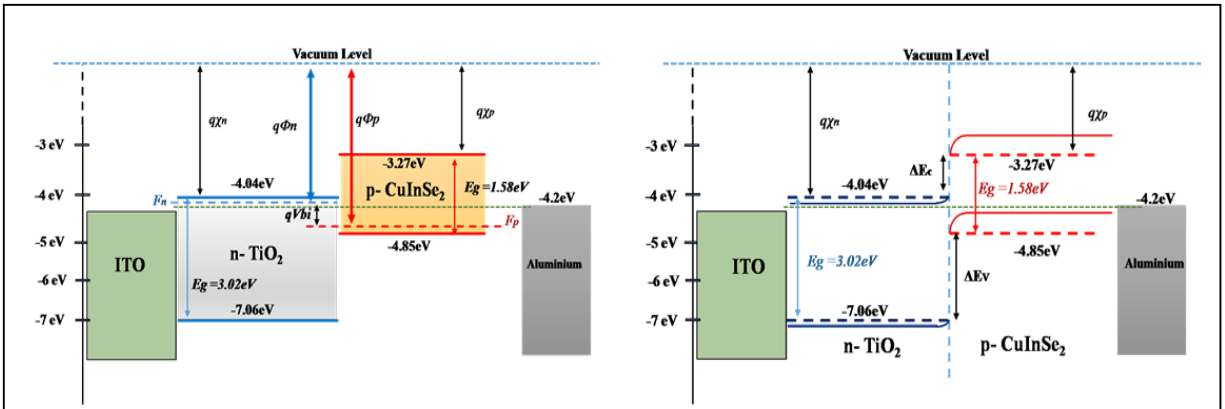

Fig. 5.3: Band diagram of Band diagram of ITO/TiO_2/$CuInSe_2$/Al before and after junction formation

Recent past, we reported elsewhere the potential applicability of hydrothermally derived $CuInSe_2$ in fabrication of Schottky device.[10] The derived TiO_2 and HF treated TiO_2 in our laboratory had also showed their potential behavior in Schottky device application.[6] In earlier reports the derived $CuInSe_2$ nanomaterial (band-gap =1.58eV) showed HOMO-LUMO energy levels at -4.85eV and -3.27 eV[5] and TiO_2nanomaterial (band-gap3.02eV)[6]bearing HOMO-LUMO energy positions at -7.06eV and -4.04eV. Theoretical possibility of formation of junction within ITO/TiO_2/$CuInSe_2$/Al configuration was revealed by the schematic band diagram (**Fig. 5.3**).

As the TiO_2 was being treated by HF, so the HOMO-LUMO positions are being shifted

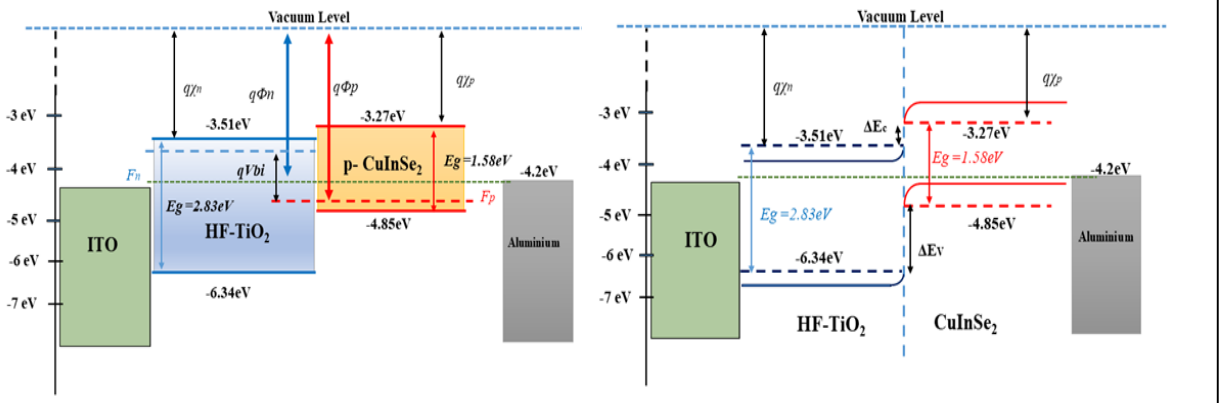

Fig. 5.4: Band diagram of Banddiagram of ITO/HF-TiO_2/$CuInSe_2$/Al before and after junction formation

to -6.34 eV and -3.51 eV with band-gap energy 2.83 eV in respect to untreated one. In probable band diagram **Fig. 5.4** exhibits ΔE_c = 0.24 eV and ΔE_v= 1.49 eV. The accumulation of carriers near to the fermi level after light soaking impacts upon these ΔE_c and ΔE_v which results on V_{bi} to reduce from 0.55 V to 0.49 V.

5.3.2. Estimation of dielectric constant

Fig. 5.5 represents the plot of capacitance against frequency at constant bias voltage for the films (a) $TiO_2/CuInSe_2$ and (b) $HF\text{-}TiO_2/CuInSe_2$. In higher frequency regimes the capacitance for both of the films were saturated, which was selected as the stable situation of the material film. Hence, the relative dielectric constant of the material film was evaluated by employing the following equation[10]:

$$\varepsilon_r = \frac{Cd}{\varepsilon_0 A}$$

Where ε_0 is the permittivity of free space, C is the capacitance (at saturation level), d is the thickness (supposed as ~1 μm) and A is the effective area (7.065×10^{-6} m^2) of the film. By utilising the formula mentioned above I have calculated the relative dielectric constant which was found to be 0.743 and 0.951 respectively.

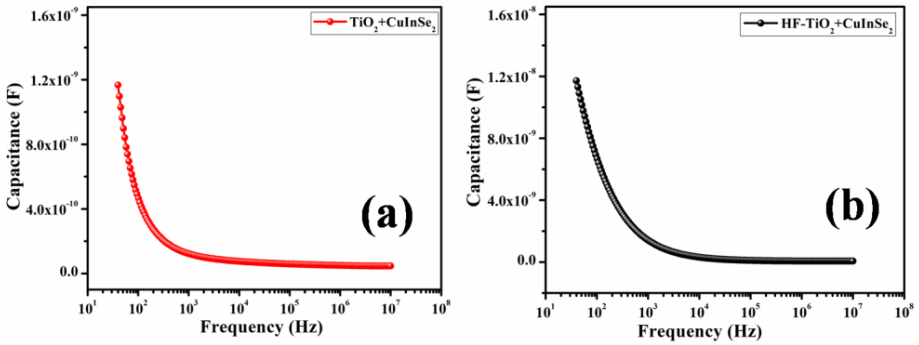

Fig. 5.5: Capacitance versus frequency plot for (a) $TiO_2/CuInSe_2$ and (b) HF-

5.3.3. Current - Voltage (I-V) analysis

Fig.5.6(a)represents the characteristic I-V of the device $ITO/TiO_2/CuInSe_2/Al$, exhibits outstanding rectifying behavior with rectification ratio 560 and 627 at bias voltage ±2V under dark and after light illumination.

To intervene into the mechanism, the I-V characteristics are analyzed by Shockley equation:

$$I = I_0\left[exp\left(\frac{qV}{nKT}\right) - 1\right] \qquad (5.1)$$

where, q is the charge of electron; n is ideality factor; V is the bias voltage; K is Boltzmann constant; T is temperature and I_0 is saturation current.

Now if bias voltage at room temperature, V> 3KT/q, i.e. 0.078 V then the equation (5.1) reduces to

$$I \approx I_0 \left[exp\left(\frac{qV}{nKT}\right)\right] \qquad (5.2)$$

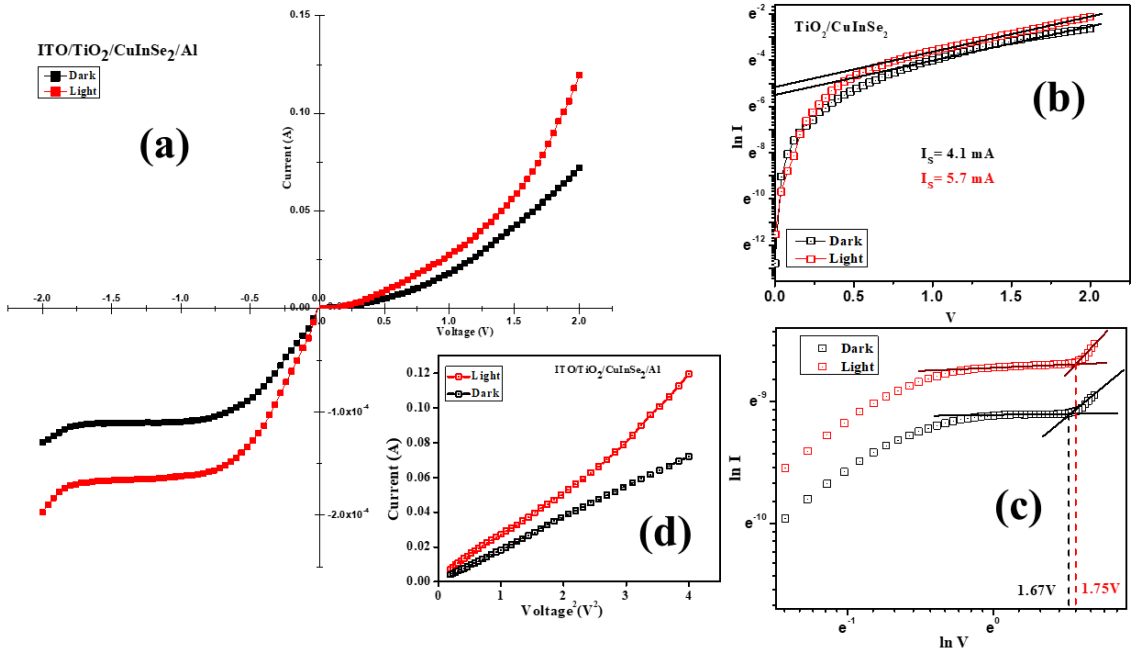

Fig. 5.6: (a) I-V curve for **ITO/TiO_2/$CuInSe_2$/Al** at dark and light; **(b)** lnI vs V curve in Forward bias; **(c)** lnI vs lnV plot in reverse bias; and **(d)** I vs V^2 plot of SCLC for dark and light.

In terms of natural log equation (5.2) reduces to

$$ln\, I = ln\, I_0 + \left(\frac{q}{nKT}\right) V \qquad (5.3)$$

Here 'n', was estimated as 1.5 for dark and 1.41 for light, from the slope of extrapolated linear part of ln I vs. V plot (Fig. 5.6(b)) employing equation (5.3). In case of ideal diode, n (value is 1) is indicative parameters of the interface uniformity. Here, n>1, indicates that there must be some interfacing layer, which deviates the device from its ideal behavior. The probability of electron-hole recombination within the depletion region also probably hinders the ideal behavior. Reduction of recombination rate upon incident light results intimate ideal behavior. The saturation current (dominated by diffusion of donor's major carriers) was estimated as 4.1 mA and 5.7 mA from the ln I vs. V plot (Fig. 5.6(b)) for dark and light respectively. Here the charge carrier density significantly increased upon light irradiance,

results on saturation current. The built in potential (V_{bi}) was reduced after light soaking from 0.51 V to 0.47 V and results on the growth of forward current (depends on the drift of charge carriers at $V>V_{bi}$). The increase in forward current after light soaking only can be demonstrated by SCLC theory. The V_{bi} can be definedby[11]:

$$V_{bi} = \frac{\Delta E_c - \Delta E_v}{2q} + \frac{KT}{q} ln\left(\frac{N_a N_d}{n_i^2}\right) \quad (5.4)$$

Where ΔE_c and ΔE_v are the change in conduction band energy and valence band energy respectively. N_a, N_d and n_i are the acceptor concentration, donor concentration and intrinsic carrier concentration at room-temperature sequentially. Here, V_{bi} was realized from the band diagram (Fig. 5.3). Fig. 5.3 exhibits ΔE_c = 0.77eV and ΔE_v= 2.21eV. The accumulation of carriers near to the fermi level after light soaking impacted upon these ΔE_c and ΔE_v which results on V_{bi} to reduce from 0.51V to 0.47 V. This built in potential would also be understood from the difference of fermi energy of donor and acceptor.[12] An obvious effect of light soaking on shifting of Fermi energy levels, results on V_{bi} for our device.

Fig. 5.6(c), represents the lnI- InV plot for reversed bias voltage, illustrates that the reverse breakdown voltage of the device is improved from 1.67V to 1.78V and the reverse saturation current (arises due to the diffusion of minor carriers of $CuInSe_2$) increases from $1.10x10^{-4}$A to $1.65x10^{-4}$A after light soaking.

To check the effect of incident light on SCLC, the effective carrier mobility (μ_{eff}) was estimatedas $2.32\times10^{-4}m^2V^{-1}S^{-1}$(dark) and $3.53\times10^{-4}m^2V^{-1}S^{-1}$ (light) from I vs V^2plot (Fig. 5.6(d)) for SCLC region by employing Mott-Gurney equation[10]:

$$I = \frac{9A\mu_{eff}\varepsilon_s}{8}\left(\frac{V^2}{d^3}\right) \quad (5.5)$$

Here, A is the effective area (≈ $7.07x10^{-6}$ m^2), d is the thickness (≈1μm) of junction materials, ε_s is the dielectric constant (estimated as 0.743) of the synthesized material. As the transit time (τ) and diffusion length (L_D) make one able to realize the efficient charge transport mechanism followed by carrier recombination, from the forward I–V plot for SCLC region, the transit time (τ) was determined by employing relation[10]:

$$\tau = \frac{9A\varepsilon}{8d}\left(\frac{V}{I}\right) \quad (5.6)$$

and in next approach, the diffusion length (L_D) was also estimated by the equation:

$$L_D = \sqrt{2D\tau} \quad (5.7)$$

where, diffusion coefficient (D) was determined from Einstein-Smoluchowski equation:

$$D = \frac{KT\mu_{eff}}{q} \qquad (5.8)$$

The results are tabulated in Table-5.2. It is important to note that the diffusion length and the transit time both decreased 14.5μm to 12.2μm and 17.62×10^{-10} seconds to 11.74×10^{-10}seconds after light soaking, which is the signature behavior of light response of the junction device. The performance of the device was realized from the product of μ and τ. The value of μτ after light soaking was also improved, which implies the potential behavior of the junction under light irradiance and henceforth this diode would have enough potentiality to be the candidate in application of solid state optoelectronic sensor.

Furthermore, to check the impact of HF treated TiO_2 on constraints of the device, are essential to characterize device grade, a hetero-structured configuration ITO/HF-TiO_2/$CuInSe_2$/Al was also fabricated and the charge transport behavior within device was analyzed in same manner.

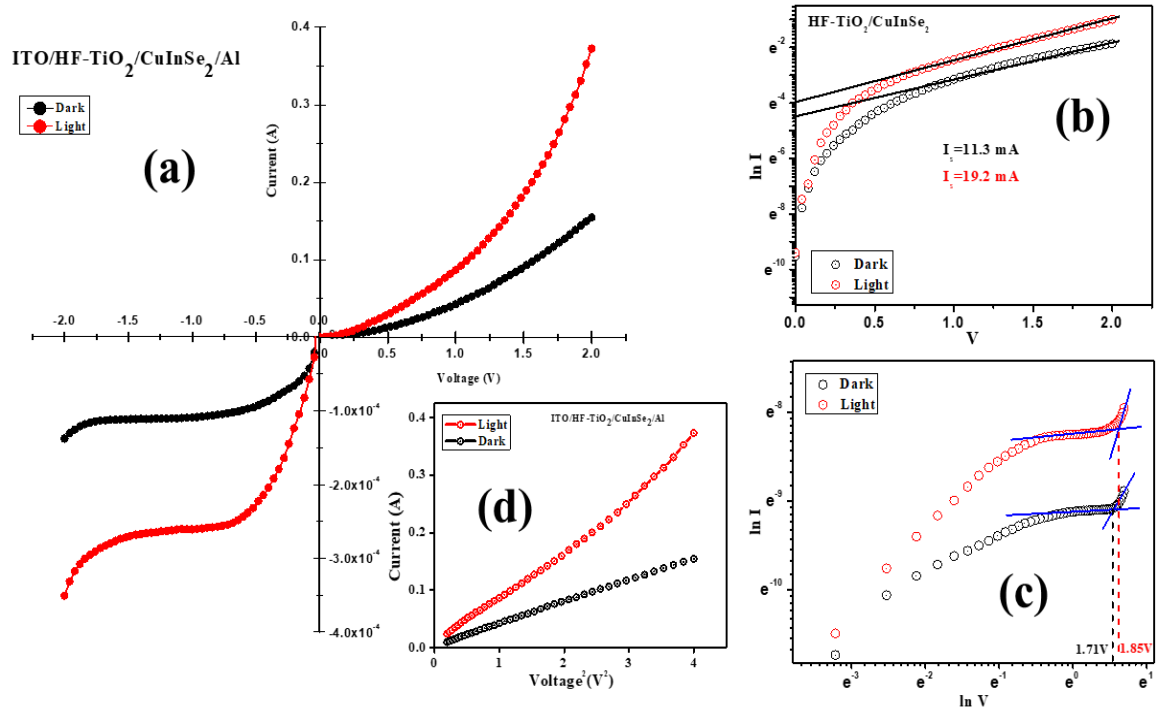

Fig. 5.7: (a) I-V characteristics curve for **ITO/HF-TiO_2/$CuInSe_2$/Al** at dark and light; **(b)** lnI vs V in Forward bias at dark and light; **(c)** lnI vs lnV in reverse bias for dark and light.

The experimental data are furnished in Fig. 5.7 and the carrier transport behavior was analyzed by employing the aforementioned equations. The results are tabulated in Table-5.2.

Table-5.2: Characteristic parameters of devices.

Parameters	ITO/TiO_2 /$CuInSe_2$ /Al		ITO/HF-TiO_2 /$CuInSe_2$ /Al	
	Dark	**Light**	**Dark**	**Light**
Rectification Ratio	560	627	1057	1107
Built-in Potential (V_{bi}) (V)	0.51	0.47	0.55	0.49
Reverse Saturation Current (I_{rs}) (A)	1.10×10^{-4}	1.65×10^{-4}	1.11×10^{-4}	2.67×10^{-4}
Cut-off voltage ($V_{Cut\text{-}off}$) (V)	1.67	1.78	1.71	1.85
Ideality Factor (n)	1.5	1.41	1.31	1.23
σ_{SCLC}(×10-3) (S/m)	7.89	14.14	16.53	43.01
μ_{eff} ($\times 10^{-4}$) ($m^2V^{-1}S^{-1}$)	2.32	3.53	4.8	10.99
τ ($\times 10^{-10}$) (S)	17.62	11.74	6.57	3.76
D ($\times 10^{-6}$)	5.98	6.44	12.38	28.35
L_D ($\times 10^{-7}$) (m)	1.45	1.22	1.27	1.46
$\mu\tau$ ($\times 10^{-14}$) ($m^3V^{-1}S^{-1}$)	40.87	41.44	31.53	41.32
Photosensitivity	1.65		2.41	

Results of Table-5.2 depict that the rectification ratio (improved from 1057 to 1107) as well as the forward current (improved from 11.3mA to 19.2mA) are improved than the earlier device. After HF treatment of TiO_2, the HOMO-LUMO levels are shifted to -6.34eV and -3.51 eV with band-gap2.83eV (Fig. 5.4). These shifting of bands have an obvious impact on built in potential as well as on the carrier transport phenomena. Here V_{bi} developed across hetero-junction is 0.55V, which decreased to 0.49Vafter light soaking. In reverse biased, the I_{rs}, and $V_{Cut\text{-}off}$ were significantly improved after light soaking than the prior one (Table-5.2). The parameters like, n, σ_{SCLC}, μ_{eff}, τ, D, L_D and $\mu\tau$, all were improved after light soaking. This

improvement, improves the device grade of the device make of HF treated TiO_2 in place of TiO_2.

In concern to the photo response of the junction devices, at constant bias voltage (at 2 V) the ratio of photo-current to dark-current was estimated as 1.65 and 2.41 for both the devices ITO/TiO_2/$CuInSe_2$/Al and ITO/HF-TiO_2/$CuInSe_2$/Al. This implies that the later device shows the better response upon light irradiance.

5.4. Conclusions

In conclusion, fabricated hetero-junctions TiO_2/$CuInSe_2$ and HF-TiO_2/$CuInSe_2$ show p-n junction behavior. The room temperature I-V measurement of the devices shows significant impact of incident white light on carrier transport mechanism and the overall performance of the devices. Meticulous computational investigations revealed that in compare to the first kind of device, the second one is more efficient towards the light response. Moreover, the devices under the influence of the light soaking, should offer us distinct current rectification and photosensitivity. The estimated diode parameters of ITO/TiO_2/$CuInSe_2$/Aland ITO/HF-TiO_2/$CuInSe_2$/Al structures are embracing the signature of the first kind of p-n junction acting as a photo-sensing device.

References

1. S. Ahmad, *Journal of Polymer Engineering*, 2014, **34**, 279-338.
2. J. Khan, R. T. M. Ahmad, J. Tan, R. Zhang, U. Khan and B. Liu, *SmartMat*, 2023, **4**, e1156.
3. M. Eslamian, *Nano-Micro Letters*, 2016, **9**, 3.
4. M. Liras and M. Barawi, *Chemical Society Reviews*, 2019, **48**, 5454-5487.
5. A. Biswas, B. Pal, M. Das, R. Sk, A. Layek and P. P. Ray, *Materials Letters*, 2023, **338**, 134066.
6. R. Sk, A. Biswas, A. Layek and P. P. Ray, *Chemical Physics*, 2024, **580**, 112233.
7. Y. Yang, Y. Liu, J. Wei, C. Pan, R. Xiong and J. Shi, *RSC Advances*, 2014, **4**, 31941-31947.
8. E. Kucur, J. Riegler, G. A. Urban and T. Nann, *The Journal of chemical physics*, 2003, **119**, 2333-2337.
9. K. G. Deepa and J. Nagaraju, *Materials Science and Engineering: B*, 2012, **177**, 1023-1028.
10. A. Biswas, S. Sil, A. Dey, J. Datta, D. Das and P. P. Ray, *Journal of Physics and Chemistry of Solids*, 2021, **150**, 109878.
11. B. Gupta, A. Jain and R. Mehra, *Journal of Materials Science & Technology*, 2010, **26**, 223-227.
12. H. Kroemer, *Surface Science*, 1983, **132**, 543-576.

Chapter 6

Effect of size of CdO on bias dependent conduction and relaxation mechanism by means of Impedance Spectroscopy: Experimental and Theoretical Studies

Effect of size of CdO on bias dependent conduction and relaxation mechanism by means of Impedance Spectroscopy: Experimental and Theoretical Studies

Abstract

In this report, the morphological impact of hydrothermally derived CdO on charge conduction and relaxations investigated by using bias-dependent impedance spectroscopy (IS). The work of art is the findings of the impact of grain and grain boundaries of CdO on the frequency-dependent electric conductivity and relaxation mechanism followed by the crystallite size. In this regard, two different crystallite size based CdOs are derived from hydrothermal route at different temperatures. Materials are characterized by XRD, FESEM, UV-vis absorption spectra. The dc conductivity is also evaluated by measuring current-voltage characteristics, and bias-dependent Impedance Spectroscopy at room temperature, which spectacles the CdO with larger crystallite size dominate the conduction mechanism.

6.1. Introduction

Metal-oxide inorganic nanoparticles present great scientific and technological values in fabricating frequency-controlled portable electronic devices mostly due to their unique physical and chemical features deriving from their nanoscale size and morphology. In the recent trend, researchers have focused on II-VI cadmium oxide (CdO) semiconductor transition metal oxide, which includes narrow direct band gaps of 2.2eV to 2.5eV.To study their size and morphology dependent behavior as well as potential applications in several areas of research, specifically in optoelectronics[1] and other applications including solar cells,[2-4] photodiodes,[5-7] transparent electrodes[8, 9] and gas sensors[10-12]. Due to its versatile dynamic behavior, there have been few efforts to prepare CdO nanoparticles by tailoring various synthesis techniques such as chemical bath deposition,[13-15] electrodeposition,[16-18] chemical spray pyrolysis.[19-21] solvothermal technique,[22, 23] etc. These methods usually involve various expensive arrangements and procurement, otherwise poor yield. The hydrothermal method adopted in this study is very simple and cost-effective than the other conventional methods and an effective route for industrial use.

Impedance spectroscopy (IS) is a popular method to realize the conduction mechanism and relaxation behavior of the grain and grain boundary in a material. Charge transport behavior through the grain and grain boundary of semiconducting material influences the carrier relaxation due to the presence of micro-structural barrier formation by grain boundary between two adjacent grains[24]. This charge transport behavior and relaxation nature can be investigated using various electrical properties like impedance, electrical modulus of semiconducting material. These properties can be investigated using IS and play an essential role in the applications of high-frequency control devices and potential difference dependent resistors.[25, 26]

There are several works where the temperature-dependent impedance behavior of CdO has been investigated and reported by researchers.[27-31] At the same time, the study of the morphological impact of CdO on bias-dependent impedance and relaxation behavior isin the empirical stage. In this report, two different types of CdO, synthesized by hydrothermal technique at 500^0C temperature treatment, labeled as S(1) and at 600^0C temperature treatment, marked as S(2) respectively. The structural characterization approved their

uniqueness with crystallite size. To find out the unique impact of morphology on its electric behavior, we have performed electrical characterization. The electrical characterization reveals its structure-dependent conducting behavior. The theoretical overview and its practical implications of the crystallites size upon the conduction constraints are investigated in this report. The occurrence of grain size and grain boundaries, depending upon the size and architecture of the crystallites of the material highly influences the electrical conductivity which is studied in depth further. To examine the variation of electrical impedance, relaxation, ac conductivity of the materials with the variation of frequency, we have fabricated two thin films by using the spin coating technique, and its frequency-dependent impedance is measured under an applied electric field. The appropriate equivalent circuits are designed to analyze Nyquist plots derived using the EIS spectrum analyzer. The main objective is to examine the effect of morphology on bias-dependent Debye relaxation and conduction mechanism of grain and grain boundary by using synthesized CdOs. A better understanding and intervention may insist us for future use of CdO in applications as a signal transport circuit element.

6.2. Experimental details

6.2.1. Materials

($Cd(CH_3COO)_2.2H_2O$) and NH_4OH of analytical grade is purchased from Merck and is used without further purification.

6.2.2. Synthesis

In the typical synthesis, 200 ml 0.5M cadmium acetate aqueous solution is prepared and separated in two different beakers in equal proportion. The ammonium solution is added dropwise to the above solutions individually (till pH = 7) with constant stirring. Brownish solutions are obtained in both cases and are followed by stirring for 24 hours. After that, we have heated the solutions overnight at 500°C (labeled as S(1)) and 600°C (marked as S(2)) under Teflon Lined hydrothermal Autoclave. The precipitates are collected through rinsing several times with distilled water by centrifuge technique. Finally, the powders are collected after annealing at 100°C for 4 hours each.

6.2.3. Thin film fabrication

Thin films of the sample are fabricated on Indium Tin Oxide (ITO) coated glass substrate by spin coating technique. In this regards a dispersed solution is prepared in ethanol by rigorous sonication for half an hour.

6.2.4. Material Characterization

To determine the crystal structure of the materials powder X-Ray Diffraction (PXRD) technique is adopted well. In this process, the diffraction patterns are recorded with the help of Bruker make D8 powder X-ray Diffractometer. FEI made Inspect F-50 scanning electron microscope is used to record the FESEM images. Shimadzu 2401 PC UV-vis spectrophotometer makes use for optical characterization of the sample. This part of characterization is carried out by preparing a dispersed solution of the sample in ethanol by ultra-sonication technique. Agilent 4294A LCR meter recorded the impedance spectroscopy of the sample films in the frequency region of 40Hz-5MHz under the bias voltage of 0mV to 1000mV at constant oscillatory voltage 50mV at ambient conditions. Conductivity at room-temperature is derived from the current-voltage characteristics curve recorded by using two-probe technique. The current-voltage (I-V) characteristics of thin film of samples are recorded with the help of Keithley 2400 SMU by applying voltage from 0V to 1.0V at interval 0.1V. By measuring the dimensions of active contact area A(=7.065×10^{-6} m^2); the thickness of the film d(=1μm) (are measured with the help of surface profiler) and the slope of the characteristic curve, conductivity of the sample films are estimated.

6.3. Results and Discussions

Fig. 6.1 indicates the X-Ray diffraction spectra of the materials S(1) and S(2). The responsible Bragg's planes (111), (200), (220), (311) and (222)are sharply observed at Bragg's angle 2θ = 33.2, 38.5, 56.1, 67.0 and 70.5 degree respectively. These responsible planes with respective Bragg's angle refer to cubical (lattice parameter a=4.6953Å) phase of CdO, justified by JCPDS card no:05-0640.[32-34]The inter-planar distances at angle 2θ = 33.2, 38.5, 56.1, 67.0 and 70.5 degree are estimated as (d_{111} = 2.7108A), (d_{200} = 2.3477A), (d_{220} = 1.66A), (d_{311} =1.4157A) and (d_{222} =1.3554A) (Table – 6.1).

Table – 6.1: Texture coefficients and Interplaner distances of CdO

For CdO: (a=4.6953Å)

2θ	(h k l)	$d_{hkl} = \frac{a}{\sqrt{h^2+k^2+l^2}}$Å	Texture Coefficient S(1)	Texture Coefficient S(2)
33.2	(1 1 1)	2.7108	0.8296	1.0004
38.5	(2 0 0)	2.3477	0.7737	0.9456
56.1	(2 2 0)	1.6600	1.0720	1.0013
67.0	(3 1 1)	1.4157	1.1149	1.0082
70.5	(2 2 2)	1.3554	1.2097	1.0444

The planes (001), (100), (101), and (102)are evenly observed at Bragg's angle 2θ = 23.5, 30.3, 36.2 and 49.7 degree respectively, imply the occurrence of hexagonal (lattice parameters a=3.4947Å and c= 4.7106Å) $Cd(OH)_2$ as admixture (supported by JCPDS card no.: 31-0228). The inter-planar distances of $Cd(OH)_2$ at angle 2θ = 23.5, 30.3, 36.2, and 49.7 degree are determined as (d_{001} = 2.7108A), (d_{100} = 2.3477A), (d_{101} = 1.66A) and (d_{102} =1.4157A) (Table – 6.2). This mild impurity of $Cd(OH)_2$ is arising mostly due to the incomplete combustion under autoclave. The intensity of the peaks assists that most of the

Table – 6.2: Texture coefficients and Interplaner distances of $Cd(OH)_2$

For $Cd(OH)_2$: (a=3.4947Å and c= 4.7106Å)

2θ	(h k l)	$d_{hkl} = \frac{1}{\sqrt{\frac{4}{3}\left(\frac{h^2+hk+k^2}{a^2}\right)+\frac{l^2}{c^2}}}$ Å	Texture Coefficient S(1)	Texture Coefficient S(2)
23.5	(0 0 1)	2.7108	1.2598	1.2596
30.3	(1 0 0)	2.3477	1.2369	1.3641
36.2	(1 0 1)	1.660	0.6442	0.5515
49.7	(1 0 2)	1.4157	0.8589	0.8247

diffraction are highly obtained from Bragg's planes of CdO. Typically, the full width at half maxima of the intense pattern is highly depends on the size of crystallites and is the subject of Williumson-Hall plot.

The typical size of crystallites 65 nm for S(1), 83 nm for S(2), with the lattice strain 3.5×10^{-3} of S(1), 5.1×10^{-3} of S(2) are estimated, by considering the significant peaks of X-Ray diffraction pattern arise from CdO, with the help of Williamson Hall's (W-H) plot(Fig. 6.2) by measuring the intercept and slope fitted with the equation (Eq. 6.1)[35, 36]:

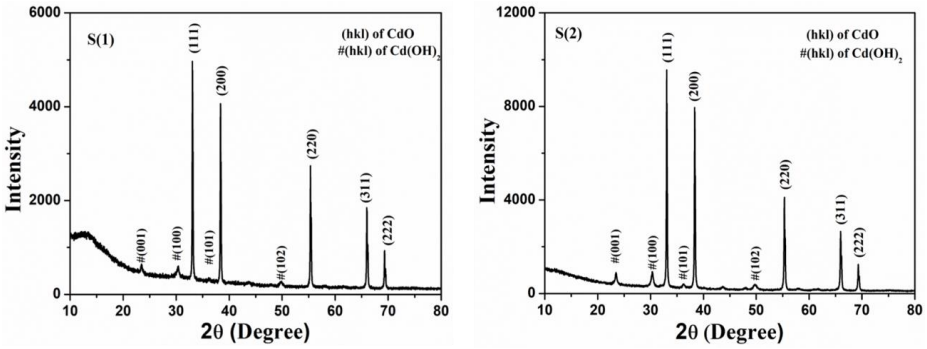

Fig. 6.1: X-Ray Diffraction spectra of the S(1) and S(2).

$$B_r \cos\theta = \frac{K\lambda}{D} + \mu \sin\theta \qquad (6.1)$$

Where crystallite size is indicated as D, the shape factor is K(=0.9),**λ**= 0.15406nm is the wavelength of the monochromatic X-Ray beam (for $CuK_{\alpha1}$ radiation), the full width at half-maximum of diffraction peak is represented by B_r, μ is lattice strain, i.e., a quantitative measure of dislocations and crystal defects arises by lattice expansion,[37] and θ is Bragg's diffraction angle.

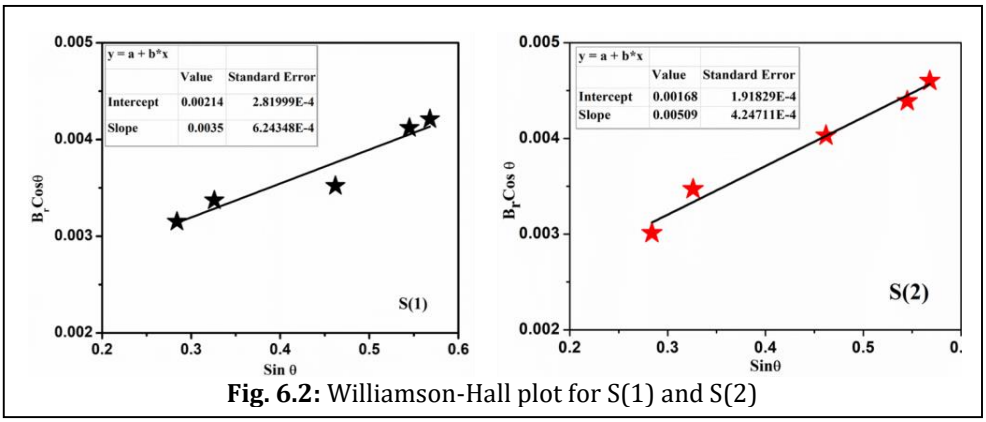

Fig. 6.2: Williamson-Hall plot for S(1) and S(2)

To obtain the detail orientation of material grains, the interplaner distances(d_{hkl}) and the texture coefficient (TC) of Miller's planes are estimated by measuring the intensity ratio of diffraction pattern (I) and the standard one (I_0) derived from JCPDS data for each responsible planes (Table – 6.1 and Table – 6.2). An increase (decrease) from the unity in the texture coefficient indicates a higher (lower) degree of preferred orientation along a particular plane of the film. The deviation in the texture coefficient from unity for a

particular Miller plane also corresponds to change in atomic densities corresponding to that plane as X-ray intensities are function of atomic structure factors.Thus, higher (lower) value of TC actually corresponds to increase (decrease) in planar density along a particular crystal plane as compared to ideal values. The texture coefficients for the Millar plane (111) and (200) of sample S(2) is nearly unity whereas, for sample S(1) the values are quite less than unity. Hence, the planar density for (111) and (200)of S(2) is much higher than S(1).The TCis quite deviatedfrom one for S(1) incorrespond to the rest Millar planes (220), (311), and (222). But for S(2) TC values for the planes (220), (311), and (222) are nearly one.

Fig. 6.3 illustrates the SEM (scanning electron microscopy) images of the synthesized materials which clearly indicates that the particles are quite like micro (0.1μm to 0.2μm) in dimension but are mostly agglomerated. The variation of the size of the crystallites follows the results which are depicted from the W-H plot in XRD analysis. Agglomeration arises mostly due to rapid grain growth during calcination at high-temperature.[38]

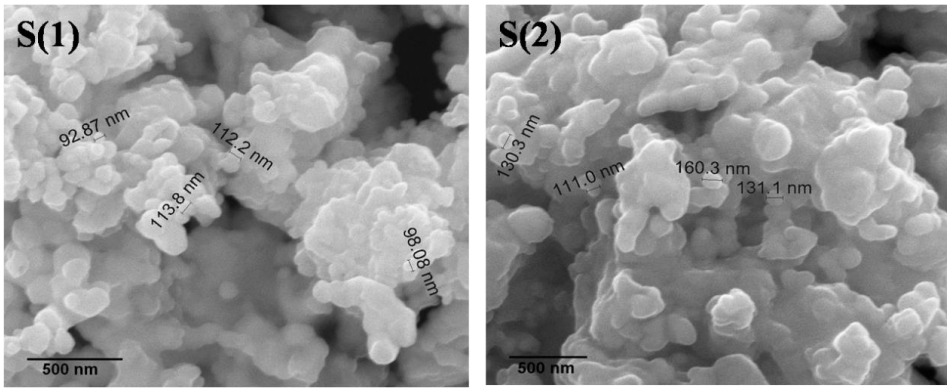

Fig. 6.3: SEM image of the synthesized materials S(1) and S(2)

The typical surface-to-volume ratio of the grain, rightly influences the absorption ability specially, within the vicinity of nano or nano-like dimension. To get better insight of the materials, the absorption data is recorded for the samples S(1) and S(2) in solution mode. Inset of Fig. 6.4 represents UV-vis absorption spectrums within the wavelength ranges from 300 nm to 1000 nm for samples respectively. To better comprehend the absorption ability quantitatively, the absorbance data of the samples are best fitted to Tauc's equation (Eq. 6.2). The optical band gap energy for S(1) as 2.19eV, and S(2) as 2.32eVarederived for direct transition with the help of intercept of the extrapolated linear part of the plot $(\alpha h\gamma)^2$ vs. $(h\gamma)$ (Fig. 6.4) using the equation (Eq. 6.2):

$$(\alpha h\gamma) = A\sqrt{(h\gamma - E_g)} \qquad (6.2)$$

Where $h\gamma$ indicates the energy of the incident photon, E_g is bandgap energy, α is the absorption coefficient (which is determined from the absorption data, using Beer's equation (Eq. 6.3)):

$$\alpha = \frac{\ln\left(\frac{1}{T}\right)}{d} \qquad (6.3)$$

Where d (=10 mm) represents the thickness of the cuvette and 1/T is the absorbance, and A (= 0.9) is a constant factor. The results are pretty evident as per the nature of crystallite size. This deviation in bandgap energy for the samples occurs due to the population of energy states next to the conduction band depending on the crystal growth engineering, which is assisted by ambient temperature, vapor pressure, etc. during nucleation.

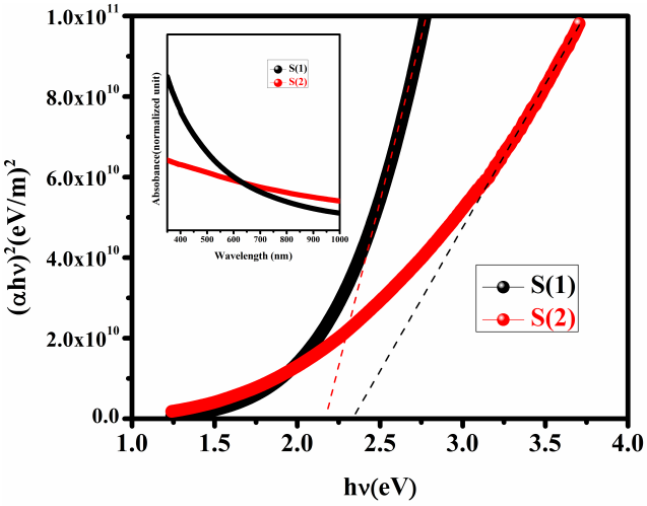

Fig. 6.4: UV-vis absorption spectra (Inset) and Tauc's

Fig. 6.5 depicts the current-voltage (I-V) behavior of the films under dark at room

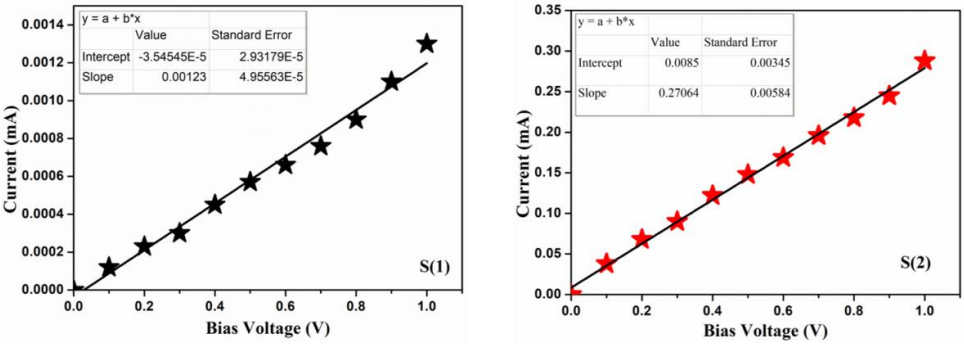

Fig. 6.5: I-V characteristics of S(1) and S(2)

temperature. The room temperature dc conductivity of the material films is estimated as 2.7×10^{-7} Sm^{-1} and 6.4×10^{-5} Sm^{-1}. The order of room temperature conductivity approves the samples to belong with the semiconductor ($10^{-6}$to 10^{4} Sm^{-1}) group. Noteworthy, imperative

thing is that the conductivity of S(2), which is merely237 times of S(1). In general, the increment of conductivity may occur due to the accumulation of the charge carriers near the Fermi level. The synthesis route greatly impacts the crystal growth as well as the occurrence of accumulation of grains. This amendment in carrier concentration influenced the bandgap energy of the synthesized materials accordingly. The consistent value of estimated energy bandgap of the synthesized materials illustrates this obvious fact.

To get better insight in the influence of grain and grain boundaries on conduction mechanism as well as on AC conductivity, the bias voltage dependent impedance behavior of the samples has been studied. The variation of the real part of impedance (Z′) with the frequency illustrates a basic idea about the conduction behavior of a material in the presence of an external field (thermal or electrical).The variation of the imaginary part of the impedance (Z″) with the frequency illustrates the mechanism behind the bias-dependent conduction and relaxation.

Here, Fig. 6.6 illustrates the Z′ versus f plot for the samples S(1) and S(2) as recorded. It has been observed that more than one frequency-dependent and frequency-independent region are perceptible as the bias voltage varies from 0 mV to 1000 mV for both the samples. Among them, S(1) exhibits a frequency independent part at low frequency (40Hz to 100KHz) as well as at high frequency (1MHz to 5MHz) and also a dispersive frequency-dependent part in between this high and low-frequency regime (100KHz to 1MHz). Whereas, S(2) shows only one frequency-independent region at low frequency (40Hz to 100KHz) and the dispersive part

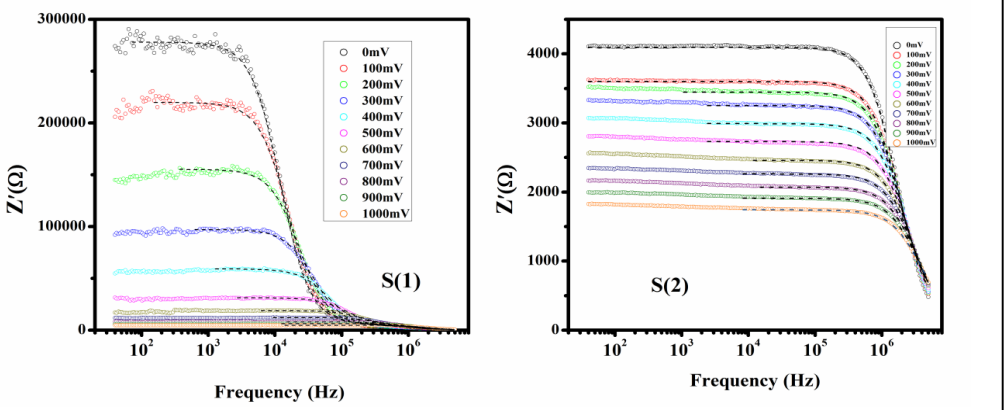

Fig. 6.6: Z′ versus frequency at different bias voltage for S(1) and S(2) (Best fitted lines are denoted by dashed lines)

at higher frequency (100KHz to 5MHz).In general, the frequency independent part at low-frequency results from the long-range movement of the charge carrier.[39] During the long-range movement, the charge carrier hops successfully to the neighbor particles which are relaxing at their site. On the other hand, the localized or short-range movements are responsible for the unsuccessful hopping of charge carriers by relaxing to their site.[39] The samples show these two regions with a different frequency span for the entire applied bias voltage. The higher crystallite size of S(2) prefers lower grain boundary which causes a depreciation of interfacial polarization and decreases the impedance value than S(1) at a certain bias voltage. At low frequency, during the long-range movement, the interfacial charge carrier follows the applied ac electric field and provides an excess capacitance that depends on frequency. Therefore, it is observed that the typical frequency, responsible for the makeover from an independent region to the dispersive part, shifts to a higher frequency for both the samples as the bias voltage decreases. S(1) emphasizes one more area at a higher frequency at which all the Z′ curves seem to merge into one curve and overcome the bias dependency. This phenomenon occurs due to the accumulated space charge carriers near the phase boundary, where those charge carriers pass through the barrier with sufficient energy. It results an increment in conductivity with a diminish of impedance.[40]

Fig. 6.7, represents the Z″ versus frequency curve for the bias voltage of 0 mV to 1000 mV for S(1) and S(2) respectively. Several significant characteristics have been observed in these curves. Every Z″ spectra contains a peak at a certain frequency under the different bias voltages. These characteristic peaks reveal the type and strength of electrical relaxation in the sample.[41] The intensity of the peaks is decreased and shifted to the higher frequency as the bias voltage enhances for both. The gradual lowering value of Z″ with the increment of bias voltage may be due to enhancement of conductivity. Moreover, the peaks move to the higher frequency due to increase in bias voltage. At different bias voltage, for S(1), the relaxation process is dominated by the accumulation of space charges at the grain boundary and the peaks appear at low frequency. However, the higher bias voltages reduce the space charge polarization near the grain boundary and make them comfortable to relax and recombine within the grain interior.[40]

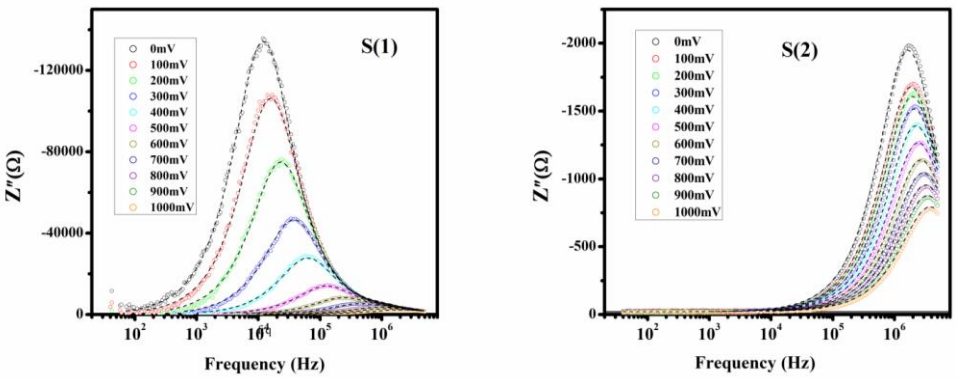

Fig. 6.7: Variation in Z″ with frequency at different bias voltage for S(1) and S(2) (Best fitted lines are denoted by dashed lines)

Here, the characteristic peaks of S(2) exhibit lower Z_{max}'' and shift to higher frequency than S(1) under the different bias voltage. The greater grain size of S(2) assists more to reduce the polarization between two grains which is responsible for the shifting of characteristic peaks towards the higher frequency. A complete distribution of Z″spectra for S(1) which is not visible for the other sample S(2) in the experimental frequency regime, has been obtained. At the higher frequency, the merging of Z″ curve generally happens due to the settling down of space charges in the material. The relaxation mechanism of S(1) has been taken place in the intermediate frequency region for every bias voltage. Whereas, this mechanism of S(2)has occurred at very high frequency, and the merging of all Z″ curves for this sample are not obtained.

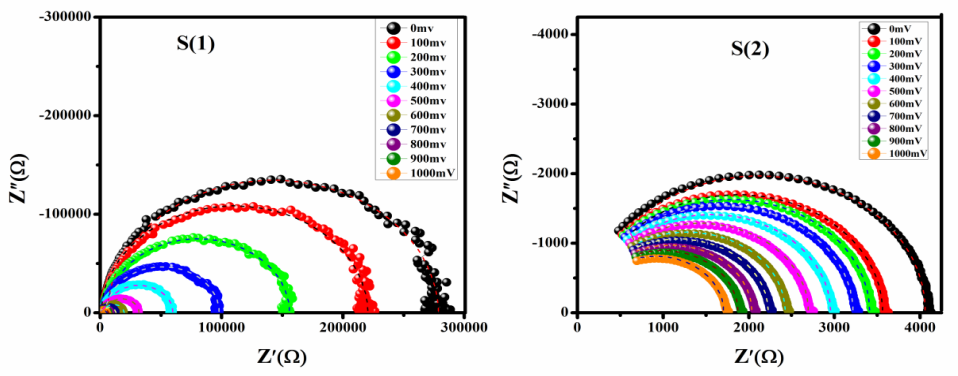

Fig. 6.8: Nyquist plots of S(1) and S(2) at different bias voltage (The dotted lines denote the fitted curve using the equivalent circuit.)

Fig. 6.8 demonstrates the Nyquist plots (Z″ versus Z′) at the bias voltage of 0 mV to 1000 mV. In general, the Nyquist plot of material is patterned as a semicircular. Its shape contains information about the evolutionary impact of grain and grain boundary due to the effect of the external field.[42] The interception of the semicircle at the positive x-axis demonstrates the total

resistance of the material at a certain condition. It is noteworthy that the total resistance of S(2) is found to be lesser than S(1) for each bias voltage which indicates the better conduction of S(2). In most cases, the grain and grain boundary bears individual semicircles at the high and low-frequency region, respectively. In this case, both samples exhibit a merged and single semicircle which may be the result of the overlapping of those individual semicircles for grain and grain boundary.[42] Therefore, we have taken the assistance of an ac equivalent circuit (Fig. 6.9) and fitted it to the Nyquist plots obtained experimentally.

We have visualized the involvement of grain and grain boundary of the synthesized material under the applied bias voltage. Generally, the semicircular arc of the Nyquist plot can be interpreted by RC parallel circuit element[42]. Here, the centers of the arcs (Nyquist plot) are displaced below the Z′ axis for which the experimental arcs of our materials are fitted with resistance and constant phase element (CPE) rather than resistance and capacitance. Therefore, C_g and C_{gb} are substituted by CPE_g and CPE_{gb}. Therefore, the impedance can be written as

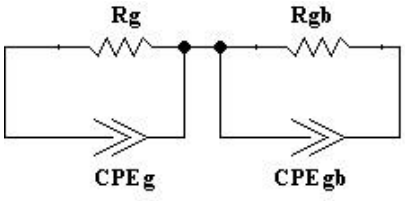

Fig. 6.9: ac Equivalent Circuit

$$Z^* = \frac{R_g}{1+R_gQ_g(jw)^{n_g}} + \frac{R_{gb}}{1+R_{gb}Q_{gb}(jw)^{n_{gb}}} \qquad (6.4)$$

where, Q is a frequency independent constant and n is the empirical exponent. n can be characterized as the phase element of resistor or capacitor.

From Eq. 6.4, the real and imaginary part of the impedance can be derived as[41]:

$$Z' = \left[\frac{R_g\left(1+R_gQ_gw^{n_g}\cos\left(\frac{n_g\pi}{2}\right)\right)}{1+2R_gQ_gw^{n_g}\cos(\frac{n_g\pi}{2})+\left(R_gQ_gw^{n_g}\right)^2}\right] + \left[\frac{R_{gb}\left(1+R_{gb}Q_{gb}w^{n_{gb}}\cos\left(\frac{n_{gb}\pi}{2}\right)\right)}{1+2R_{gb}Q_{gb}w^{n_{gb}}\cos(\frac{n_{gb}\pi}{2})+\left(R_{gb}Q_{gb}w^{n_{gb}}\right)^2}\right] \qquad (6.5)$$

and

$$Z^{//} = \left[\frac{R_g^2 Q_g w^{n_g} \sin\left(\frac{n_g \pi}{2}\right)}{1 + 2R_g Q_g w^{n_g} \cos(\frac{n_g \pi}{2}) + \left(R_g Q_g w^{n_g}\right)^2}\right] + \left[\frac{R_{gb}^2 Q_{gb} w^{n_{gb}} \sin\left(\frac{n_{gb} \pi}{2}\right)}{1 + 2R_{gb} Q_{gb} w^{n_{gb}} \cos(\frac{n_{gb} \pi}{2}) + \left(R_{gb} Q_{gb} w^{n_{gb}}\right)^2}\right] \quad (6.6)$$

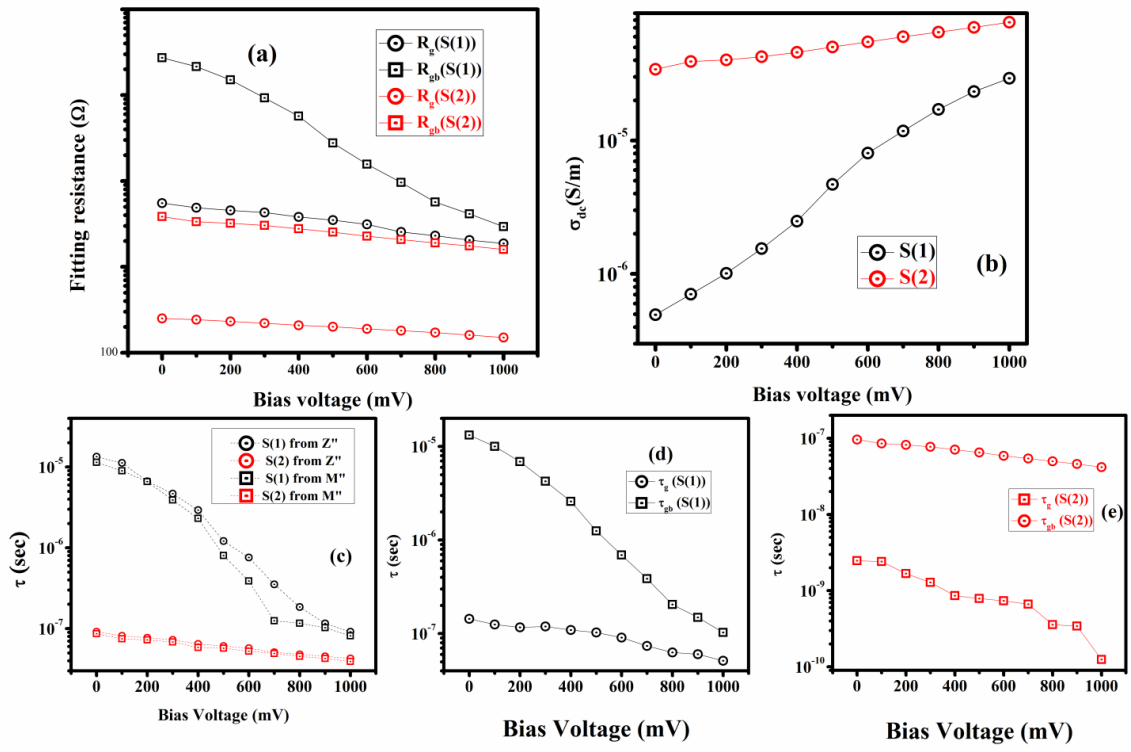

Fig. 6.10: (a) The fitted resistance value of S(1) and S(2) as a function of bias voltage. **(b)** σ_{dc} versus bias voltage. **(c)** relaxation time versus bias voltage obtained from impedance and electrical modulus value. **(d)** and **(e)** The grain and grain boundary relaxation time as a function of bias voltage for S(1) and S(2) respectively.

The fitted grain and grain boundary resistance values are illustrated in Fig. 6.10(a). It is observed that the grain boundary resistance of both samples is higher than grain resistance. In contrast, the grain and grain boundary resistance of S(2) is lower than S(1) throughout the bias voltage region. The lessening of grain and grain boundary resistance may have resulted from the release of space charges with the increment of bias voltage.[41]

All the fitted parameters are provided in Table – 6.3 (the 'g' and 'gb' index are denoted for grain and grain boundary).We have evaluated grain relaxation time (τ_g) and grain boundary relaxation time (τ_{gb}) from the fitted parameter by using the following relation(Eq. 6.7),[41]

$$\tau_g = \left(R_g Q_g\right)^{1/n_g} \text{ and } \tau_{gb} = \left(R_{gb} Q_{gb}\right)^{1/n_{gb}} \quad (6.7)$$

Table - 6.3: Fitted parameters obtained from the equivalent circuit simulation

Bias voltage (mV)	S(1)							
	$R_g(\Omega)$	$R_{gb}(\Omega)$	$n_g(\Omega)$	n_{gb}	Q_g	Q_{gb}	C_g(F)	C_{gb}(F)
0	5518.7	272900	0.98372	0.9912	3.3701E-11	5.3462E-11	2.60769E-11	4.84296E-11
100	4877.1	214900	0.98262	0.99212	3.3857E-11	5.0936E-11	2.56856E-11	4.65183E-11
200	4555.3	150640	0.98518	0.99646	3.2496E-11	4.7638E-11	2.56503E-11	4.5675E-11
300	4296.2	92886	0.99	0.99999	3.2524E-11	4.5744E-11	2.77309E-11	4.57383E-11
400	3827.2	56916	0.98829	0.99963	3.4389E-11	4.5577E-11	2.85031E-11	4.53605E-11
500	3507.3	27687	0.98475	0.99672	3.7525E-11	4.7299E-11	2.93606E-11	4.52369E-11
600	3125.2	15721	0.98	0.99999	4.0174E-11	4.4009E-11	2.90472E-11	4.40028E-11
700	2554.5	9633.7	0.98637	0.99786	3.6123E-11	4.1303E-11	2.88784E-11	4.0018E-11
800	2314.8	5682.7	0.98903	0.99659	3.2545E-11	3.7959E-11	2.71318E-11	3.60168E-11
900	2054.4	4137.8	0.98899	0.99999	3.5143E-11	3.6054E-11	2.92641E-11	3.60483E-11
1000	1875.1	2939.7	0.98633	0.99769	3.4364E-11	3.6305E-11	2.73176E-11	3.49804E-11
Bias voltage (mV)	S(2)							
	$R_g(\Omega)$	$R_{gb}(\Omega)$	$n_g(\Omega)$	n_{gb}	Q_g	Q_{gb}	C_g(F)	C_{gb}(F)
0	251.1	3848	0.99999	0.99999	9.8521E-12	2.4991E-11	9.85015E-12	2.4987E-11
100	242.7	3359.8	0.99999	0.98999	9.9478E-12	2.9991E-11	9.94583E-12	2.54827E-11
200	231.96	3218.7	0.99999	0.98999	7.2236E-12	2.9905E-11	7.22214E-12	2.53979E-11
300	220.55	3035.7	0.99999	0.98999	5.8148E-12	2.9925E-11	5.81361E-12	2.54E-11

400	208.8	2785	0.99998	0.98999	4.1094E-12	3.0097E-11	4.10768E-12	2.55252E-11
500	200.5	2535	0.99999	0.98962	3.9278E-12	3.0576E-11	3.92698E-12	2.57512E-11
600	190	2274	0.99992	0.98999	3.8757E-12	3.0625E-11	3.86918E-12	2.59244E-11
700	181	2085	0.99951	0.98752	3.7043E-12	3.2134E-11	3.66614E-12	2.60797E-11
800	171.33	1904	0.99007	0.98725	2.5885E-12	3.2466E-11	2.08564E-12	2.62016E-11
900	160.99	1752	0.99139	0.9855	2.5621E-12	3.3568E-11	2.1237E-12	2.62748E-11
1000	150.01	1596	0.99	0.98152	1.0436E-12	3.5909E-11	8.30788E-13	2.62335E-11

It is very clear that, the relaxation time is proportional to the product of resistance and capacitance, which indicates an enhancement of relaxation time if the product of resistance and capacitance increases.

The grains are generally more conductive than the grain boundary.[43] This conducting behavior depends on the distribution of grain, its size, and the nature of the connectivity between two grains through the grain boundary. Because this boundary behaves as a trap and constructs a barrier through which the carriers feel a constraint to transport to the neighbor particle. This barrier layer possesses high resistance and capacitance and executes higher relaxation time for the carrier at the grain boundary.

The relaxation time is measured from Z″ versus frequency plot using the following relation (Eq. 6.8),

$$\tau = \frac{1}{\omega_{\mathrm{m}}} = \frac{1}{2\pi f_{\mathrm{m}}} \qquad (6.8)$$

Where f_m is the frequency at which the peak has appeared for a specific bias voltage. The measured values of relaxation time with frequency are illustrated in Fig. 6.10(c). The relaxation time of S(2) is lower than S(1) for specific frequency and it reflects the better ability of conduction for S(2). Therefore, the grain boundary response occurs towards a lower frequency than grain.[43] Here, both grain and grain boundary relaxation times of S(2) are lower than S(1) (Fig. 6.10(d) and 6.10(e))and decreases with the increase of bias voltage. The larger grain size and lower grain boundary of S(2) may be the reason for lower relaxation time.

The electrical modulus is another representation to designate the relaxation mechanism of the external field in the material and provide an idea about the electrical response of the material.[44] It is proportional to the impedance of the material and involved with the range of conduction and the behavior of dielectric relaxation phenomena.[45, 46] The electric modulus can be expressed in terms of impedance as:

$$M^* = M^{/} - jM^{//} = j\omega\varepsilon_0 Z^* = -\omega\varepsilon_0 Z^{//} + j\omega\varepsilon_0 Z^{/} \qquad (6.9)$$

where M′ and M″ are the real and imaginary parts of the electric modulus.

Fig. 6.11 represents the frequency dependency on M′for both the samples at different bias voltages. The figure illustrates that, both samples exhibit almost zero magnitude of M′at the low-frequency region. At the higher frequency region the value of M′ decreases with the enhancement of applied bias voltage.

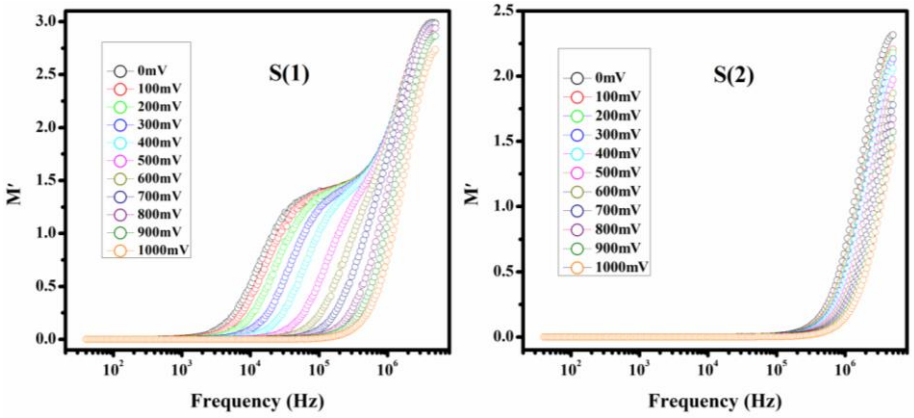

Fig. 6.11: M′ versus frequency at different bias voltage for S(1) and S(2)

However, a continuous dispersion in M′is observed at every bias voltage after a certain frequency increment for samples. It is also noteworthy that this dispersive region appears towards a higher frequency as the bias voltage increases. For S(1), the value of M′ increases steeply and then a sigmoidal, the increment is viewed for low bias voltage. But at the higher voltage, the enhancement of M′ follows a singular way of the uprising. Overall, the M′approach towards a definite value, which is termed as M_∞′. Surprisingly, at every bias voltage, M′of S(2) enhances sharply, although the values at the dispersive region are quite congested than S(1). These whole phenomena differentiate the types of conduction ranges which occurred in the material. The low value of M′ at low frequency may be designated by the negligible contribution from the electrode[47] wherever the dispersive behavior at the

higher frequency indicates the long-range mobility of charge carriers. The lack of restoring force under the external induced electric field may assist the charge carrier to mobile within the long-range.[48]

Moreover, the approaching of M′ towards the M_{∞}' value attributes to the short-range carrier mobility conduction mechanism.[41] Therefore, the relaxation mechanism of S(1) is influenced by both short and long-range ordered conduction, whereas the relaxation of S(2) is mainly governed by long-range ordered charge carriers' mobility.

Fig. 6.12 depicts the variation of M″ with frequency at different bias voltage for both samples. A distinguished nature has been observed in the frequency-dependent M″ for both samples which are pretty noteworthy from the viewpoint of conduction and relaxation phenomena. The M″ of S(1) exhibits a lower value at low frequency and provides two peaks towards the higher frequency for low bias voltage. Along with, the low-frequency peak for S(1) has shifted towards a higher frequency region with the enhancement of bias voltage. In concerned to frequency limit the second peak is not obtained for the bias voltage of greater than 700 mV. On the contrary, S(2) exhibits only one peak for every bias voltage, those appears at higher frequency region. Moreover, the spreading of spectra distribution for S(2) are quite less than other one. The twin peaks in S(1) at various bias voltages may arise due to the migration of charge carriers from short time constants to long time constants through the reduction of frequency.[44] Only one peak has appeared (the same phenomena has occurred for S(1) at the bias voltage greater than 700 mV). In addition, the peak intensity of S(2) reduces with the enhancement of bias voltage and the opposite phenomena are observed for S(1).The shifting of peak

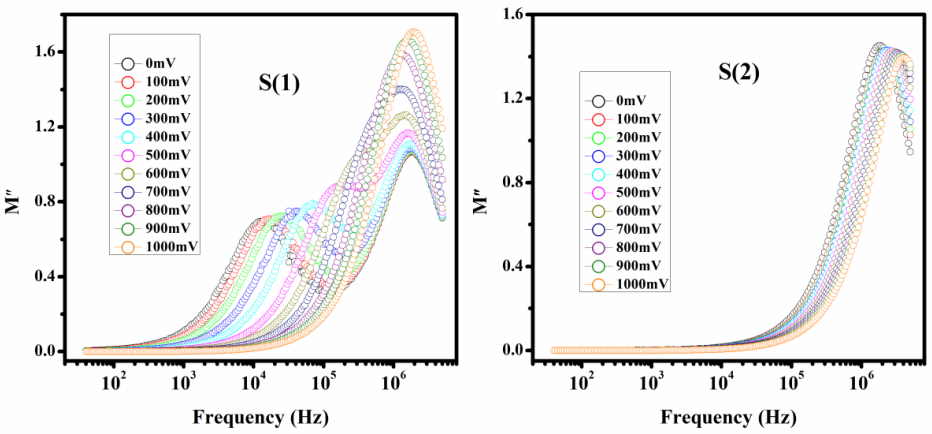

Fig. 6.12: M″ as a function of frequency under the different bias voltage for S(1) and

frequency indicates that the conductivity relaxation is dependent on external bias voltage and the hopping of charge carriers plays the dominant role. In general, the shifting in characteristic frequency (at which the peaks are observed) at a constant peak, intensity indicates the variation in resistance. Change in peak intensity without shifting characteristic frequency implies the variation in capacitance. Here, Fig. 6.12 suggests that the synthesized materials undoubtedly have a combined impact of resistance and capacitance in the conduction procedure. From the M″ vs. frequency plot using the Eq. 6.8 relaxation time (τ) are also deducted (Fig. 6.10(c)). These data curves exemplify the comparative relaxation information of S(1) and S(2) obtained from impedance data. These graphs interestingly illustrate a slight difference the value of relaxation times, obtained from electric modulus and impedance. It is illustrated previously that the dual peak in M″ vs frequency plot for lower bias indicating the existence of delocalized and localized relaxation. For the higher bias, those two peaks are merged and we get only one peak for S(1) and for S(2) respectively at all bias voltage. In overall the deviations of relaxation time obtained from electrical modulus and impedance are lower for S(2) sample. The difference of peak frequency for Z″ and M″ is originated from the short range localized relaxation behavior which leads to the non-ideal Debye behavior. The slighter deviation of relaxation time obtained from Z″ and M″(Fig 6.9(c)) depicts the delocalized long range conduction behavior of S(2).

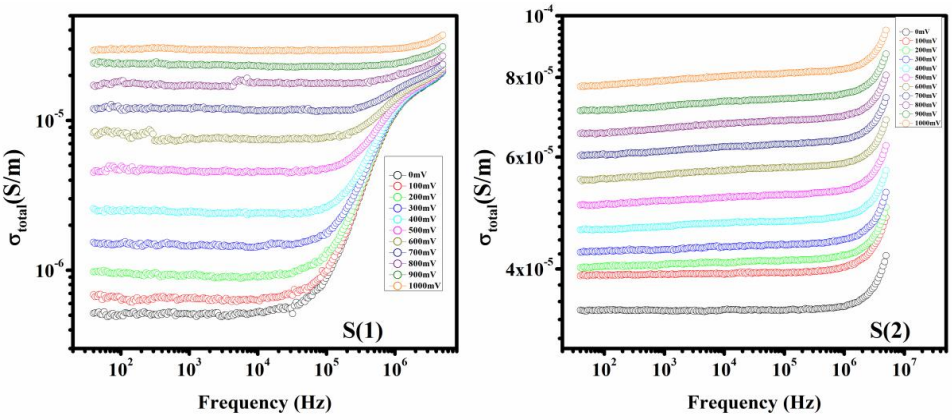

Fig. 6.13: ac conductivity versus frequency at the bias voltage 0 mV- 1000 mV for S(1) and S(2)

The frequency dependent conductivity of sample S(1) and S(2) are recorded for different bias voltages. Fig. 6.13 represents the curves having two distinguished regions. One of them is frequency independent which is known as dc conductivity (σ_{dc}) and another is the

frequency-dependent dispersive region, known as ac conductivity (σ_{ac}). To get into the mechanism, relevant to transport of charge carriers, the following equation (Eq. 6.10)[41] is employed. Equation 8 is necessarily employed to elucidate the bias voltage-dependent (at the bias voltage from 0 mV to 1000 mV) conductivity of both the samples as a function of frequency as obtained in Fig. 6.13.

$$\sigma_{total} = \sigma_{dc} + \sigma_{ac} = \frac{Z^{/}}{Z^{/2} + Z^{//2}} \cdot \frac{d}{A} \qquad (6.10)$$

Here, 'd' is the thickness of the film, 'A' is the effective area. At the lower frequency region, the charge carriers jump from one site to the neighbor site successfully and dominate the conducting behavior of the material. These hopping motions take a long time to execute the jumping successfully and it results in long-range translational motion in terms of frequency-independent dc conductivity.[49] The dispersive frequency-dependent conductivity at high frequency can only be understood by using a suitable theoretical approach such as quantum mechanical tunneling model, polaron tunneling model, atomic hopping model, correlated barrier hopping model.[50] Generally, it can be illustrated by considering the occurrence of deep electronic states near the Fermi level, those control the ac conductivity.[51] The deep or shallow defect centers are induced by the external electric field and generate a transition of charges by covering the short or long distance in the material as a function of frequency.[50] However, the dc conductivity of S(1) is found lower than S(2) (illustrated in Fig. 6.10(b)) and enhanced with the increment of bias voltage. On other hand, the transition from dc to ac conductivity happens at a higher frequency for S(2) than S(1). These two phenomena support the better conducting nature of S(2) and approve the impedance and electric modulus pattern aptly, as discussed above.

Several possibilities can be adopted to explain the size-dependent conduction mechanism for the synthesized materials. Among them, the first consideration is based on traveling via nearest-neighbor hopping. The transport probability of a carrier is directly related to the crystallite size because of a larger particle needs fewer hops to cover up a finite distance.[52] Therefore, the larger particle exhibits higher conductivity. The next possibility is related to the energy distribution in the electronic state and its dependency on crystallite size. The

particle radius is inversely proportional to the width of the lowest electronic state which indicates the lower width of the electronic state for larger particles. It makes the interparticle coupling stronger as the energy distribution in the electronic state chooses the narrow path.[53] Therefore, the conductance of S(2) has been improved than S(1). Moreover, the larger particle contains a smaller number of traps density as its grain boundary is lower, as well as fewer amounts of charges are trapped in between two grains in comparison to the smaller particle.

6.4. Conclusion

Here the influence of crystallite size of hydrothermally (at temperature500^0C and 600^0C) derived Cadmium Oxide (CdO)s upon the conduction and relaxation mechanism are demonstrated aptly. Impedance behavior has been studied well which approved the better conducting performance of CdO derived at a higher temperature. Moreover, the relaxation time for grain and grain boundary also decreases for the sample derived from higher temperatures. The electric modulus and ac conduction study in addition provide better aspects on the relaxation and conduction of CdO, derived at high-temperature. So, this work explores the experimental and theoretical view of relaxation and conduction mechanism and offers insightful information about the behavioral and morphological impacts of synthesized CdO in different aspects. So, this literature will expedite the study about CdO based signal network systems.

References

1. S. Senthil, S. Srinivasan, T. Thangeeswari, B. Madhu and M. Silambarasan, *Nano-Structures & Nano-Objects*, 2020, **24**, 100554.
2. R. S. Mane, H. M. Pathan, C. D. Lokhande and S.-H. Han, *Solar Energy*, 2006, **80**, 185-190.
3. R. A. Ismail and O. A. Abdulrazaq, *Solar Energy Materials and Solar Cells*, 2007, **91**, 903-907.
4. Y. Hameş and S. Eren San, *Solar Energy*, 2004, **77**, 291-294.
5. B. A. Gozeh, A. Karabulut, C. B. Ismael, S. I. Saleh and F. Yakuphanoglu, *Journal of Alloys and Compounds*, 2021, **872**, 159624.
6. S. Dugan, M. M. Koç and B. Coşkun, *Journal of Molecular Structure*, 2020, **1202**, 127235.
7. I. L. P. Raj, N. Chidhambaram, S. Saravanakumar, S. Sasikumar, S. Varadharajaperumal, D. Alagarasan, T. Alshahrani, M. Shkir and S. AlFaify, *Optik*, 2021, **241**, 166406.
8. W.-M. Cho, G.-R. He, T.-H. Su and Y.-J. Lin, *Applied Surface Science*, 2012, **258**, 4632-4635.
9. M. Raaif and S. H. Mohamed, *Applied Physics A*, 2017, **123**, 441.
10. R. N. Bulakhe and C. D. Lokhande, *Sensors and Actuators B: Chemical*, 2014, **200**, 245-250.
11. A. B. Bodade, A. M. Bende and G. N. Chaudhari, *Vacuum*, 2008, **82**, 588-593.
12. X. Fu, J. Liu, T. Han, X. Zhang, F. Meng and J. Liu, *Sensors and Actuators B: Chemical*, 2013, **184**, 260-267.
13. D. S. Dhawale, A. M. More, S. S. Latthe, K. Y. Rajpure and C. D. Lokhande, *Applied Surface Science*, 2008, **254**, 3269-3273.
14. H. Khallaf, C.-T. Chen, L.-B. Chang, O. Lupan, A. Dutta, H. Heinrich, A. Shenouda and L. Chow, *Applied Surface Science*, 2011, **257**, 9237-9242.
15. M. Ocampo, A. M. Fernandez and P. J. Sebastian, *Semiconductor Science and Technology*, 1993, **8**, 750-751.
16. T. Singh, D. K. Pandya and R. Singh, *Materials Chemistry and Physics*, 2011, **130**, 1366-1371.

17. A. Seshadri, N. R. de Tacconi, C. R. Chenthamarakshan and K. Rajeshwar, *Electrochemical and Solid-State Letters*, 2006, **9**, C1.
18. W. Ismail, M. Bakry, M. Elshobaki, A. El-Shaer and M. Abdelfatah, *Materials Science in Semiconductor Processing*, 2021, **133**, 105959.
19. K. T. R. Reddy, G. M. Shanthini, D. Johnston and R. W. Miles, *Thin Solid Films*, 2003, **427**, 397-400.
20. R. Ferro and J. A. Rodríguez, *Thin Solid Films*, 1999, **347**, 295-298.
21. R. Ferro, J. A. Rodríguez, O. Vigil and A. Morales-Acevedo, *Materials Science and Engineering: B*, 2001, **87**, 83-86.
22. K. Kaviyarasu, E. Manikandan, J. Kennedy and M. Jayachandran, *Materials Letters*, 2014, **120**, 243-245.
23. Y. C. Zhang and G. L. Wang, *Materials Letters*, 2008, **62**, 673-675.
24. J. Lee, J. H. Hwang, J. J. Mashek, T. O. Mason, A. E. Miller and R. W. Siegel, *Journal of Materials Research*, 1995, **10**, 2295-2300.
25. A. Sacco, *Renewable and Sustainable Energy Reviews*, 2017, **79**, 814-829.
26. F. F.-Santiago, J. Bisquert, G. G.-Belmonte, G. Boschloo and A. Hagfeldt, *Solar Energy Materials and Solar Cells*, 2005, **87**, 117-131.
27. R. Tripathi, A. Dutta, S. Das, A. Kumar and T. P. Sinha, *Applied Nanoscience*, 2016, **6**, 175-181.
28. A. S. Roy, K. R. Anilkumar and M. V. N. A. Prasad, *Journal of Applied Polymer Science*, 2012, **123**, 1928-1934.
29. A. S. Roy, K. R. Anilkumar and M. V. N. A. Prasad, *Ferroelectrics*, 2011, **413**, 279-290.
30. P. Thomas and K. E. Abraham, *Journal of Advanced Dielectrics*, 2016, **06**, 1650030.
31. P. Choudhary, P. Saxena, A. Yadav, V. N. Rai and A. Mishra, *Ionics*, 2019, **25**, 4991-5001.
32. R. A. Ismail, A.-M. E. Al-Samarai, S. J. Mohmed and H. H. Ahmed, *Solid-State Electronics*, 2013, **82**, 115-121.
33. T. P. Gujar, V. R. Shinde, W.-Y. Kim, K.-D. Jung, C. D. Lokhande and O.-S. Joo, *Applied Surface Science*, 2008, **254**, 3813-3818.
34. L. R. de León-Gutiérrez, J. J. Cayente-Romero, J. M. Peza-Tapia, E. Barrera-Calva, J. C. Martínez-Flores and M. Ortega-López, *Materials Letters*, 2006, **60**, 3866-3870.

35. R. Jenkins and R. L. Snyder, in *Introduction to X-ray Powder Diffractometry*, John Wiley & Sons, Inc., New York, 1996, vol. 138, pp. 47-95.
36. E. F. Kaelble, *Handbook of X-rays : for diffraction, emission, absorption, and microscopy*, McGraw-Hill, New York, 1967.
37. M. Kurian and C. Kunjachan, *International Nano Letters*, 2014, **4**, 73-80.
38. S. S. Mansoor, K. Aswin, K. Logaiya and S. P. N. Sudhan, *Journal of Saudi Chemical Society*, 2016, **20**, 517-522.
39. R. K. Panda, R. Muduli, S. K. Kar and D. Behera, *Journal of Alloys and Compounds*, 2014, **615**, 899-905.
40. A. Kaushal, S. M. Olhero, B. Singh, D. P. Fagg, I. Bdikin and J. M. F. Ferreira, *Ceramics International*, 2014, **40**, 10593-10600.
41. J. Datta, M. Das, A. Dey, S. Sil, R. Jana, S. Halder, P. Das and P. P. Ray, *Materials Chemistry and Physics*, 2018, **213**, 23-34.
42. S. Saha, S. Chanda, A. Dutta and T. P. Sinha, *Materials Research Bulletin*, 2013, **48**, 4917-4923.
43. M. Idrees, M. Nadeem, M. Atif, M. Siddique, M. Mehmood and M. M. Hassan, *Acta Materialia*, 2011, **59**, 1338-1345.
44. M. Coşkun, Ö. Polat, F. M. Coşkun, Z. Durmuş, M. Çağlar and A. Türüt, *RSC Advances*, 2018, **8**, 4634-4648.
45. P. Chandra Sati, M. Kumar and S. Chhoker, *Ceramics International*, 2015, **41**, 3227-3236.
46. V. F. Lvovich, *Impedance spectroscopy: applications to electrochemical and dielectric phenomena*, John Wiley & Sons, 2012.
47. S. L. Agrawal, M. Singh, M. Tripathi, M. M. Dwivedi and K. Pandey, *Journal of Materials Science*, 2009, **44**, 6060-6068.
48. M. Ravi, S. Bhavani, K. K. Kumar and V. V. R. N. Rao, *Solid State Sciences*, 2013, **19**, 85-93.
49. S. Sil, J. Datta, M. Das, R. Jana, S. Halder, A. Biswas, D. Sanyal and P. P. Ray, *Journal of Materials Science: Materials in Electronics*, 2018, **29**, 5014-5024.
50. A. Kahouli, A. Sylvestre, F. Jomni, B. Yangui and J. Legrand, *The Journal of Physical Chemistry A*, 2012, **116**, 1051-1058.

51. A. R. Long, *Advances in Physics*, 1982, **31**, 553-637.
52. Y. Liu, M. Gibbs, J. Puthussery, S. Gaik, R. Ihly, H. W. Hillhouse and M. Law, *Nano Letters*, 2010, **10**, 1960-1969.
53. M. S. Kang, A. Sahu, D. J. Norris and C. D. Frisbie, *Nano Letters*, 2010, **10**, 3727-3732.

Chapter 7

Summary

7.1. Summary

In pursuit of comprehending and enhancing the performance of photo-electronic junction devices designed with inorganic semiconductor nanocomposites, the charge transfer dynamics and conduction kinetics are extremely important. Surface effects and quantum confinement often give rise to special electrical features of the materials. The theoretical understanding about carriers' dynamics requires a thorough practical investigation of the interfacial interactions, electronic band structure and carrier mobility. In subject to understand the charge transfer mechanisms experimentally, current-voltage (I-V) characteristics, ac impedance spectroscopy (IS) and thorough study of absorption and emission related spectroscopy data of the materials along with the analytical investigations are quite essentially examined. All the experimental deeds along with their results are summarized here as follows.

This dissertation is mainly focused upon the original synthesis technique and characterization processes. The ternary I-III-VI_2 Semiconductor $CuInSe_2$ has been synthesized and characterized, and their potential applicability in thin film Schottky barrier diodes have been examined and demonstrated accordingly. In later part, Cadmium Oxide (CdO) has been synthesized by hydrothermal route and the morphological impact of the derived CdO on charge conduction and relaxation within Schottky diode is investigated by using bias-dependent impedance spectroscopy (IS). This thesis work has focused not only on the synthesis and characterizations of the above semiconductors but also focused on the optoelectronic device fabrication followed by the investigation of the charge transport properties via impedance spectroscopy (IS) and analysis of current-voltage (I-V) data.

In the prolonged course of these experimental studies, first of all, the Copper Indium Selenide ($CuInSe_2$) has been synthesized via solvothermal synthesis route and the structural, optical and electrical properties have been characterized aptly. Thereafter, Al/$CuInSe_2$ Schottky Diode (SD) has been fabricated and characterized. The carrier transport dynamics have been investigated with the help data analysis of dc current-voltage (I-V) and ac impedance spectroscopy (IS). Fundamental parameters of Schottky like ideality factor, barrier height and series resistance was obtained from conventional current-voltage characteristics by adopting thermionic emission theory. Metal-semiconductor interfaces are

properly identified by using impedance spectroscopy analysis at different dc bias under dark condition. Moreover, the charge transport mechanism through Al/$CuInSe_2$ is extensively analyzed by employing space charge limited current (SCLC) theory. It has been observed that after illumination of light the mobility is increased ~5 fold. Over all, the experimental analysis involved me to get insights into the charge transport mechanism, and the physics of Schottky interfaces.

After that, we established the successful energy quenching and resonance energy transfer process from P3HT to $CuInSe_2$ via Fluorescence Resonance Energy Transfer (FRET) analysis by compositing P3HT:$CuInSe_2$. The motivation has come from the study of absorption and emission spectra of the said composite materials. The photo-induced charge transport phenomenon has been successfully examined through estimation of band structures along with proper band diagram. This composition demonstrates the enormous prospective of solvothermally derived $CuInSe_2$, as an acceptor of excitons, created from P3HT donor polymer. The estimate value of the Förster distance (R_0) of critical energy transfer and thorough studies of absorption and emission spectra highly ensured the possibility of resonance energy transfer from P3HT to $CuInSe_2$ in context to fabricate efficient photovoltaics.

In a while, the hetero-junctions of the configuration TiO_2/$CuInSe_2$ and HF-TiO_2/$CuInSe_2$ have been made to understand the underlined carrier dynamics for my own interest and it has been observed that the junctions show p-n diode like behavior. It has also been observed that the room temperature I-V measurement of the devices shows significant impact of incident white light on carrier transport mechanism and the overall performance of the devices. Meticulous computational investigations revealed that in compare to the first kind of device, the second one is more efficient towards the light response. Moreover, the devices under the influence of the light soaking, should offer us distinct current rectification and photosensitivity. The ITO/TiO_2/$CuInSe_2$/Al and ITO/HF-TiO_2/$CuInSe_2$/Al structures are implementing the signature of the first kind of p-n junction acting as a photo-sensing device.

Almost all of the contemporary works, in Addition, two different crystallite size based Cadmium Oxide (CdO)s have been synthesized via hydrothermal route at temperature, 500^0C and 600^0C. The influence of crystallite size of derived Cadmium Oxide (CdO)s upon the conduction and relaxation mechanism have been investigated and demonstrated aptly.

Impedance behavior has been studied well which approved the better conducting performance of CdO derived at a higher temperature. Moreover, the relaxation time for grain and grain boundary also decreases for the sample derived from higher temperatures. The work explores the experimental and theoretical view of relaxation and conduction mechanism and offers insightful information about the behavioral and morphological impacts of synthesized CdO in different aspects. Hence, the work will accelerate the research on signal transport network systems based on CdO.

As a whole, this thesis illustrated the successful synthesis of Copper indium Selenide ($CuInSe_2$) nanocomposite and its implication in thin film semiconductor devices. Several techniques were implemented to characterize the synthesized material. In order to get a better understanding of metal-semiconductor interfaces, the I-V characteristics and impedance spectroscopy analysis of the devices were thoroughly discussed. In order to exploit the potential of the material for the application in optoelectronic devices, the photo responsivity of the fabricated Schottky devices has also been investigated. The performances of the fabricated devices were investigated by analyzing the electrical and the charge transports parameters. Significant charge transport parameters like effective charge carrier mobility, transit time and carrier concentration of the fabricated devices have been estimated. So the huge improvements in thin film device performance, photoresponse and charge transport properties of Copper indium Selenide ($CuInSe_2$) nanocomposites make it an outstanding support material for various photo-electronic junction device application. In Addition, two different crystallite size based Cadmium Oxide (CdO)s have been synthesized and the dc conductivity is also evaluated by measuring current-voltage characteristics. The morphological impact of derived CdO on charge conduction and relaxation has been investigated by using bias-dependent impedance spectroscopy (IS).

List of Publications

Journals

1. **Animesh Biswas,** Sayantan Sil, Arka Dey, Joydeep Datta, Dhananjoy Das, and Partha Pratim Ray, **"Investigation of conduction kinetics in Al/$CuInSe_2$ Schottky device utilizing impedance spectroscopy (IS) measurement and study of its photosensing behaviour,"** Journal of Physics and Chemistry of Solids **150**, 109878 (2021).

2. **Animesh Biswas,** Baishakhi Pal, Mainak Das, Ramjan Sk, Animesh Layek, and Partha Pratim Ray, **"An experimental approach to ensure energy quenching and fluorescence resonance energy transfer of excitons from P3HT to $CuInSe_2$,"** Materials Letters **338**, 134066 (2023).

3. Joydeep Datta, **Animesh Biswas,** Somobrata Acharya, Animesh Layek, and Partha Pratim Ray, **"Effect of size of CdO on bias dependent conduction and relaxation mechanism by means of impedance spectroscopy: Experimental and theoretical studies,"** Materials Chemistry and Physics **301**, 127542 (2023).

4. Ramjan Sk, **Animesh Biswas**, Animesh Layek, and Partha Pratim Ray, **"Performance of Schottky diode of structured FTO/TiO2/Al employing hydrogen fluoride treated TiO2: Qualitative and quantitative analysis,"** Chemical Physics **580**, 112233 (2024).

5. Indrajit Pal, **Animesh Biswas,** Santanu Majumdar, Gerald Lepcha, Baishakhi Pal, Partha Pratim Ray, and Biswajit Dey, **"Unveiling the Semiconducting Diode Property through Current Density–Voltage Features with Effective Interface Mobility and Conductivity of Nitroterephthalic Acid-Directed Supramolecular Co(II)/Cu(II) Metallogels,"** ACS Applied Engineering Materials **1** (11), 3005-3015 (2023).

6. Rabi Sankar Sarkar, **Animesh Biswas**, Partha Pratim Ray, Rosa M. Gomila, Michael G. B. Drew, Snehasis Banerjee, Antonio Frontera, and Shouvik Chattopadhyay, **"An insight into the non-covalent interactions in the solid state structures of dinuclear cobalt(ii) complexes with N,O-donor ligands: application of the complexes in the fabrication of Schottky devices,"** CrystEngComm **25** (6), 1006-1017 (2023).

7. Dhananjoy Das, Mainak Das, **Animesh Biswas**, Puspendu Sahu, and Partha Pratim Ray, **"Exploring reduced graphene oxide-zinc telluride nanocomposites for enhanced charge transfer in optoelectronic devices: a study of the metal–semiconductor interfaces via equivalent circuit model,"** Journal of Materials Science: Materials in Electronics **34** (21), 1574 (2023).

8. Sayantan Sil, Rajkumar Jana, **Animesh Biswas,** Dhananjoy Das, Arka Dey, Joydeep Datta, Dirtha Sanyal, and Partha Partha Ray, **"Elucidation of Inhomogeneous Heterojunction Performance of Al/Cu5FeS4 Schottky Diode With a Gaussian Distribution of Barrier Heights,"** IEEE Transactions on Electron Devices **67** (5), 2082-2087 (2020).

9. Mainak Das, Dhananjoy Das, Supravat Ghosh, Ramjan Sk, **Animesh Biswas**, and Partha Pratim Ray, **"Investigation of charge transfer in optoelectronic devices: a study of carbon nanotube-copper sulfide nanocomposites using equivalent circuit models for metal–semiconductor interfaces,"** Journal of Materials Science: Materials in Electronics **35** (17), 1143 (2024).

10. Rajkumar Jana, Joydeep Datta, Sayantan Sil, Arka Dey, Baishakhi Pal, **Animesh Biswas**, and Partha Pratim Ray, **"Exploration of temperature dependent dielectric relaxation and correlated barrier hopping (CBH) conduction mechanism of hydrothermally synthesized CuO nanoflakes,"** Materials Research Express **6** (10), 1050d1051 (2019).

11. Sayantan Sil, Joydeep Datta, Mrinmay Das, Rajkumar Jana, Soumi Halder, **Animesh Biswas,** Dirtha Sanyal, and Partha Pratim Ray, **"Bias dependent conduction and relaxation mechanism study of Cu5FeS4 film and its significance in signal transport network,"** Journal of Materials Science: Materials in Electronics **29** (6), 5014-5024 (2018).

12. Soumi Halder, Baishakhi Pal, Arka Dey, Sayantan Sil, Pubali Das, **Animesh Biswas,** and Partha Pratim Ray, **"Effect of graphene on improved photosensitivity of MoS2-graphene composite based Schottky diode,"** Materials Research Bulletin **118**, 110507 (2019).

Conference Proceedings

1. Mrinmay Das, Joydeep Datta, **Animesh Biswas**, Soumi Halder, and Partha Pratim Ray, **"Enhanced charge transport properties of rGO-TiO2 based Schottky diode by tuning graphene content,"** Materials Today: Proceedings **11**, 776-781 (2019).

Under Review

1. **Animesh Biswas**, Ramjan Sk, Animesh Layek, Partha Pratim Ray, **"Recognition of Light Sensing p-n Junction for Hetero-Structure $CuInSe_2/TiO_2$ and $CuInSe_2$/HF-TiO_2: Study of Carrier Transport Mechanism" (Under review).**

Conferences/Seminars Attended

1. Participation in "**Twist and Turns in Physics Research: Special Emphasis on Condensed Matter and Biophysics (TTPR-2017)**", February 21-22, 2017, Department of Physics, Jadavpur University, Kolkata, India.

2. Poster Presentation entitled "Bias Dependent Impedance Spectroscopy Study of $CuInSe_2$ Nanoparticles" in **"Fourth International Symposium on Semiconductor Materials and Devices (ISSMD 4)",** March 8-10,2017, Jadavpur University, Kolkata, India.

Workshops Attended

1. Participation in **"Two-day workshop on Material Characterization Techniques",** February 02-02, 2023, CSIR-Central Glass and Ceramic Research Institute, Kolkata, India.

2. Paper presentation entitled "Surfactant guided synthesis of TiO2: morphological impact on optoelectronic switching device" in **"Indian Workshop and symposium on Modeling, Experimentation and Simulation on Complex Systems",** August 05-08, 2015, Haldia institute of Technlogy, Haldia, India.

Animesh Bhowmik

24/09/24

ANNEXURE

β–CIS Phase ($Cu_2In_4Se_7$ and $CuIn_3Se_5$)

Various nomenclatures are used by different researchers to describe the β–CIS compounds. They are sometimes referred to as P-chalcopyrite, a term created by Hönle and co-workers when they concluded that the structure possesses P42c symmetry.[1] These structures are also sometimes referred to generically as "Ordered Defect Compounds" (ODC's).[2, 3] β-CIS is a high-pressure polymorph of $CuInSe_2$ as it has been observed under conditions of high pressure and temperature.[4, 5] The structure of β-CIS is less well-defined compared to α-CIS, but it is known to have a higher density due to the more compact arrangement of atoms. The high-pressure phase tends to adopt a rock-salt or distorted rock-salt structure, where Cu and In atoms are randomly distributed in the cation sub-lattice. Each Se atom is octahedrally coordinated by Cu and In atoms, leading to different electronic properties. The band gap in β-CIS is typically narrower than in α-CIS due to the increased overlap of atomic orbitals under high pressure.

γ–CIS Phase ($CuIn_5Se_8$)

γ-CIS refers to a defect version of the chalcopyrite structure, where some of the cation sites are either vacant or occupied by different atoms, leading to a non-stoichiometric composition.[6] The lattice constants are similar to those of α-CIS but slightly varied due to the presence of defects. Defects can lead to disordered regions within the chalcopyrite lattice, affecting the overall symmetry and periodicity.[7] The presence of vacancies or interstitials alters the local coordination environment around Se atoms. Defect chalcopyrite structures often exhibit localized states within the band gap, which can influence electronic and optical properties.

δ–CIS Phase (Sphalerite)

δ-CIS is an ordered vacancy compound (OVC) phase, characterized by a specific arrangement of vacancies within the crystal structure. δ-CIS typically adopts a structure with a larger unit cell compared to α-CIS to accommodate the ordered vacancies. The vacancies

are ordered in a regular pattern, often leading to a superlattice structure. The ordered vacancies create a unique coordination environment for the Se atoms, with some tetrahedral sites being vacant. The presence of ordered vacancies can lead to band gap narrowing and the introduction of mid-gap states.

References

1. W. Hönle, G. Kühn and U. C. Boehnke, *Crystal Research and Technology*, 1988, **23**, 1347-1354.
2. M. León, R. Serna, S. Levcenko, A. Nateprov, A. Nicorici, J. Merino and E. Arushanov, *Journal of applied physics*, 2007, **101**.
3. R. Marquez and C. Rincon, *Solar energy materials and solar cells*, 2002, **71**, 19-26.
4. L.-C. Xu, R.-Z. Wang, L.-M. Liu, Y.-P. Chen, X.-L. Wei, H. Yan and W.-M. Lau, *Journal of Materials Chemistry*, 2012, **22**, 21662-21666.
5. W. Li, Z. Pan and X. Zhong, *Journal of Materials Chemistry A*, 2015, **3**, 1649-1655.
6. I. Bodnar', V. Y. Rud' and Y. V. Rud', *Inorganic materials*, 2002, **38**, 873-875.
7. S. Zhang, S.-H. Wei, A. Zunger and H. Katayama-Yoshida, *Physical Review B*, 1998, **57**, 9642.

Publications, Conference and Workshop Certificates

Journal of Physics and Chemistry of Solids 150 (2021) 109878

Contents lists available at ScienceDirect

Journal of Physics and Chemistry of Solids

journal homepage: http://www.elsevier.com/locate/jpcs

Investigation of conduction kinetics in Al/$CuInSe_2$ Schottky device utilizing impedance spectroscopy (IS) measurement and study of its photosensing behaviour

Animesh Biswas [a,b], Sayantan Sil [a], Arka Dey [c], Joydeep Datta [a], Dhananjoy Das [a], Partha Pratim Ray [a,*]

[a] Department of Physics, Jadavpur University, Kolkata, 700032, India
[b] Department of Physics, Sreegopal Banerjee College, Mogra, Hooghly, 712148, India
[c] Department of Condensed Matter Physics and Material Sciences, S. N. Bose National Centre for Basic Sciences, Block JD, Sec. III, Salt Lake, Kolkata, 700106, India

ARTICLE INFO

Keywords:
Al/$CuInSe_2$ Schottky diode
Impedance spectroscopy (IS)
I–V Characteristics
Space charge limited current (SCLC)
Mobility

ABSTRACT

Copper Indium Selenide ($CuInSe_2$) has been synthesized by solvothermal synthesis method. The Schottky diode (SD) has been fabricated by using the material and the interface characteristics of Al/$CuInSe_2$/ITO have been investigated with the help of ac impedance spectroscopy (IS) analysis (under dark condition) and dc current-voltage (I–V) measurements (under both dark and photo condition). IS is a very important and powerful technique to investigate and analyze the impedance at the boundary regions of SDs. Ac impedance spectra of Al/$CuInSe_2$ SD have been recorded in the wide range of frequency from 40 Hz to 20 MHz during dc bias scanning from −0.5 V to 0.5 V under dark condition. From forward I–V characteristics, important parameters such as ideality factor (η), photosensitivity, barrier height (Φ_b), series resistance (R_S) of SD were obtained under dark and photo condition. The photosensitivity of the Al/$CuInSe_2$ SD was found to be 3.36. For better realization of charge transport phenomena through the MS junction, space charge limited current (SCLC) theory has been employed. The effective mobility of the carrier is evaluated in dark and photo condition as 0.42×10^{-3} $m^2V^{-1}s^{-1}$ and 2.11×10^{-3} $m^2V^{-1}s^{-1}$ respectively. It has been observed that the mobility is improved 5 times under illumination compared to the dark condition.

1. Introduction

For the sake of conservation of energy, a low cost sustainable power source is extremely essential for the well being of the human kind [1]. The conventional solar cells being very costly, it requires a search for materials for solar energy conversion. Photovoltaic cells based on I–III–VI compounds have shown a lot of promises for solar energy harvesting. Copper indium selenide ($CuInSe_2$) is one of those promising materials and a ternary chalcopyrite IB-IIIA-VIA compound semiconductor. It (CIS) has been one of the most potential absorber materials because few of its alluring characteristics for photovoltaic application such as high optical absorption coefficient, suitable band gap [2,3] that can harvest a wide range of visible lights which are ideal for the development of photovoltaic devices. This material has gained much attention for the researchers everywhere throughout the world also because of its good stability under radiation, low toxicity and high efficiency of PV devices [4]. Furthermore, one can reduce the absorption layer up to a several micrometers and by substituting of In^{3+} by Ga^{3+} the band gap can be adjusted from 1.00 eV to 1.68 eV [2]. In view of such optical and electrical properties it has became one of the most significant photovoltaic materials. Various researchers have paid their attention for the measurements of thermal conductivity, optical absorption, Raman spectra and magneto-resistance on both single and polycrystalline samples [5–9]. R. Bouferra et al. [10] reported the AC conductivity of n-$CuInSe_2$ material utilizing impedance spectroscopy (IS) over a broad range of temperatures [80 K–300 K] and frequencies [20 Hz-1 MHz]. The report also provided some useful insight about the conduction mechanism in the material. However, metal-semiconductor (MS) contacts are mostly used as rectifying junction for different electronic devices like solar cells, ICs and photosensitive detectors [11–15]. As the MS junction plays a pivotal role in different microelectronic devices, the study of the influence of this material on the performance of electronic

* Corresponding author.
E-mail addresses: partha@phys.jdvu.ac.in, parthapray@yahoo.com (P.P. Ray).

https://doi.org/10.1016/j.jpcs.2020.109878
Received 6 September 2020; Received in revised form 20 October 2020; Accepted 25 November 2020
Available online 1 December 2020

Materials Letters 338 (2023) 134066

Contents lists available at ScienceDirect

Materials Letters

journal homepage: www.elsevier.com/locate/matlet

An experimental approach to ensure energy quenching and fluorescence resonance energy transfer of excitons from P3HT to $CuInSe_2$

Animesh Biswas [a,b], Baishakhi Pal [a], Mainak Das [a], Ramjan Sk [a], Animesh Layek [a,*], Partha Pratim Ray [a]

[a] Department of Physics, Jadavpur University, Kolkata 700032, India
[b] Department of Physics, Sreegopal Banerjee College, Mogra, Hooghly 712148, India

ARTICLE INFO

Keywords:
Nanocomposite
Optical materials and properties
Absorption and emission spectra
Energy quenching
Stern-Volmer method
Förster's distance

ABSTRACT

This letter reports the paramount fluorescence resonance energy transfer mechanism for photo induced charge transfer from P3HT to solvothermally derived $CuInSe_2$. The HOMO (-4.85 eV) and LUMO (-3.38 eV) energy states of $CuInSe_2$ (electrical conductivity = 1.1x 10^{-7} Scm^{-1}) are determined from cyclic voltammetry and optical study. This HOMO-LUMO position agrees to select P3HT polymer as possible donor of excitons. Steady-state luminescence study of composite (P3HT:$CuInSe_2$) demonstrates possibility of successful charge transfer. Stern–Volmer analysis of absorption and emission spectroscopy ensures static energy quenching phenomena. The Förster distance (R_0) of critical energy transfer is estimated as 3.61 nm. The average distance between donor–acceptor (r_{avg} = 4.71 nm) is<8 nm and within the range $0.5R_0 < r < 1.5R_0$ (1.81 nm < r < 5.42 nm), which ensures energy transfer from P3HT to $CuInSe_2$.

1. Introduction

In recent past $CuInSe_2$ (CIS) composite and its application as electron acceptors in photovoltaics has become more popular because of its semiconductor nature with narrow band gap, non-toxicity, high reproducibility, tuneable optical energy gap, and good stability [1]. In order to attain higher performance of organic–inorganic solar cell, conjugated polymer like poly(3-hexylthiophene) (P3HT) is appreciated yet as electron donor. Extensive studied had been performed by several scientists and researchers on energy harvesting from the P3HT: $CuInSe_2$ composite based solar cells [2]. The understanding of underline physics of resonance energy transfer by quenching phenomena is an obvious commissioning task of charge transfer from donor to acceptor. However, the underline charge transport mechanism by fluorescence resonance energy transfer theory within this composite is not reported so far. Hence the field remain unexplored.

In this letter the solvothermally derived $CuInSe_2$ is composited with P3HT to study the state of quenching which is highly responsible for understanding the hopping of excitons from donor to acceptor [3]. Even though CIS's applications in Schottky diode has been reported earlier [4], perhaps this is the first approach to report the quenching phenomena and photo-induced charge transfer by utilizing FRET mechanism within the composite P3HT:$CuInSe_2$.

In this context, solvothermally derived CIS is characterized accordingly and the energy band positions are determined to find out the organic P3HT as appreciable donor with respect to CIS one. To get better insight the mechanism of energy quenching and the physics behind of hopping of excitons from donor to acceptor, the optical spectral (absorption and emission) analyses are performed pertinently. The analysis deserves a thorough inspection which is carried out by employing Stern-Volmer theory and Förster's equation for non-radiative energy transfer [5,6].

2. Materials & methods

Poly(3-hexylthiophene) (P3HT) purchased from Sigma-Aldrich. Flake like $CuInSe_2$ is derived by Solvothermal technique (reported elsewhere) [4].

FESEM and EDAX spectroscopy are performed with a FEI make Inspect F-50 scanning electron microscope equipped with energy-dispersive X-ray analysis system. Bruker D8 Advanced PXRD is used to record diffraction. The absorption spectra are obtained from Perkin Elmer Lambda 365 spectrophotometer. Fluorescence spectra are recorded via Perkin Elmer LS-45 fluorimeter. The electrical conductivity (σ) is

* Corresponding author.
E-mail address: alayek.physics@jadavpuruniversity.in (A. Layek).

https://doi.org/10.1016/j.matlet.2023.134066
Received 14 December 2022; Received in revised form 2 February 2023; Accepted 14 February 2023
Available online 16 February 2023

Materials Chemistry and Physics 301 (2023) 127542

Contents lists available at ScienceDirect

Materials Chemistry and Physics

journal homepage: www.elsevier.com/locate/matchemphys

Effect of size of CdO on bias dependent conduction and relaxation mechanism by means of impedance spectroscopy: Experimental and theoretical studies

Joydeep Datta [a,b,c,1], Animesh Biswas [a,d], Somobrata Acharya [b], Animesh Layek [a,1,*], Partha Pratim Ray [a,**]

[a] Department of Physics, Jadavpur University, Kolkata, 700032, India
[b] School of Applied & Interdisciplinary Sciences, Indian Association for the Cultivation of Science, Jadavpur, Kolkata, 700032, India
[c] Department of Physics, Techno India University, EM-4, Sector-V, Saltlake City, Kolkata, West Bengal, 700091, India
[d] Department of Physics, Sreegopal Banerjee College, Mogra, Hooghly, 712148, India

HIGHLIGHTS

- Hydrothermal Synthesis of CdO followed by different annealing temperature.
- Impedance spectroscopy analysis for the CdOs under different dc bias voltage.
- Study of relaxation and conduction mechanism of grain and grain Boundary.
- Study of electrical modulus and ac conductivity for conduction mechanism.
- The improvement in charge transportation for larger crystallite size.

GRAPHICAL ABSTRACT

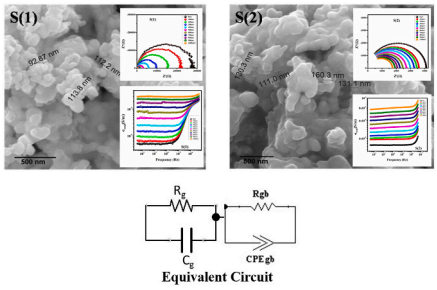

ARTICLE INFO

Keywords:
Nanostructured CdO
Impedance spectroscopy
Grain and grain boundary
Electrical modulus
AC conductivity

ABSTRACT

In this report, the morphological impact of hydrothermally derived CdO on charge conduction and relaxation is investigated by using bias-dependent impedance spectroscopy (IS). The work of art is the findings of the impact of grain and grain boundaries of CdO on the frequency-dependent electric conductivity and relaxation mechanism followed by the crystallite size. In this regard, two different crystallite size based CdOs are derived from hydrothermal route at different temperatures. Materials are characterized by XRD, FESEM, UV–vis absorption spectra. The dc conductivity is also evaluated by measuring current-voltage characteristics, and bias-dependent Impedance Spectroscopy at room temperature, which spectacles the CdO with larger crystallite size dominate the conduction mechanism.

* Corresponding author.
** Corresponding author.
E-mail addresses: alayek.physics@jadavpuruniversity.in, alayek.phys@gmail.com (A. Layek), parthapray@yahoo.com (P.P. Ray).
[1] These authors contributed equally.

https://doi.org/10.1016/j.matchemphys.2023.127542
Received 14 March 2022; Received in revised form 16 January 2023; Accepted 24 February 2023
Available online 10 March 2023

Chemical Physics 580 (2024) 112233

Contents lists available at ScienceDirect

Chemical Physics

journal homepage: www.elsevier.com/locate/chemphys

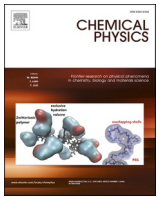

Performance of Schottky diode of structured FTO/TiO_2/Al employing hydrogen fluoride treated TiO_2: Qualitative and quantitative analysis

Ramjan Sk [a], Animesh Biswas [a,b], Animesh Layek [a,*], Partha Pratim Ray [a,*]

[a] Department of Physics, Jadavpur University, Kolkata 700 032, India
[b] Department of Physics, Sreegopal Banerjee College, Mogra, Hooghly 712148, India

ARTICLE INFO

Keywords:
HF treatment
TiO_2 nanoparticles
Schottky device
Mobility
Resistivity
Carrier concentration

ABSTRACT

Having ascertained the improvement of band gap and conductivity of the synthesized TiO_2 after HF treatment under consideration, it occurred to us that the materials may perform as the better Schottky barrier diode. To verify our presumption, we studied the I-V characteristic of the device fabricated in a sandwich configuration of FTO/sample/Al. The comparative studies show better potentiality of the material in subject to study the qualitative and quantitative measures of the Schottky devices. The work is concluded by examined the various characteristic parameters related with performance of device that is fabricated with HF treated and untreated TiO_2.

1. Introduction

In subject to high oxidation power, non-toxicity, long term stability and more over low synthesis cost, titanium dioxide (TiO_2) is a promising inorganic material. Though it is inefficient to harvest visible solar spectrum due to its larger band gap, but enormous effort had been given to make it applicable for photovoltaic devices by their entire work of pronounced scientists and researchers [1–6]. To improve the efficiency of absorption under visible light, numerous attempts have been made to modify the electronic structure of titanium dioxide by doping with various transition element (Zn, Ni, Co, Mn, Sn) [1–3] and group element (N, C, B, S, P) [4–6].

In recent years, much attention has been given in doping TiO_2 with halogen. Since Fluorine doping with TiO_2 improve the efficiency of stronger absorption in the UV–Vis region with decrease in band gap energy [7], it becomes a promising material in advance research of optoelectronics. Studies of F-doped TiO_2 reveals that F doping lowers the conduction band edge of TiO_2 [7,8].

Titanium oxide (TiO_2) nanoparticle has emerged as a superior material of interest for application of dye sensitized solar cell (DSSC)s, due to its wide band gap and *n*-type semiconducting property [9–12]. The performance of DSSC depends critically on the morphology, size, dimension and the doping concentration, which determines the electrical and thermal transport properties in addition to optical and mechanical properties [10]. To improve the energy conversion efficiency of DSSCs the understanding of the behavior of injected electron in TiO_2 is very much important. This is also depending on TiO_2 structure and its architectural development. Another important factor that can optimize the energy conversion efficiency of device is the thickness of TiO_2 film. To optimize the important factors, significant scientific and engineering effort has been examined and implemented [13]. To enhance the absorption ability, hence device performance, various TiO_2 nanocomposites with different architecture have been synthesized by adopting different synthesis techniques [14,15,16]. In order to investigate the effect of interfacial layers on electrical behavior an enormous effort have been given in study of TiO_2 based Schottky junction [17,18].

In this present study, to improve the absorption ability of TiO_2, Hydrogen fluoride (HF) treatment by a novel technique is performed on hydrothermally derived TiO_2 nanoparticle. It is noticed that the electrical conductivity of TiO_2 has been significantly improved. The optical band gap energy has also been reduced after HF treatment, that signifies high absorption coefficient, which would have a better impact on carrier transport followed by tunneling through Schottky barrier. This HF treated TiO_2 is applied in fabrication of metal–semiconductor junction based Schottky diode with aluminium (Al) as metal, having work function 4.1 eV. These synthesized and treated materials are characterized by powder X-ray diffraction, SEM, BET surface area measurement and UV–Vis absorption spectroscopy. The quality improvements as well as the performance of FTO/sample/Al based Schottky devices have been investigated through electrical characterization part followed by

* Corresponding authors.
E-mail addresses: alayek.physics@jadavpuruniversity.in (A. Layek), parthap.ray@jadavpuruniversity.in (P.P. Ray).

https://doi.org/10.1016/j.chemphys.2024.112233
Received 18 September 2023; Received in revised form 9 January 2024; Accepted 15 February 2024
Available online 21 February 2024

ACS APPLIED ENGINEERING MATERIALS

pubs.acs.org/acsaenm Article

Unveiling the Semiconducting Diode Property through Current Density−Voltage Features with Effective Interface Mobility and Conductivity of Nitroterephthalic Acid-Directed Supramolecular Co(II)/Cu(II) Metallogels

Indrajit Pal, Animesh Biswas, Santanu Majumdar, Gerald Lepcha, Baishakhi Pal, Partha Pratim Ray,* and Biswajit Dey*

Cite This: *ACS Appl. Eng. Mater.* 2023, 1, 3005−3015 Read Online

ACCESS | Metrics & More | Article Recommendations | Supporting Information

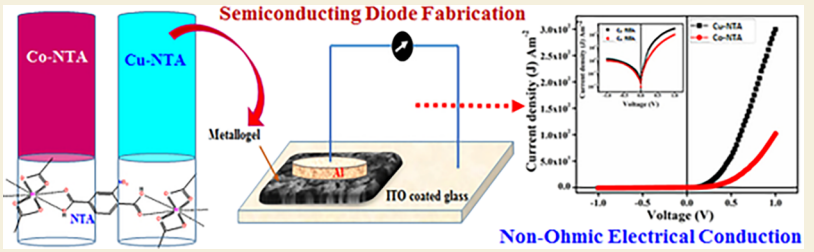

ABSTRACT: Nitroterephthalic acid (NTA)-based supramolecular Co(II)/Cu(II) metallogels were precisely achieved. NTA as the low molecular weight gelator is stoichiometrically combined with respective metal salts to construct Co-NTA and Cu-NTA metallogels in *N*,*N*′-dimethylformamide (DMF) medium. The mechanoelastic properties of both metallogels have been meticulously established through the assessment of rheological parameters. The microstructural arrangements within the xerogel samples are intricately elucidated through field emission electron scanning microscopy (FESEM), and this depicts distinct interconnected stacked-like morphological configurations within the supramolecular metallogels. Verification of persisting elements contributing to the metallogel formation is achieved through comprehensive EDX elemental analyses. FTIR spectroscopic analyses dictate the signature of noncovalent interactions for offering an individual stable metallogel network. The possible major repeating unit within the metallogel network is ascertained with the utmost precision through exhaustive ESI mass spectral analyses. The semiconducting behavior of the fabricated metallogels has also been executed. Remarkably, these metallogels exhibit nonlinear *J*−*V* characteristics, accompanied by rectification ratios of 102.82 (Co-NTA) and 211.52 (Cu-NTA), underscoring exceptional charge transport attributes for both metallogels. Notably, insights into the Schottky diode parameters of both metallogels and Cu-NTA material display enhanced effective interface mobility, conductivity, and transit time, collectively implying an improved conduction mechanism.

KEYWORDS: *Co(II) and Cu(II)-metallogel, FESEM, rheology, Schottky diode device, space-charge limited conduction (SCLC), non-Ohmic*

1. INTRODUCTION

Beyond the world of covalent interactions, noncovalent facets have been manifested through the domain of supramolecules.[1] In supramolecular chemistry, multitudes of versatile noncovalent interactions (electrostatic interactions, hydrogen bonding, hydrophobic interactions, van der Waals interaction, metal ion coordination modes, etc.) participate in building synthetic chemical architectures from a discrete number of molecules.[1] This rapidly growing branch of chemistry has witnessed a tremendous surge in contemporary technological advances and related works during the past decade.[2] The marvelous attributes and adaptability of supramolecular systems permit their incorporation in endless fields of research across all branches of science and technology.[2] In terms of the progress of supramolecular research, gel earns a key focus.[3] The current decade is overwhelmed by the use of huge research works, which are being materialized by the molecular self-assembling process of gel science and technology through the use of LMWGs (compounds having molecular mass less than 3000) in the gelation process for their numerous

Received: August 18, 2023
Revised: October 5, 2023
Accepted: October 13, 2023
Published: October 26, 2023

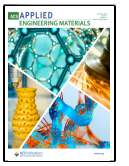

https://doi.org/10.1021/acsaenm.3c00481
ACS Appl. Eng. Mater. 2023, 1, 3005−3015

CrystEngComm

ROYAL SOCIETY OF CHEMISTRY

PAPER

View Article Online
View Journal | View Issue

Cite this: *CrystEngComm*, 2023, **25**, 1006

An insight into the non-covalent interactions in the solid state structures of dinuclear cobalt(II) complexes with N,O-donor ligands: application of the complexes in the fabrication of Schottky devices†

Rabi Sankar Sarkar, [a] Animesh Biswas, [bc] Partha Pratim Ray, *[c] Rosa M. Gomila, [d] Michael G. B. Drew, [e] Snehasis Banerjee, [f] Antonio Frontera *[d] and Shouvik Chattopadhyay *[a]

Received 16th September 2022,
Accepted 19th December 2022

DOI: 10.1039/d2ce01282k

rsc.li/crystengcomm

Two new dinuclear cobalt(II) complexes, $[(H_2O)Co^{II}L^1(\mu\text{-}O_2CR^1)Co^{II}(NCS)]$ (**1**) and $[(DMSO)Co^{II}L^2(\mu\text{-}O_2CR^2)Co^{II}(NCS)]$ (**2**) (H_2L^1 = (2,2-dimethyl-1,3-propanediyl)bis(iminomethylene)bis(6-methoxyphenol), H_2L^2 = (2,2-dimethyl-1,3-propanediyl)bis(iminomethylene)bis(6-ethoxyphenol), R^1CO_2H = 3-methyl-4-nitrobenzoic acid, and R^2CO_2H = 4-methyl-3-nitrobenzoic acid), were synthesized using multidentate N, O-donor ligands with two pockets. Each complex was characterized using single crystal X-ray diffraction and spectral analysis. The noncovalent interactions were analyzed using density functional theory (DFT) calculations. In addition, the optical properties of the complexes were studied with a focus on the band gaps. Both complexes were utilized for the fabrication of semiconducting Schottky devices.

Introduction

The 1 : 2 condensation of various diamines and salicylaldehyde produces H_2salen-type (sal = salicylaldehyde and en = 1,2-diaminoethane) Schiff bases, the di-negative anionic forms of which have been widely used by synthetic inorganic chemists as tetradentate N_2O_2-donor chelating ligands for the synthesis of mono-, di- and poly-nuclear complexes of several transition and non-transition metals.[1–10] It is also a very common strategy of synthetic inorganic chemists to exploit the interesting bridging ability of the phenoxo oxygen atoms of the mononuclear complexes of transition metals with salen ligands for the synthesis of hetero-nuclear complexes, where the mononuclear metal–salen moieties can be used as metallo-ligands.[11–15] Another common way to develop di- and poly-nuclear complexes with salen-type ligands is to use 3-alkoxysalicylaldehyde (instead of salicylaldehyde), so that compartmental $N_2O_2O_2'$-donor Schiff bases, which may accommodate smaller metal ions in their inner N_2O_2 cavity and the relatively large cations in their outer O_4 cores, can be produced.[16–20] The salen-type Schiff bases can easily be reduced with a mild reducing agent to form the corresponding reduced Schiff base ligands, which are essentially secondary diamines and may be more beneficial due to their greater flexibility and stability over a wider range of solvents as well as in oxidizing and reducing conditions.[21–25]

The unusual physical properties of several di- and poly-nuclear complexes with salen-type Schiff base ligands and their reduced analogues and their ability to mimic the biological functions of different metalloproteins have attracted the interest of coordination chemists to synthesize, characterize and explore new complexes in salen and reduced salen families.[26–29] Additionally, multi-metallic complexes containing paramagnetic metal centers are important for their interesting magnetic properties and applications as magnetic materials.[30–34] Another leading area of modern research is the study of the opto-electronic properties of these complexes. The production and transportation of charge

[a] *Department of Chemistry, Inorganic Section, Jadavpur University, Kolkata 700032, India. E-mail: shouvik.chem@gmail.com*
[b] *Department of Physics, Sreegopal Banerjee College, Hooghly 712148, West Bengal, India*
[c] *Department of Physics, Jadavpur University, Kolkata 700032, India. E-mail: partha@phys.jdvu.ac.in, parthapray@yahoo.com; Fax: +91 3324138917*
[d] *Department of Chemistry, Universitat de les Illes Balears, Crta de Valldemossa km 7.5, 07122 Palma de Mallorca, Spain. E-mail: toni.frontera@uib.es*
[e] *School of Chemistry, The University of Reading, P.O. Box 224, Whiteknights, Reading RG6 6AD, UK*
[f] *Department of Higher Education, (University Branch) Government of West Bengal, Bikash Bhavan, Salt Lake, Kolkata-91, India*

† Electronic supplementary information (ESI) available: Hirshfeld surface analysis, Tables S1–S6; figures S1–S6; CCDC 2104932 and 2204058 for complexes **1** and **2** respectively. For ESI and crystallographic data in CIF or other electronic format see DOI: **https://doi.org/10.1039/d2ce01282k**

J Mater Sci: Mater Electron (2023) 34:1574

Exploring reduced graphene oxide-zinc telluride nanocomposites for enhanced charge transfer in optoelectronic devices: a study of the metal–semiconductor interfaces via equivalent circuit model

Dhananjoy Das[1], Mainak Das[1], Animesh Biswas[1,2], Puspendu Sahu[1], and Partha Pratim Ray[1,*]

[1] *Department of Physics, Jadavpur University, Kolkata 700032, India*
[2] *Department of Physics, Sreegopal Banerjee College, Mogra, Hoogly 712148, India*

Received: 29 June 2023
Accepted: 10 July 2023
Published online: 24 July 2023

ABSTRACT

This study presents the synthesis of zinc telluride (ZnTe) nanoflakes and their composite with reduced graphene oxide (RGO-ZnTe) through a simple hydrothermal reaction. The crystal structure of the synthesized materials was characterized using X-ray Diffraction techniques. Subsequently, the Metal-Semiconductor (MS) based Schottky devices were fabricated by depositing the ZnTe and RGO-ZnTe thin films and Aluminium electrodes via vacuum coating methods. The surface morphology and topography of the deposited films were investigated using field emission scanning electron microscopy (FESEM) and atomic force microscopy (AFM) techniques, respectively, to study the formation of MS junctions. The interfacial properties of the MS junctions in the Al/ZnTe/ITO and Al/RGO-ZnTe/ITO configurations were analyzed using ac impedance spectroscopy over a frequency range of 50 Hz–10 MHz. Thereafter, the bias-dependent impedance spectrometry was also conducted within a voltage range of ± 0.6 V to establish the equivalent circuits for the fabricated MS junction Schottky diodes (SDs). The diode parameters, including on/off ratio, ideality factor, barrier height and series resistance were determined by measuring the current–voltage (*I*–*V*) characteristics of the fabricated SDs. Further, the charge transport parameters, such as dc conductivity and photosensitivity, were also estimated. The findings indicate that the Schottky devices based on the RGO-ZnTe composites exhibit enhanced device performance compared to those based on pristine ZnTe, attributed to the synergistic effects between the RGO sheets and ZnTe nanoflakes.

Address correspondence to E-mail: parthapray@yahoo.com

https://doi.org/10.1007/s10854-023-10978-7

Elucidation of Inhomogeneous Heterojunction Performance of Al/Cu_5FeS_4 Schottky Diode With a Gaussian Distribution of Barrier Heights

Sayantan Sil, Rajkumar Jana, Animesh Biswas, Dhananjoy Das, Arka Dey, Joydeep Datta, Dirtha Sanyal, and Partha Pratim Ray

***Abstract*— Here, we analyze inhomogeneities in the barrier height (BH) of Al/Cu_5FeS_4 Schottky device from the electrical (*I–V*) measurements with a temperature range between 303 and 408 K. The temperature-dependent performance of our fabricated device is analyzed by using the thermionic emission (TE) theory. Some important diode parameters like BH (Φ_{bo}), ideality factor (η), and series resistance (R_S) are evaluated from the forward current–voltage characteristic curves. The calculated η and R_S of the Schottky barrier diode (SBD) decrease, whereas the Φ_{bo} of the device increases with the increase in temperature. The value of Richardson constant (A^*) for our material is obtained as 1.94×10^{-4} A cm^{-2} K^{-2} in the temperature range 303–408 K, which is found as much lesser than the theoretical value of 29.90 A cm^{-2} K^{-2}. The discrepancy of A^* from the theoretical value has been well explained by TE theory with the assumption of Gaussian distribution (GD) of BHs due to the existence of BH inhomogeneities at metal semiconductor (MS) junction. The obtained values of the mean BH $\overline{\Phi_{bo}}$ and the standard deviation σ_s are 1.026 eV and 173 mV in the corresponding temperature range. The mean BH (1.199 eV) and Richardson constant (29.73 Acm^{-2}K^{-2}) are determined from the modified Richardson plot depending on the inhomogeneity of BHs. Apparent BH consists of mean BH ($\overline{\Phi_{bo}}$) and standard deviation (σ_s). The σ_s contributes significantly to the modification of Richardson constant and mean BH. The calculated value of the modified Richardson constant is in close agreement with the theoretical value. From *C–V* measurements built-in voltage and effective BH of this structure were calculated as a function of frequency.**

***Index Terms*— Al/Cu_5FeS_4 Schottky diode, barrier inhomogeneities, Gaussian distribution (GD), *I–V* characteristics, Richardson constant.**

I. Introduction

THE ternary chalcogenide materials have enjoyed much attention and plenty of prospects in the field of material science due to its promising physical properties [1], [2]. Bornite (Cu_5FeS_4) is a common and widespread copper sulfide mineral that has been well known for many years due to its fascinating electrical and magnetic properties [3], [4]. The current conduction mechanism of Schottky barrier diodes (SBDs) is dependent on various parameters, such as the device temperature, process of surface preparation, inhomogeneities of barrier height (BH) at metal semiconductor (MS) interface, the series resistance of the device, and applied bias voltage [5], [6]. Many researchers have paid their attention to study the current transport properties through the SBD at room temperature, but the information about the conduction process or the nature of barrier formation at the MS interface could not be described with room temperature *I–V* analysis [7], [8]. Therefore, it is crucial to study the temperature-dependent analysis of SBDs, which allows us to realize the different views of conduction mechanisms and barrier formation at MS interface [9], [10]. In this article, the forward bias *I–V* measurements have been carried out in the temperature range 303–408 K on Al/Cu_5FeS_4 SBDs. On the other hand, to the best of our knowledge, the temperature-dependent analysis of Al/Cu_5FeS_4 SBD has not yet been reported. The unusual behavior of the temperature dependence SBD parameters, such as BH, ideality factor, Richardson's constant, and series resistance, is evaluated on the assumption of a Gaussian distribution (GD) of BHs.

II. Experimental Section

A. Materials and Synthesis

All the analytical reagent (AR) grade reagents are purchased from Sigma–Aldrich. All reagents are used as it is procured. Cu_5FeS_4 (Bornite) is prepared by the hydrothermal synthesis technique. The synthesis procedure is reported in the previous work [2].

Manuscript received January 12, 2020; accepted March 23, 2020. Date of publication April 10, 2020; date of current version April 22, 2020. The work of Partha Pratim Ray was supported by the Science and Engineering Research Board-Department of Science and Technology (SERB-DST), Government of India under Grant EMR/2016/005387. The review of this article was arranged by Editor J. Mateos. *(Corresponding author: Partha Pratim Ray.)*

Sayantan Sil, Rajkumar Jana, Dhananjoy Das, Joydeep Datta, and Partha Pratim Ray are with the Department of Physics, Jadavpur University, Kolkata 700032, India (e-mail: partha@phys.jdvu.ac.in).

Animesh Biswas is with the Department of Physics, Jadavpur University, Kolkata 700032, India, and also with the Department of Physics, Sreegopal Banerjee College, Hooghly 712148, India.

Arka Dey is with the Department of Condensed Matter Physics and Material Sciences, S. N. Bose National Center for Basic Sciences, Kolkata 700106, India.

Dirtha Sanyal is with the Variable Energy Cyclotron Center, Kolkata 700064, India, and also with the Training School Complex, Homi Bhaba National Institute, Mumbai 400094, India (e-mail: dirtha@vecc.gov.in).

Color versions of one or more of the figures in this article are available online at http://ieeexplore.ieee.org.

Digital Object Identifier 10.1109/TED.2020.2983489

J Mater Sci: Mater Electron **(2024) 35:1143**

Investigation of charge transfer in optoelectronic devices: a study of carbon nanotube-copper sulfide nanocomposites using equivalent circuit models for metal–semiconductor interfaces

Mainak Das[1], Dhananjoy Das[1], Supravat Ghosh[1], Ramjan Sk[1], Animesh Biswas[1,2], and Partha Pratim Ray[1,*]

[1] *Department of Physics, Jadavpur University, Kolkata 700032, India*
[2] *Department of Physics, Sreegopal Banerjee College, Mogra, Hooghly 712148, India*

Received: 4 April 2024
Accepted: 1 June 2024
Published online: 14 June 2024

ABSTRACT

This study outlines the synthesis of copper sulfide (CuS) nanoparticles and their composites with carbon nanotubes (T-CuS) via a solvothermal reaction. X-ray diffraction techniques were employed to characterize the crystal structure of the synthesized materials. Thin films of both CuS and T-CuS were deposited using vacuum coating techniques to construct Schottky devices. Atomic force microscopy (AFM) and field emission scanning electron microscopy (FESEM) were utilized to examine the topography and surface morphology of the deposited films, enabling analysis of metal–semiconductor (MS) junction formation. The interfacial characteristics of MS junctions in Al/CuS and T-CuS/ITO designs were investigated using AC impedance spectroscopy (IS) over a frequency range of 40 Hz to 10 MHz. Bias-dependent impedance spectroscopy within a ± 1.0 V range was conducted to determine the equivalent circuit for the MS junction Schottky diodes (SDs). Parameters such as on/off ratio, series resistance, ideality factor, and barrier height of the fabricated diodes were derived from current–voltage (*I*–*V*) characteristics. Additionally, characteristics related to charge transport, including photosensitivity and conductivity, were calculated. The results indicate an enhanced performance of carbon nanotube-based Schottky devices, likely attributed to the strong interaction and synergy between CNTs and CuS nanoparticles.

1 Introduction

In recent years, the usage of compound semiconductors in electronic and optoelectronic devices has witnessed a notable increase, primarily propelled by the growing demand for solar energy solutions [1]. Copper metal chalcogenide semiconductors, exemplified by copper oxide (CuO), copper selenide (CuSe), and copper telluride (CuTe), have garnered attention owing to their favorable attributes, encompassing low environmental

Address correspondence to E-mail: parthapray@yahoo.com

https://doi.org/10.1007/s10854-024-12876-y

Materials Research Express

PAPER

Exploration of temperature dependent dielectric relaxation and correlated barrier hopping (CBH) conduction mechanism of hydrothermally synthesized CuO nanoflakes

RECEIVED
10 June 2019

REVISED
23 August 2019

ACCEPTED FOR PUBLICATION
5 September 2019

PUBLISHED
18 September 2019

Rajkumar Jana[1], **Joydeep Datta**[1], **Sayantan Sil**[1], **Arka Dey**[1], **Baishakhi Pal**[1], **Animesh Biswas**[1,2] and **Partha Pratim Ray**[1]

[1] Department of Physics, Jadavpur University, Kolkata–700 032, India
[2] Sreegopal Banerjee College, Bagati, Mogra, Hooghly 712148, India

E-mail: partha@phys.jdvu.ac.in

Keywords: non-Debye type relaxation, hopping mechanism, ac and dc activation energy, time temperature superposition

Supplementary material for this article is available online

Abstract

In this study, we have reported the temperature-dependent relaxation and hopping conduction mechanism of the hydrothermally synthesized nanoflake like cupric oxide (CuO) by employing complex impedance spectroscopy technique. The non-Debye type relaxation mechanism has been explored from the impedance and modulus formalism. Frequency dependent ac conductivity analysis suggests that the material follows correlated barrier hopping (CBH) model and also satisfies the Jonscher's universal power law at various temperatures. Moreover, the density of localized states of the synthesized material near Fermi level was estimated at different frequency. We have also elucidated the activation energy, the hopping distance and the maximum barrier height of the materials. It has been observed that the scaling behavior of the conductivity isotherms can be explained by the time temperature superposition (TTS) principle. Two important parameters of the synthesized sample such as the number density of the charge carrier and the charge carrier mobility are also calculated. This study has tried to enlighten the behaviour of relaxation and conduction mechanism of CuO nanoflake at various temperatures and explained it from the theoretical point of view.

1. Introduction

Among the various transition metal oxides, cupric oxide (CuO) has attracted considerable attention because of its environment-friendly nature, easy and low cost processability of the compound in its pure form. It is a very promising semiconducting type material having many unique features [1, 2] and potential application possibilities in the various fields such as field effect transistors [3], gas sensors [4] catalysis [5], biosensors [6] and dye-sensitized solar cell [7] and so on. Additionally, in recent times, CuO shows promise in the field of microelectronics due to its giant dielectric behavior [8]. It is already well established that the particle size-shape and the dielectric constant of CuO strongly dependent on the synthesis procedure and conditions [9]. Therefore, the investigations of the structural and optical properties of CuO nanostructures have drawn considerable attention to the researchers. The dielectric measurements of the semiconducting material can enlighten the underlying relaxation mechanism of charge carriers. Exploration of the electrical properties is necessary to predict the dynamical behaviour of the charge carriers present in the material. The measurements of ac conductivity have been widely used to get a true picture about the conduction process in the material. The complex impedance spectroscopy (CIS) technique is an exceptional and informative characterization tool to study the contributions of grains, grain boundaries, the contact effects and the impurities inside the sample [10, 11]. In particular, there are very few works reported on the temperature dependent relaxation and conduction mechanism dominated by the carrier hopping in CuO nanoflake (NF). To understand the hopping mechanism, various theoretical models, such as quantum mechanical tunneling (QMT) [12], non overlapping

Journal of Materials Science: Materials in Electronics (2018) 29:5014–5024
https://doi.org/10.1007/s10854-017-8463-4

Bias dependent conduction and relaxation mechanism study of Cu_5FeS_4 film and its significance in signal transport network

Sayantan Sil[1] · Joydeep Datta[1] · Mrinmay Das[1] · Rajkumar Jana[1] · Soumi Halder[1] · Animesh Biswas[2] · Dirtha Sanyal[3,4] · Partha Pratim Ray[1]

Received: 27 October 2017 / Accepted: 19 December 2017 / Published online: 28 December 2017

Abstract
Here we have reported the electric and dielectric properties of a Bornite (Cu_5FeS_4) film using non-destructive complex impedance spectroscopy (CIS) in the frequency range 40 Hz–20 MHz and bias voltage range 0–0.8 V. A typical hydrothermal reaction was carried out to obtain the Cu_5FeS_4 material. Thereafter, we fabricated the film of the synthesized material and analysed its various properties as a function of frequency and dc bias voltages. The CIS analysis at room temperature (303 K) for different forward dc bias voltages shows that the bulk resistance plays a predominant role in conduction mechanism. The complex impedance (Nyquist) plots are well modelled with grain and grain boundary resistance by introducing proper ac equivalent circuit. The impedance loss spectra showed that the relaxation peak shifts towards the higher frequency with increasing bias voltages, which implies the possibility of a charge hopping between the localized charge states. Furthermore, we find that dielectric constant (ε'), dielectric loss (ε''), electrical modulus (M^*) and ac/dc conductivity of the Cu_5FeS_4 film are strongly frequency dependent. The values of ε' and ε'' decreases whereas ac conductivity increases with increasing frequency. High frequency and low frequency dielectric constant of the material are found to be 3.48 and in the order of 10^4 respectively. Electrical modulus study is introduced for better explanation of conductivity relaxation phenomenon. Finally, we investigated the variation of ac/dc conductivity with forward dc bias voltages. This confirmed the presence of a hopping mechanism for electrical transport in our system, which can be best explained on the basis of jump relaxation model. Overall, this extensive study based on complex impedance spectroscopy demonstrates the dielectric relaxation behaviour of Cu_5FeS_4 film and also shed light on hopping induced conduction mechanism.

1 Introduction

Recently, metal chalcogenide semiconductor nanoparticles are being intensively studied in solar energy conversion devices because of their great light absorbing capacity [1], high conversion efficiency and low toxicity [2]. Metal sulphides exhibit a fascinating diversity in structural chemistry as well as in electrical, magnetic and other physical properties [3–6]. In the ternary system Cu–Fe–S, Chalcopyrite ($CuFeS_2$) and Bornite (Cu_5FeS_4) is important for their applications in the arena of materials science due to the presence of major copper minerals [7]. A large variety of experiments in this sulphide mineral have been done in the presence of bacteria and as electrodes in electrochemical cells [8–10]. Many researchers have explained the magnetic behaviour of Bornite, vacancy clustering, super paramagnetic relaxation [11, 12], thermo electric properties [13] and also provided the information about valence state of copper (Cu) and iron (Fe^{2+}, Fe^{3+}) [14, 15]. Bornite (Cu_5FeS_4) has three polymorph phases referred to as high cubic phase, intermediate cubic phase and low orthorhombic phase [16]. Crystal structures of Bornite (Cu_5FeS_4) are based on a cubic closest packed array of sulphur (S) atom (antifluorite-type cell) with space group Fm3m [13] and metal atoms (Cu and Fe) are randomly

✉ Dirtha Sanyal
dirtha@vecc.gov.in

✉ Partha Pratim Ray
partha@phys.jdvu.ac.in

[1] Department of Physics, Jadavpur University, Kolkata 700032, India

[2] Sreegopal Banerjee College, Bagati, Mogra, Hooghly 712148, India

[3] Variable Energy Cyclotron Centre, 1/AF, Bidhannagar, Kolkata 700064, India

[4] Homi Bhabha National Institute, Training School Complex, Anushakti Nagar, Mumbai 400094, India

Materials Research Bulletin 118 (2019) 110507

Contents lists available at ScienceDirect

Materials Research Bulletin

journal homepage: www.elsevier.com/locate/matresbu

Effect of graphene on improved photosensitivity of MoS_2-graphene composite based Schottky diode

Soumi Halder[a], Baishakhi Pal[a], Arka Dey[a,b], Sayantan Sil[a], Pubali Das[a], Animesh Biswas[a,c], Partha Pratim Ray[a,*]

[a] Department of Physics, Jadavpur University, Kolkata, 700 032, India
[b] Department of Condensed Matter Physics and Material Sciences, S. N. Bose National Centre for Basic Sciences, Block JD, Sec. III, Salt Lake, Kolkata, 700106, India
[c] Sreegopal Banerjee College, Bagati, Mogra, Hooghly, 712148, India

ARTICLE INFO

Keywords:
Schottky barrier diode
MoS_2
Current density-voltage
Photosensitivity
Charge transport phenomena

ABSTRACT

In this work, MoS_2 and MoS_2-Graphene (MGC) composite have been synthesized by hydrothermal process followed by their structural, optical and electrical characterization. The current density-voltage measurements have been performed at room temperature by fabricating Al/MoS_2 and/or MGC/ITO configured sandwich structured metal-semiconductor (MS) thin film Schottky devices. Under light and dark conditions, various parameters of our synthesized material based devices like rectification ratio, series resistance, barrier height, etc. have been measured and compared between the two. All the measured electrical properties show improvement for the composite based diodes, noteworthy the photosensitivity which has been increased by almost 33 times, signifying its potential application in photosensitive devices.

1. Introduction

In the last few years two dimensional (2D) atomic crystal like Graphene, black phosphorus, MoS_2 have attracted great attention of the researchers for their unique physical and chemical properties like great mechanical flexibility, high thermal stability and a very good range of electrical conductivity [1–3].Graphene has a potential for the use in a wide range of applications like Li-ion batteries, supercapacitors, fuel cells, photovoltaic and others [4]due to its properties like large surface area [5], excellent electrical conductivity and high mechanical strength [6]. Also, a wide range of applications of transition-metal dichalcogenide material in areas like photosensing devices, solid lubricant, electrochemical devices, and capacitors are already in progress [7]. Molybdenum Disulphide (MoS_2) has a two-layered sandwiched structure of the Mo layer between two S layer held together by weak Vander Walls interaction [8,9]. However, in order to enhance the electrical conductivity of $MoS_2$and to overcome various other deficiencies, there has been a recent focus on the synthesis of MoS_2 Graphene composites (MGC) to make use of the potentiality of Graphene as a highly conducting material. In the context of the metal-semiconductor junction, there has been a widespread application of bulk MoS_2 or Graphene in Schottky device. However, the implementation of semiconducting MGC in Schottky Barrier Diode (SBD) and its effects on electrical parameters should be studied in detail.

In this work, pure MoS_2 and MGC have been synthesized by using hydrothermal process and the structural, optical and electrical characterization has been done. Using MoS_2 and MGC as the basic structure, the detailed analysis of the fabricated SBDs has been done. The measured electrical conductivity, photosensitivity, and rectification ratio of MGC based devices show large improvement compared to devices made with pure MoS_2 or Graphene as semiconducting material. The calculated Schottky Diode parameters like barrier height, ideality factor, diffusion coefficient and diffusion length for MGC based devices also show better performance.

2. Experimental Section

2.1. Synthesis of MoS_2

The MoS_2nanocomposite has been synthesized by the hydrothermal method as per the procedure mentioned elsewhere [10]. In short, 2.19 g of $Na_2MoO_4.2H_2O$ and 2.07 g of H_2NCSNH_2have been added in 70 mL of deionized water with vigorous stirring for about 10 min. After adjusting the pH value to less than 1 with12 M HCl, the mixture has been transferred into a 100 mL Teflon lined stainless steel autoclave and heated at 200 °C for 24 h.

* Corresponding author.
E-mail address: partha@phys.jdvu.ac.in (P.P. Ray).

https://doi.org/10.1016/j.materresbull.2019.110507
Received 9 December 2018; Received in revised form 29 May 2019; Accepted 29 May 2019
Available online 30 May 2019

Available online at www.sciencedirect.com

ScienceDirect

Materials Today: Proceedings 11 (2019) 776–781

materialstoday: PROCEEDINGS

www.materialstoday.com/proceedings

2nd International Conference on Emerging Materials: Characterization and Application (EMCA-2017)

Enhanced charge transport properties of rGO-TiO_2 based Schottky diode by tuning graphene content

Mrinmay Das,[a] Joydeep Datta, [a] Animesh Biswas,[b] Soumi Halder, [a] and Partha Pratim Ray [a] *,

[a] *Department of Physics, Jadavpur University, Kolkata – 700 032, India,*
[b] *Department of Physics, Sreegopal Banerjee College, Mogra, Hooghly-712148, India*

Abstract

Here we report the fabrication of Al/rGO-TiO_2 Schottky barrier diodes (SBD) and the effect of graphene content on charge transport properties. The SBDs showed better performance after graphene incorporation and the best result was obtained for 5% rGO. We employed space charge limited current (SCLC) theory to estimate the carrier mobility, carrier concentration and diffusion length. For 5% rGO, we achieved a carrier mobility of 0.065 $cm^2V^{-1}s^{-1}$, which is almost a 15 fold increase on pure TiO_2 and the diffusion length improved by 35%. The study demonstrates improved charge transport by tuning rGO content, which can be beneficial for device applications.

Selection and peer-review under responsibility of Conference Committee of the 2nd International Conference on Emerging Materials: Characterization and Application (EMCA-2017).

Keywords: Metal-semiconductor junction, Schottky barrier diode, rGO-TiO_2, Charge transport

1. Introduction

Formation of Schottky barrier diode (SBD) at a metal-semiconductor (MS) junction and the charge transport analysis has attracted much interest recently.[1] SBDs are a key part in modern electronics due to their usability in power and frequency control circuits.[2] The performance and reliability of a SBD is closely related to many factors

* Corresponding author. Tel.: +91-9475237259
E-mail address: partha@phys.jdvu.ac.in

Selection and peer-review under responsibility of Conference Committee of the 2nd International Conference on Emerging Materials: Characterization and Application (EMCA 2017).

TWO DAYS SEMINAR

on

Twists and Turns in Physics Research : Special Emphasis on Condensed Matter and Biophysics (TTPR-2017)

Organised by

Department of Physics, Jadavpur University, Kolkata

Supported by UGC-DSA-I Programme

CERTIFICATE OF PARTICIPATION

This is to certify that Mr./Mrs/Dr./Prof. Animesh Biswas

has participated/presented (oral/poster) a paper entitled .....

..... *In the two days seminar on "Twists and Turns in Physics Research: Special Emphasis on Condensed Matter and Biophysics (TTPR-2017)" on 21-22 February, 2017 held at Department of Physics, Jadavpur University, Kolkata – 700032.*

Conveners

Dr. Dipankar Mandal
Dr. Subrata Sarkar
Dr. Sk Saiyad Ali
Dr. Saikat Kr. Seth

Prof. Argha Deb
Head, Department of Physics
Jadavpur University

Fourth International Symposium on Semiconductor Materials and Devices
ISSMD 4
8th-10th March, 2017

CERTIFICATE OF PARTICIPATION

This is to certify that *Mr. Animesh Biswas*

from *Jadavpur University*

has presented a paper / participated in the International Symposium on Semiconductor Materials and Devices (ISSMD 2017), organized at the School of Materials Science and Nanotechnology, Jadavpur University, Kolkata, West Bengal, INDIA during March 8-10, 2017.

Prof. K. K. Chattopadhyay
Convener, ISSMD 2017

Two-day Workshop on Material Characterization Techniques

Certificate of Participation

This is to certify that ....ANIMESH BISWAS..... of .SREEGOPAL BANERJEE COLLEGE.....

has participated in the

"Two-day Workshop on Material Characterization Techniques"

Sponsored by

Science and Engineering Research Board (SERB)

February 02-03, 2023

at CSIR-Central Glass and Ceramic Research Institute, Kolkata
196, Raja S C Mullick Road, Kolkata 700032, India

.....

Co-ordinator
Dr. Swastik Mondal

Indian Workshop and Symposium on
Modelling, Experimentation and Simulation on Complex Systems

MESCoS 2015

August 05 – 07, 2015

IndianOil

HALDIA INSTITUTE OF TECHNOLOGY, HALDIA, WEST BENGAL

Financially supported by **SERB-DST, GoI & IOCL**

CERTIFICATE

This is to certify that Prof. /Dr. /Mr. /Ms. Animesh Biswas of Sreegopal Banerjee College participated/delivered an invited talk/chaired a session/presented a paper/presented a poster in a technical session of MESCoS 2015. Title of talk/paper: Surfactant Guided Synthesis of Titanium Dioxide : Morphological Impact on Optoelectronic Switching Device

Prof. P. P. Das
Secretary, MESCoS2015

Dr. S. Agarwal
Secretary, MESCoS2015

Dr. R. Chatterjee
Convenor, MESCoS2015